

---

# Test Results at Transonic Speeds on a Contoured Over-the-Wing Propfan Model

---

Alan D. Levin, Donald B. Smeltzer and Ronald C. Smith

---

LIBRARY COPY FOR REFERENCE

LANG: L  
ENTER: SA  
PRINIA

NOT TO BE TAKEN FROM THIS ROOM

July 1986



NF01666

**NOTICE**

**FOR EARLY-DOMESTIC-DISSEMINATION**

Because of its significant early commercial potential, this information, which has been developed under a U S Government program, is being disseminated within the United States in advance of general publication. This information may be duplicated and used by the recipient with the express limitation that it not be published. Release of this information to other domestic parties by the recipient shall be made subject to these limitations. Foreign release may be made only with prior NASA approval and appropriate export licenses. This legend shall be marked on any reproduction of this information in whole or in part.

Date for general release July 1988



National Aeronautics and  
Space Administration

---

# **Test Results at Transonic Speeds on a Contoured Over-the-Wing Propfan Model**

---

Alan D. Levin,  
Donald B. Smeltzer,  
Ronald C. Smith, Ames Research Center, Moffett Field, California

July 1986



*N88-28918 #*

## NOMENCLATURE

$c_D$	drag coefficient, drag/qS
$c_L$	lift coefficient, lift/qS
$c_M$	pitching moment coefficient, pitching-moment/qS $\bar{c}$
$c_p$	pressure coefficient, $(p - p_\infty)/q$
$c_{P_{\text{prop}}}$	propeller power coefficient, power/ $\rho_\infty N^3 D^5$
$c_{T_{\text{NET}}}$	propeller net thrust coefficient, net-thrust/qS
$c_{T_{\text{prop}}}$	propeller thrust coefficient, thrust/ $\rho_\infty N^2 D^4$
$\bar{c}$	mean aerodynamic chord, 0.702 m
D	propeller diameter, 0.622 m
EPR	exhaust pressure ratio, $p_{t_e}/p_{s_e}$
J	advance ratio, $60V/ND$
M	Mach number
N	propeller rotational speed, rpm
p	local static pressure, kPa
$p_{s_e}$	average nozzle exit static pressure, kPa
$p_{t_e}$	average nozzle exit total pressure, kPa
$p_\infty$	free-stream static pressure, kPa
q	free-stream dynamic pressure, kPa
S	reference area, $1.434 \text{ m}^2$
V	free-stream velocity, m/s
x/c	local chord station, fraction of chord measured from the baseline wing leading-edge
$\alpha$	angle of attack, deg

$\beta_p$	propeller blade pitch angle, deg
$\eta$	span station, fraction of semispan
$\rho_\infty$	free-stream density, kg/m <sup>3</sup>
$\Delta Y, \Delta Z$	horizontal and vertical displacement of contoured nacelle propeller axis, respectively, from the UTW nacelle geometry, cm

#### Subscripts

INS	installed
NAC	nacelle
SS	slipstream
TR	thrust removed

#### Configuration codes

B	body
E	extended duct
H2	SR-2C propeller hub
L	wing leading-edge extension (LEX)
OTW	over-the-wing contoured nacelle
OTWB	over-the-wing contoured nacelle (jet effects powerplant)
P2	SR-2C propeller
UTW	under-the-wing straight nacelle
W	wing

## SUMMARY

A semispan wing/body model with a powered highly loaded propeller has been tested to provide data on the propulsion installation drag of advanced propfan-powered aircraft. The test, conducted in the Ames Research Center's 14-Foot Transonic Wind Tunnel, is a part of a National Aeronautics and Space Administration (NASA) program to develop the technology for fuel efficient, high-speed propeller driven aircraft. The primary test objectives were to determine slipstream interference, and total powerplant installation drag penalties on a representative propfan aircraft. Additional objectives were to determine propeller performance and exhaust jet-effects. The baseline configuration had a contoured over-the-wing nacelle with the exhaust at the wing midchord. A second configuration was tested with an exhaust duct extension to permit the turbine to exhaust air at the wing trailing edge.

The semispan wing/body model had a swept supercritical wing mounted low on the body. The contoured nacelle was mated to the wing in an over-the-wing (OTW) configuration. The model was instrumented for measuring propeller forces, total configuration forces and moments, and pressure distributions over the wing and nacelle. A selected sample of the force data and pressure distributions are presented in this report.

The test was conducted at angles of attack from  $-0.5^\circ$  to  $4^\circ$  at Mach numbers ranging from 0.6 to 0.8. Tunnel total pressure was 1 atm, resulting in Reynolds numbers between 7.4 and 8.5 million. The test program was designed to assess jet-off and jet-on nacelle installation drag (jet-effects), propeller slipstream interference drag, and total powerplant installation drag. For both configurations tested, the results indicated a total powerplant installation drag of 82 counts (0.0082) at  $M = 0.8$  and a lift coefficient of 0.5. This represents about 29% of cruise drag of a typical airplane.

## INTRODUCTION

The reduction of aircraft fuel consumption is a major goal of NASA and the aerospace industry. The NASA Aircraft Energy Efficiency program has studied extensively the requirements for reducing the fuel consumption of transport aircraft. One of the primary candidates to aid in such reduction is the highly loaded, high-speed propeller, typically referred to as the propfan. Several system studies (refs. 1-4) have indicated that a propfan-powered aircraft operating at  $M = 0.8$  could achieve a 10% to 30% saving in fuel relative to a comparable turbofan-powered

aircraft. Flight speeds near  $M = 0.8$  are being considered to insure compatibility with existing airline operations. Advanced propeller designs have recently been developed that provide efficient performance at these speeds. However, the gains suggested by the system studies can be realized only if the propulsion system is properly integrated with the airframe.

In addition to generating the technology base from which airframe manufacturers can reliably design propfan aircraft, several technical issues must be resolved. Among these is the aerodynamic integration of the powerplant with the wing. One of the concerns about the propfan installation is the interference drag that may result from integration of the nacelle and propeller on a supercritical wing. The resultant interference effects are dependent upon the nacelle/wing interactions along with the Mach number and swirl increment generated in the slipstream. A slipstream simulator test was conducted in 1978 to evaluate experimentally these interference effects (ref. 5). A flow-through, ejector-powered nacelle located ahead of the wing was used to simulate the propeller slipstream flow. This approach permitted simulating various propeller parameters to obtain a basic understanding of power effects on the wing. Recently, a more realistic representation was obtained from a wind-tunnel test on a propfan powered model (ref. 6). This model had a highly loaded, eight-bladed propeller mounted on a semispan wing. The nacelle was mated to the supercritical wing in an under-the-wing (UTW) configuration. Nacelle installation drag, propeller slipstream interference drag, and total powerplant installation drag were measured. With proper fillets at the wing-nacelle intersections, it was demonstrated that the total powerplant installation drag at  $M = 0.8$  was about 6% of the airplane cruise drag and this compared favorably with current turbofan installations.

A number of propfan-powered aircraft concepts has been developed (refs. 7-9). These designs considered mating the propfan on an advanced design, high-aspect ratio supercritical wing. The design of reference 7 was a UTW configuration with the wing mounted high on the body; references 8 and 9 considered an OTW nacelle on a low-wing configuration. All of the designs incorporated nacelle contouring. In addition to these design geometries, aft-mount locations are being considered for powerplants with either tractor or pusher propellers. The configuration selected for the first test of an OTW design was that provided by the Douglas Aircraft Co. (ref. 9). The reasons for selecting this configuration were twofold. First, one design was a nacelle contoured for the wing geometry which had been previously tested and reported on in reference 6. This had the obvious advantage of reduced cost in terms of model hardware. Second, the design was low wing, which appeared more appropriate for commercial transport applications.

The results of the test reported herein are for an OTW nacelle configuration with nacelle contouring to alleviate potentially adverse flow conditions between the nacelle and the fuselage. Propeller performance characteristics, pressure distributions over the wing and nacelle, powerplant installation losses, and fluorescent oil flow visualization studies were made.

## MODEL DESCRIPTION AND INSTRUMENTATION

The model configuration was derived from a supercritical wing incorporating 1975 design technology which demonstrated good drag-rise characteristics near  $M = 0.8$ . The turboprop nacelle was mated to the wing in an over-the-wing configuration. The nacelle was blended and shaped for optimum aerodynamic integration (refs. 9 and 10).

Results of an earlier powered test (ref. 11) of the UTW configuration in the Ames 14-Foot Transonic Wind Tunnel indicated that the installation of the nacelle and propeller swirl significantly affected the wing flow. To alleviate this flow problem, a wing modification was designed (ref. 9) that included adding a leading-edge extension (LEX) to the baseline wing. This proved very beneficial in achieving the low installation losses and was investigated in this series of tests.

Photographs of the semispan wing/body wind-tunnel models mounted in the Ames 14-Foot Transonic Wind Tunnel are shown in figure 1. Figure 1(a) shows a front view of the semispan model. Figures 1(b) and 1(c) show front and rear views of the nacelle/wing installation, respectively, without the LEX installed. The configuration with the LEX installed and the nacelle geometry shown in figures 1(b) and 1(c) is hereinafter denoted as the baseline configuration (with or without the propeller). Figures 1(d) and 1(e) show front and rear views, respectively, of the configuration with the exhaust duct extended to the wing trailing edge. These two photographs also show the LEX mated to the wing (inboard from the nacelle). The propeller axis was aligned downward  $3.75^\circ$  (droop) and inboard  $2^\circ$  (toe-in) to minimize the cyclic blade loads caused by wing sweep and angle of attack. (The procedure used to determine this has been reported in reference 12.)

### Model Details

The model scale was 12% of a representative 180 passenger transport. Model planform details are shown in figure 2(a). Fine grit was applied near the wing leading edge to produce an all turbulent boundary layer. On the wing upper surface, the grit was applied 11.7 cm (4.6 in.) from the leading edge, or at the 15% chord line, whichever was less. On the wing lower surface, it was applied 15.9 cm (6.25 in.) from the leading edge. The LEX was added between the inboard side of the nacelle and the body. Wing airfoil coordinates are provided in reference 13 and the LEX coordinates are given in reference 9.

The nacelle was scaled based on an  $M = 0.8$  transport powered by two 30,000-hp engines (ref. 3). Nacelle geometry is shown in figure 2(b) and the cross-section geometry and coordinates are provided in figure 2(c). The technique used to derive the nacelle contouring is described in reference 9. The contouring maintained the longitudinal cross-sectional area distribution of the straight nacelle (ref. 13), while the centers of these areas were displaced horizontally and vertically to conform to the flow streamlines of the baseline wing without power effects.

The model powerplant (excluding the exhaust nozzle) was the same as that described in reference 6. Geometric details of the exhaust nozzle and calibration procedures can be found in reference 14. The propeller used the Hamilton Standard SR-2 (unswept) eight-blade propfan geometry. Blades for this model were fabricated from molded carbon-epoxy composite and were designated SR-2C. The propeller diameter was 0.622 m (2.04 ft). The pitch angle of all blades was the same and could be varied manually.

The turbine motor was a 6-stage axial flow design driven by compressed air. A 24-channel slip ring was located at the rear of the turbine. Instrumentation signals from the hub balance and the propeller blade strain gages were passed through a hole in the motor shaft and out through the slip rings to the nonrotating system. For the baseline configuration, turbine exhaust air was ducted over the wing and exited the exhaust pipe at the wing midchord. For the extended duct configuration, turbine exhaust was at the wing trailing edge. Pitot probes (thrust rake) and static wall pressure taps were used to measure the exhaust thrust. A section of stainless steel honeycomb located upstream of this instrumentation removed any residual swirl from the motor exhaust. This permitted accurate calibration of the thrust rake and exhaust nozzle (ref. 14).

#### Balance and Pressure Instrumentation

Total configuration normal- and axial-force and pitching moment were obtained from a five-component force-moment floor balance. The balance capacity in the normal- and axial-force directions were 53,400 N (12,000 lb) and 4,450 N (1,000 lb), respectively. Propeller forces and moments were obtained from a six-component rotating propeller balance located within the hub. The balance capacity was 2,000 N (450 lb) in the axial-force direction, 2,225 N (500 lb) in the normal- and side-force directions, and 745 N-m (550 ft-lb) in rolling moment.

The coordinates of all model pressure instrumentation are given in reference 13, and consisted of the following: (1) 239 wing static orifices distributed over 8 spanwise stations; (2) 103 nacelle static orifices distributed over 12 longitudinal stations; (3) 25 hub-cavity static orifices; (4) 6 internal duct static orifices; (5) 6 nacelle-base static orifices; and (6) 21 internal duct total probes. These pressures were recorded using two 6-module Scanivalve assemblies. Other model instrumentation consisted of a temperature rake in the exhaust duct, strain gages on the propeller blades for measuring unsteady blade stresses, 17 pressure transducers (Kulites) for measuring acoustic pressures on the wing and body, and probes to measure the motor plenum temperature and pressure. Additional instrumentation, such as accelerometers and motor bearing temperatures, were provided to monitor the health of the turbine system for wind tunnel safety.

#### Installation

There was a gap of about 4.4 cm (1.75 in.) between the bottom of the body and the tunnel floor. This permitted some of the tunnel floor boundary-layer flow to

pass beneath the body. A shroud was placed around the wing floor-mount to prevent this flow from impinging on the balance. Throughout the test the wind-tunnel floor slots were sealed. The effect of flow passing beneath the body on the unpowered test results were described in references 13 and 15.

#### TEST PROCEDURE

The test variables were Mach number, angle of attack, propeller blade pitch angle, and nozzle exhaust pressure ratio (EPR). Tunnel total pressure was 1 atm throughout the test. The Reynolds number based on mean aerodynamic chord (without LEX) varied from  $7.4 \times 10^6$  at  $M = 0.6$  to  $8.5 \times 10^6$  at  $M = 0.8$ . For the jet effects configurations (blades off), EPR was varied from 1.0 to approximately 2.0 at each test Mach number, while angle of attack was held constant. Note that EPR = 1.0 represents a jet-off point, that is, no air was flowing through the exhaust nozzle. For the blades-on configurations, propeller speed was varied from windmill (jet-off) to 8,500 rpm in approximately 500 rpm increments, or to the maximum speed possible within power or safety limitations, whichever occurred first. Note that propeller speed and EPR could not be varied independently. Maximum propeller speed was based upon maintaining a positive margin of safety with a maximum unbalanced load resulting from blade failure. This occurs at 8,500 rpm with a loss of four adjacent blades.

Model angle of attack was varied from  $-0.5^\circ$  to  $4^\circ$ . Data were obtained at blade pitch angles of  $54.8^\circ$ ,  $55.6^\circ$ , and  $56.6^\circ$  for Mach numbers 0.6, 0.7, and 0.75 to 0.8, respectively; the design angles were  $55^\circ$ ,  $56^\circ$ , and  $57^\circ$ , respectively. All angles were measured at the 75% radius station.

#### DATA REDUCTION

The procedures used to obtain thrust removed longitudinal characteristics and interference drags have been described in detail in reference 6. For the OTW configuration, the equations cited in the reference were modified to account for the geometric differences in the location of the exhaust and propeller thrust vectors with respect to the model center of gravity. All coefficients presented in the airplane reference system use the reference area and mean aerodynamic chord of the wing without the LEX.

The equation for net thrust has four terms representing six independent measurements. Additionally, the equation for the slipstream interference drag requires 10 independent measurements, each subject to experimental uncertainty (ref. 6). The uncertainty in the slipstream interference drag, based upon repeatability, has been estimated to be  $\pm 0.0008$ . The maximum uncertainties in the floor balance readings, based on repeatability, have been estimated to be  $\pm 0.0020$  in lift coefficient and  $\pm 0.0003$  in drag coefficient.

The interference drag values were obtained from the difference in drag from two different configurations at constant values of lift coefficient and EPR. To obtain a drag difference at constant EPR and lift coefficient, it was necessary to obtain thrust removed drag polars by interpolation. The procedure to obtain the installation drag characteristics is described below:

1. At each angle of attack, the blades-on thrust-removed data were plotted as a function of net thrust coefficient. For uniform values of net thrust coefficient, lift-, drag-, and pitching moment coefficients were obtained, along with the corresponding value of EPR.

2. At each angle of attack, the blades-off, thrust-removed, jet-effects data were plotted as a function of EPR. The EPRs from step 1 were used to obtain the aerodynamic coefficients. In addition, coefficients were obtained at an EPR = 1.0 (jet-off).

3. The interpolated data were then plotted as a function of lift coefficient for each value of net thrust coefficient (blades on) and for the corresponding EPR (blades off).

4. Differences were then taken between the two drag polars at constant values of lift coefficient, and by implication, at constant EPR.

The procedure outlined above is configuration dependent, since it uses the measured installed thrust characteristics of the propeller and not the isolated characteristics. This allows the true aerodynamic interference characteristics to be determined. If the isolated propeller data are used, any changes in propeller performance would be interpreted as aerodynamic interference.

## RESULTS AND DISCUSSION

The test results are presented in figures 3 through 20. Unless otherwise noted, the data presented are at the cruise conditions of  $M = 0.8$  at an angle of attack of  $2^\circ$ .

### Pressure Distributions

Wing pressure distributions showing power and configuration effects are presented in figures 3 through 8. The discussion of the pressure results is limited to the nominal cruise condition of  $M = 0.8$  at an angle of attack of  $2^\circ$ . All chordwise pressure locations have been referenced to the wing leading edge without the LEX; thus, results are shown at negative  $x/c$  for span stations 0.25 through 0.418. Along the nacelle centerline ( $\eta = 0.481$ ), the nacelle pressures along the upper and lower surfaces have also been referenced to the wing-leading edge and local chord length without the LEX; thus, there are negative values of  $x/c$  at this semispan station.

The effect of the jet on the wing pressure distributions is shown in figure 3 for the baseline configuration and in figure 4 for the extended duct. Note that both upper and lower surface pressures are shown with the same symbol. At  $\eta = 0.365$ , there was a strong shock wave at approximately  $x/c = 0.15$  which originated at the wing/nacelle juncture. This was also evident from the flow visualization studies, to be described later. However, there was no evidence of shock induced separation. For the baseline configuration there was generally no effect of the jet on the wing pressure distributions, except at  $\eta = 0.481$  (fig. 3(b)). At this station, for  $x/c > 0.5$ , the flow was separated behind the duct exit with jet off (EPR = 1.0). With jet on, the pressure coefficient increased slightly. Note that an EPR = 1.963 represents a supersonic pressure ratio. For the extended duct (fig. 4) the jet has generally no effect on the wing pressures. Note that at  $\eta = 0.481$ , the wing upper surface pressure taps were covered by the nacelle and duct extension. The pressures shown are those along the nacelle upper surface centerline.

The effect of propeller speed on the wing pressure distributions is shown for the baseline and extended duct configurations in figures 5 and 6, respectively. An EPR = 1.0 represents the windmill condition (jet off) and the corresponding RPM shown was the windmill speed. The direction of propeller rotation was up-inboard, which increased the local angle of attack of the inboard airfoil sections and decreased the local angle outboard. Inboard, the effect of power generally increased the negative pressure peaks; outboard, the pressure peaks decreased. The results are consistent with the direction of propeller rotation. At the first station inboard from the nacelle,  $\eta = 0.418$ , the pressure distributions indicate a possible flow separation between  $x/c = 0.1$  to about 0.35, which becomes more severe with increasing power. This will be discussed later in the flow visualization section.

A comparison of the wing pressure distributions for the wing alone, baseline, and extended duct configurations is shown in figures 7 and 8. For blades off (fig. 7), there are only minor differences in the pressure distributions between the baseline and extended-duct configurations (squares and diamonds). Compared with the wing, there was a greater effect of the nacelle inboard than outboard. At  $\eta = 0.250$ , the suction peak on the upper surface has been significantly reduced. At  $\eta = 0.365$ , the shock has moved closer to the wing leading edge, but there are no indications of any significant flow separations (indicated by the smooth expansion behind the shock). At the first station inboard from the nacelle ( $\eta = 0.418$ ), placing the nacelle on the wing increased the suction peak and appeared to cause flow separation over much of the chord.

The addition of the propeller (fig. 8) appears to make the flow conditions inboard slightly more severe than for blades off. Outboard there appears to be little difference among the configurations. These results are consistent with the direction of propeller rotation.

## Flow Visualization Studies

The baseline and extended-duct configurations were studied using fluorescent oil to visualize the boundary layer flow. Photographs taken under ultraviolet light are presented in figure 9. All flow visualization studies were conducted at an angle of attack of 2°.

The baseline jet effects configuration with jet off is shown in figure 9(a). Note the separation at the duct exit with a strong spanwise pressure gradient. Inboard, a separation line emanates from the wing/nacelle juncture. No similar separation occurs outboard. Jet-on effects are shown in figure 9(b). The separation at the duct exit has been eliminated and the spanwise pressure gradient is reduced. Figure 9(c) shows the extended duct configuration with jet on. Although not shown, there were no significant differences in the oil flows to distinguish whether the jet was on or off. Compared to the baseline (fig. 9(b)), the spanwise pressure gradient outboard of the nacelle has been reduced considerably, as indicated by the reduced spanwise component of the oil flow lines.

The effect of the propeller near windmill speed is shown in figure 9(d). At the duct exit, the low velocity exit-flow is similar in appearance to the jet-off condition (fig. 9(a)). Note the vortex-like pattern at the wing trailing edge. The upper surface flow with the propeller operating near cruise conditions is shown in figure 9(e). The flow in the vicinity of the inboard wing/nacelle juncture shows evidence of flow separation, which is indicated by the reversed flow just downstream from the separation line. The separated region has increased in size which is consistent with the increased local angle of attack caused by the propeller slipstream.

Figures 9(f) and 9(g) show the extended duct configuration at the same two propeller speeds as the baseline, figures 9(d) and 9(e). A comparison of these photos shows no significant effect of the duct on the flow over the inboard panel. Outboard of the nacelle, however, the duct has reduced the spanwise flow component.

The baseline and extended duct boundary layer flow are shown in figures 9(h) and 9(i), respectively, at cruise thrust and  $M = 0.78$ . For the baseline (fig. 9(h)) the boundary layer flow is similar to the flow at  $M = 0.8$  (fig. 9(e)). For the extended duct configuration (fig. 9(i)), there is a new separation outboard of the nacelle that was not present at  $M = 0.8$ . This Mach number sensitivity suggests a wing shock/boundary layer interaction; wherein the shock at  $M = 0.78$  has moved to a point on the wing where the pressure gradient is sufficiently positive to cause the boundary layer to be separated by the shock interaction.

Recall that the nacelle contours were designed for the baseline wing without the LEX and did not include power effects (ref. 9). In the presence of the propeller, the baseline wing/UTW nacelle without the LEX showed separated flow and strong pressure gradients inboard of the nacelle (ref. 6). Because the LEX significantly improved the wing flow (ref. 6), the decision was made to test the nacelle with the LEX installed. At this time it is not clear whether the flow conditions shown by

the oil flows are due to improper nacelle contours with the LEX installed, whether the contours were too sharp for transonic flow conditions, or whether the power effects on the streamlines are generally more sensitive for an OTW than for a UTW configuration.

### Propeller Performance

The propeller power- and thrust-coefficient are shown as a function of advance ratio in figures 10 and 11. Figure 10 shows the effects of changes in Mach number. Note that the highest value of advance ratio corresponds to the propeller at windmill and the lowest value to the maximum RPM tested. The data are shown at the appropriate blade-pitch angle for each Mach number. The slopes of the power and thrust curves increase with increasing Mach number up to  $M = 0.75$ . At Mach numbers of 0.75 and higher, the slopes are generally the same. Up to  $M = 0.75$ , the change in slope was caused primarily by changes in blade-pitch angle and, secondarily, by Mach-number effects. This is evidenced by the constant slope of the curves in the Mach number range 0.75 to 0.8, where the blade-pitch angle was constant. Isolated propeller data also exhibit this same characteristic.

The effect of angle of attack on propeller thrust- and power- coefficients is shown in figure 11. The slopes of the curves are essentially the same, but the windmill speed decreased (increased  $J$ ) with increasing angle of attack. Note that at  $\alpha = 0.5^\circ$ , the propeller angle of attack is  $-3.25^\circ$  with respect to the freestream velocity and is  $0.25^\circ$  when  $\alpha = 4^\circ$ . The differences shown in windmill speed over the  $3.5^\circ$  change in angle of attack are equivalent to about  $0.3^\circ$  change in blade pitch angle.

### Thrust Removed Characteristics

Thrust-removed lift-, drag-, and pitching-moment coefficients are shown as a function of net thrust in figure 12. Data are presented for several angles of attack at  $M = 0.8$ . Note that there is a negative net thrust coefficient when the propeller is windmilling. At this condition, the propeller produces drag.

For the baseline configuration (fig. 12(a)), the lift initially decreased with increasing thrust from windmill at all angles of attack. Further increases in thrust resulted in increased lift. Generally, the lift was restored to the windmill value at a thrust coefficient of about 0.02; beyond 0.02 the lift was greater than the windmill value.

From windmill, the effect of increasing thrust on the pitching moment was destabilizing up to thrust coefficients of about 0.013; above this value, further increases were then stabilizing. This pitching-moment characteristic is consistent with the variation in lift owing to power.

The drag increased continuously with increasing thrust. This drag increase provides evidence that the slipstream interference drag increases with increasing thrust. This is consistent with the results seen in the oil flow photographs.

The same thrust removed characteristics are presented in figure 12(b) for the extended duct configuration. With the turbine exhaust at the wing trailing edge the lift generally increased with thrust. The lift increase resulted from some swirl recovery at the leading edge. The baseline configuration also had swirl recovery, but the effect of the jet exhausting at the wing midchord possibly reduced the section lift more rapidly than the increase provided by swirl recovery.

Generally, the effect of increasing thrust was destabilizing over the entire thrust range tested. The slipstream was destabilizing and this effect is supported by the pressure distributions. Evidently, some of the swirl momentum was recovered as leading edge thrust. Inboard, the slipstream produced higher suction peaks and higher section lift. Since these airfoil sections are forward of the center of gravity the result was destabilizing.

Initially, the drag usually decreased with a slight increase in thrust from windmill. However, the level indicated was within the experimental uncertainty of the measurements; thereafter, there was a continuous drag increase with thrust, similar to the baseline configuration. The initial drag decrease was possibly caused by restoring leading edge thrust through recovery of swirl momentum. The drag increase thereafter was probably caused by the viscous slipstream interference flow over the wing.

#### Longitudinal Aerodynamic Characteristics

Longitudinal thrust removed force and moment characteristics are presented in figures 13 through 16. The data are presented at constant values of net thrust and/or EPR. Note that for semispan configurations, the absolute drag levels are not representative of a full span configuration. There are additional contributions to the drag caused by the tunnel-floor boundary layer acting on the underside of the body and the reflection plane possibly being altered by the crossflow boundary layer with changes in model angle of attack. However, it should be emphasized that reliable increments can be obtained from semispan testing.

Results are shown for the baseline configuration in figure 13. At each test Mach number the blades-on, blades-off, and wing/body (no nacelle) configurations are compared. For blades on, the net thrust coefficient indicated on the figure is the appropriate value for each Mach number. For blades-off, the EPR is seen to be identical to that with blades on.

At all Mach numbers the lift curve slope was independent of variations in the configuration. For fixed angle of attack, the lift for the blades-off and jet-on configurations was lower than it was for the wing/body. For blades-on at cruise power, some of the loss of lift which occurred when the nacelle was added was restored as a result of the high suction pressure peaks caused by swirl in the

slipstream. The stability was markedly reduced when the nacelle was added, and it decreased further with the addition of the propeller.

For lift coefficients near cruise ( $C_L = 0.5$ ), adding the nacelle increased the drag increments (nacelle-on minus wing/body) as the Mach number was increased. Addition of the propeller increased the drag increment even further. This will be described later in the interference drag section. Figure 14 presents similar data for the extended duct configuration. The trends are generally similar to those described for the baseline configuration.

The effect of net thrust on the thrust removed aerodynamic characteristics for the baseline and extended duct configurations at  $M = 0.8$  are presented in figure 15. For either configuration the level of thrust has little effect on the thrust-removed parameters.

The two blades-on configurations at cruise thrust are compared with the wing/body in figure 16. Generally, there were no differences in the lift-curve slope between the configurations. The lift for the extended duct configuration was slightly higher than for the baseline, and both had higher lift than did the wing/body. The suction peaks over the leading edge influenced by the propeller were increased, and the lower surface pressures were less negative in those regions affected by the jet (fig. 8). The net effect was an overall increase in lift.

The combination of nacelle, jet, and propeller was destabilizing, as previously described. There were only minor differences in the stability for the blades-on configurations, although the moment level was more negative with the extended duct installed. The drag was generally the same for the two blades-on configurations. At the cruise lift coefficient of 0.5, the installation drag was about 82 counts (0.0082). The breakdown of the various drags (which make up the total installation drag) is described in the next section.

#### Installation Drag Increments

The total powerplant installation drag is the sum of the nacelle installation drag and slipstream-interference drag. The procedure for obtaining these drags has been fully described in reference 6. A brief review of that procedure is described below.

Slipstream interference drag is defined as the drag difference between blades-on and blades-off for fixed lift- and thrust-coefficients, and EPR. Nacelle-installation drag is the difference in drag between blades-off, jet-on and the wing/body, evaluated at the EPR for blades on. Total powerplant installation drag is the sum of these two interference drags, or the drag difference between blades-on jet-on and the wing/body at fixed lift- and thrust-coefficients.

Interference-drag results are presented in figures 17 through 19 for the OTW configurations. Figure 17 shows the effect of thrust on the interference drags at a lift coefficient of 0.5. For the baseline (fig. 17(a)), at all Mach numbers the

nacelle installation drag decreased, and the slipstream interference drag generally increased with increasing thrust. The slipstream interference drag increased because the swirl caused flow separation and increased the strength of the shock wave inboard from the nacelle. The total powerplant installation drag ( $C_{D_{INS}}$ ) increased between  $M = 0.6$  and  $M = 0.8$ . The larger increase between  $M = 0.7$  to  $M = 0.75$  was caused by the onset of compressibility effects.

For the extended duct configuration (fig. 17(b)), the nacelle installation drag increased with increasing thrust and the slipstream interference drag decreased, which is opposite to the trends for the baseline configuration. Note the high slipstream interference drag at  $M = 0.78$ , consistent with the oil flow photograph (fig. 9(i)). At  $M = 0.8$  there was no shock outboard of the nacelle and the slipstream drag decreased. This trend is reflected in the total powerplant installation drag.

The installation drag characteristics as a function of Mach number are shown for different lift coefficients (constant thrust) in figure 18. For both configurations, the nacelle installation drag increased with increasing lift; the slipstream interference drag decreased. The combined effect was an increase in the total powerplant installation drag. Recall that  $C_{D_{NAC}}$  is referenced to the wing/body configuration;  $C_{D_{SS}}$  to the blades-off, jet-on configuration.

The interference drags for the baseline and extended duct configurations are compared at the same lift- and thrust-coefficients in figure 19. Except at  $M = 0.8$ , the extended duct nacelle installation drag was lower than the baseline. The differences in slipstream interference drag between the two configurations were all within the experimental uncertainty of the measurements. At  $M = 0.8$  both configurations had a total powerplant installation drag of 82 counts. This level is about 29% of a typical aircraft cruise drag.

Figure 20 compares the total installation drag for the OTW (circles and squares) and UTW (diamonds) configurations. The lift coefficient is 0.5, but the UTW configuration is at a higher net thrust. The UTW data shown are with the LEX, but do not include the fillet and strake (which had even lower installation drag). The total powerplant installation drag for the OTW is about 29% of airplane cruise drag (assuming a cruise  $L/D = 17.5$ ) and about 11% for the UTW (cruise  $L/D = 16$ ). With the fillet and strake added, the data of reference 6 showed that the powerplant installation drag for the UTW could be as low as 6% of the cruise drag.

The powerplant installation drag for the OTW configurations are obviously too high. The nacelle contours were obtained by matching the streamlines about the clean wing, with the constraint that the powerplant must fit within the body (ref. 9). Because the objective of the study was to evaluate what could be achieved by nacelle contouring, power effects were not included, but were to be treated using wing modifications. The clean wing streamlines were obtained from an incompressible surface panel method using unknown source and dipole singularities to satisfy the zero normal flow condition at control points located on the panels (ref. 17). The OTW nacelle was designed for testing with the clean wing (without the LEX).

However, because the LEX significantly improved the adverse flow conditions on the baseline wing with the UTW nacelle (ref. 6), the test was conducted with the LEX installed. No redesign effort was made since it was felt that the contours would not be greatly different. At this time, it is not known whether the high drag levels were caused by testing with the LEX installed or were due to the contours being too sharp for transonic flow. It should be noted that the nacelle contouring began near the leading edge of the baseline wing. With the LEX installed, this contouring probably begins too far aft of the leading edge of the LEX.

More work is required to determine if the installed drag for an OTW configuration can be reduced to near those of the UTW installation. Testing without the LEX would be one approach to verify the design methods used. Currently, plans are under way to test a contoured OTW nacelle on a new, high aspect ratio wing. The nacelle was designed with the duct extending to the wing trailing edge. Results from this test should aid in determining both the design philosophy and whether it is possible to obtain low installed drag on an OTW nacelle for wings mounted low on the body.

#### CONCLUSIONS

Tests were conducted on a semispan wing/body model with a powered propeller in the Ames 14-Foot Transonic Wind Tunnel. The swept supercritical wing was tested with a wing leading-edge extension (LEX) and a contoured over-the-wing nacelle. The test was conducted at a total pressure of 1 atm at Mach numbers from 0.6 to 0.8 and angles of attack from  $-0.5^\circ$  to  $4^\circ$ . The test results support the following conclusions:

1. The addition of the nacelle caused a shock wave inboard of the nacelle, originating at the wing/nacelle juncture.
2. With the propeller operating at cruise power, the inboard shock was strengthened and flow separation occurred on the wing upper surface.
3. Extending the exhaust duct to the wing trailing edge resulted in a strong shock wave outboard from the nacelle at  $M = 0.78$  (propeller on).
4. With the jet exhaust at the wing midchord (baseline configuration), turning the jet on (propeller off) reduced the lift. The lift loss was not restored until cruise power was reached (EPR about 1.8). At all jet on power settings, extending the duct to the wing trailing edge resulted in increased lift from the jet-off value.
5. Adding the propeller increased the suction pressure peaks inboard from the nacelle because the up-inboard propeller rotation increased the local angle of attack of the wing.

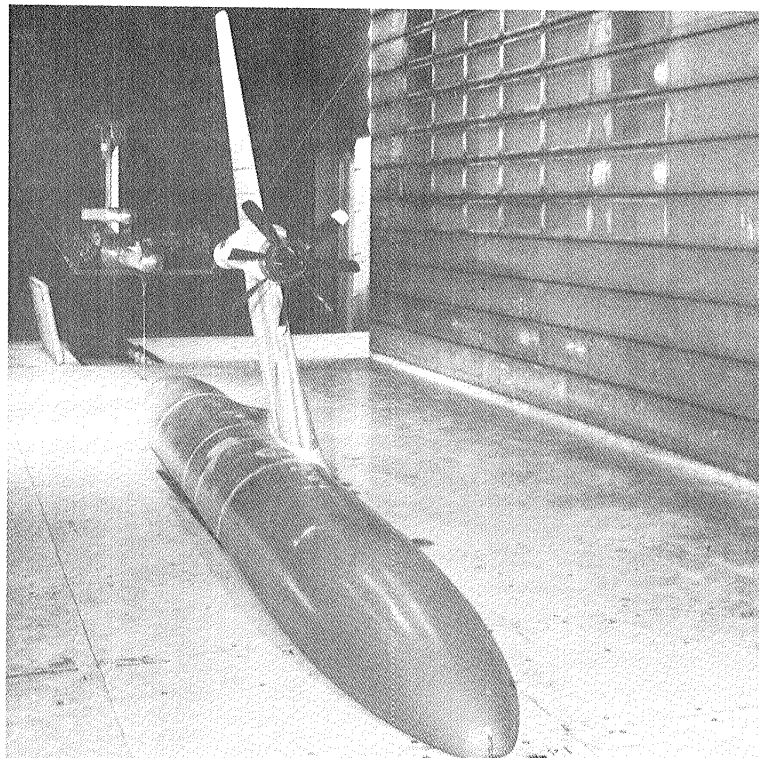
6. For both configurations, baseline and extended duct, the installation drag penalty ( $M = 0.8$ ,  $C_L = 0.5$ ) was 82 drag counts, about 29% of a typical airplane cruise drag. The highest installed drag was 88 counts for the extended duct configuration at  $M = 0.78$  (31% of cruise drag).

7. The nacelle was designed for the baseline wing without the LEX. It is not known whether the high drag levels were caused by the nacelle/LEX geometry or by the nacelle contours being too sharp for transonic flow conditions.

## REFERENCES

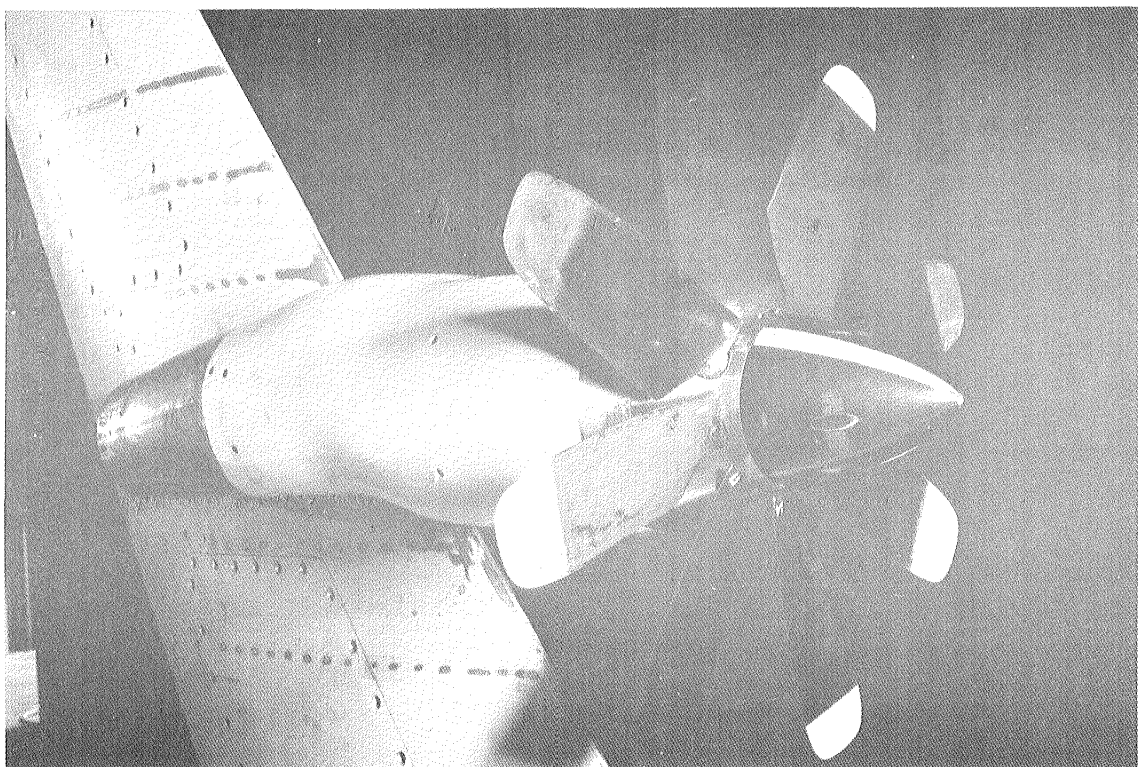
1. Hopkins, J. P.; and Wharton, H. E.: Study of the Cost/Benefit Tradeoffs for Reducing the Energy Consumption of the Commercial Air Transportation System, Lockheed-California Co. NASA CR-137927, 1976.
2. Kraus, E. F.; and Van Abkoude, J. C.: Cost/Benefit Tradeoffs for Reducing the Energy Consumption of the Commercial Air Transportation System, vol. I: Technical Analysis, Douglas Aircraft Co. NASA CR-137923, 1976.
3. Staff: Energy Consumption Characteristics of Transports Using the Prop-Fan Concept, Boeing Commercial Airplane Co. NASA CR-137938, 1976.
4. Dugan, J. F.; Bencze, D. P.; and Williams, L. J.: Advanced Turboprop Technology Development. AIAA Paper 77-1223, 1977.
5. Welge, H. R.; and Crowder, J. P.: Simulated Propeller Slipstream Effects on a Supercritical Wing, Douglas Aircraft Co. NASA CR-152138, 1978.
6. Levin, Alan D.; Smith, Ronald C.; and Wood, Richard, D.: Aerodynamic and Propeller Performance Characteristics of a Propfan-Powered, Semispan Model. NASA TM 86705, 1985.
7. Aljabri, Abdullah S.; and Swearengen, John M.: Analysis of Mach Number 0.8 Turboprop Slipstream Wing/Nacelle Interactions, Lockheed-Georgia Co., NASA CR-166419, 1982.
8. Samant, Satish S.; Hultman, Don; Lines, T. R.; Yu, N. J.; and Rubbert, Paul E.: Analysis and Design of Prop-Fan Nacelle Installations at Transonic Speeds, Boeing Commercial Airplane Co., NASA CR-166376, 1982.
9. Welge, H. Robert; Newhart, Dan H.; and Dahlin, John A.: Analysis of Mach Number 0.8 Turboprop Slipstream Wing/Nacelle Interactions, Douglas Aircraft Co. NASA CR-166214, 1981.
10. Welge, H. Robert: Prop-Fan Integration at Cruise Speeds, AGARD Paper 33, presented at AGARD Symposium on Aerodynamics of Power Plant Installation, Toulouse, France, May 11-14, 1981.
11. Smith, Ronald C.; and Levin, Alan D.: Propfan Installation Aerodynamics of a Supercritical Swept Wing Transport Configuration. AIAA Paper 81-1563, 1981.
12. Mendoza, J. P.: Interference Effects of Aircraft Components on the Local Blade Angle of Attack of a Wing Mounted Propeller. NASA TM 78587, 1979.
13. Levin, Alan D.; and Smith, Ronald C.: Installed Nacelle Drag-Improvement Tests of a  $M = 0.8$  Turboprop Transport Configuration. NASA TM 84302, 1983.

14. Shumpert, Paul K.: Over-the-Wing Exhaust Nozzle Calibration for a Model 123<sup>4</sup> Air Turbine Motor. Tech Development, TR83-113, 1983.
15. Levin, Alan D.; and Smith, Ronald C.: Propfan Propulsion Integration Test Techniques. AIAA Paper 82-0577, 1982.
16. Vernon, David F.; Page, Gregory S.; and Welge, H. Robert: Propfan Experimental Data Analysis, Douglas Aircraft Co. NASA CR-166582, 1984.
17. Hess, J. L.: The Problem of Three-Dimensional Lifting Potential Flow and Its Solution by Means of Surface Singularity Distribution. Computer Methods in Applied Mechanics and Engineering, vol. 4, 1974, pp. 283-319.



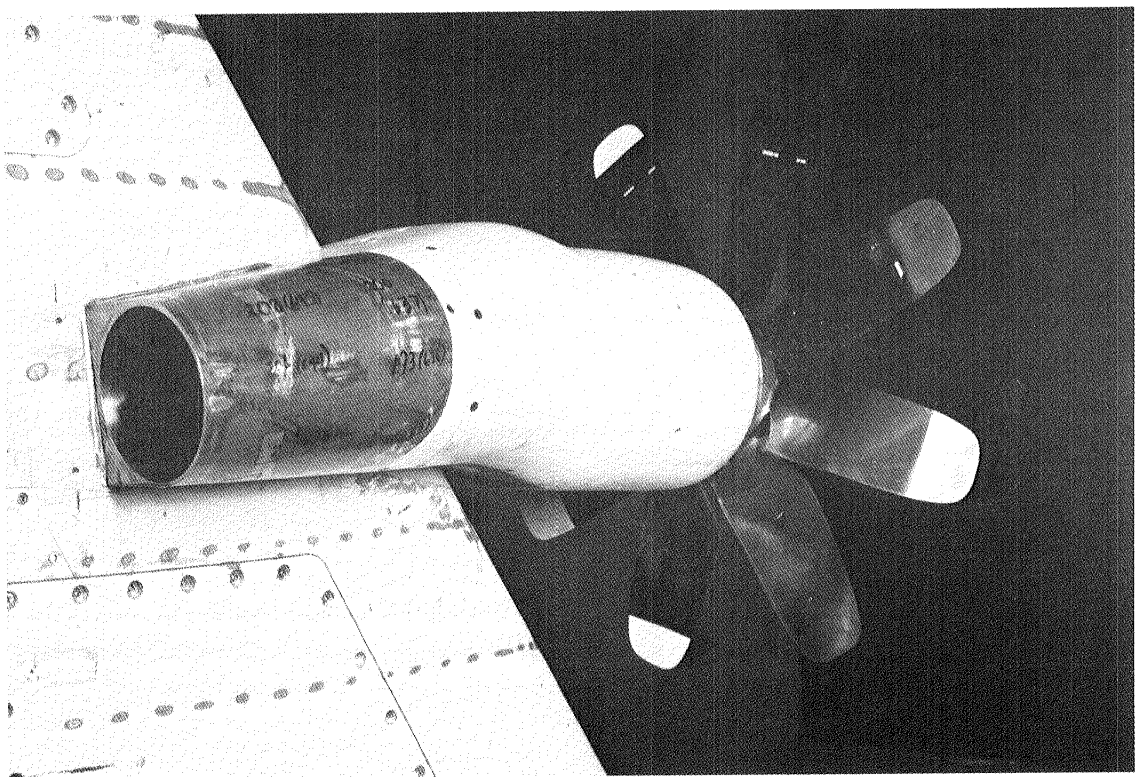
(a) Wing/body model.

Figure 1.- Model mounted in the 14-foot tunnel.



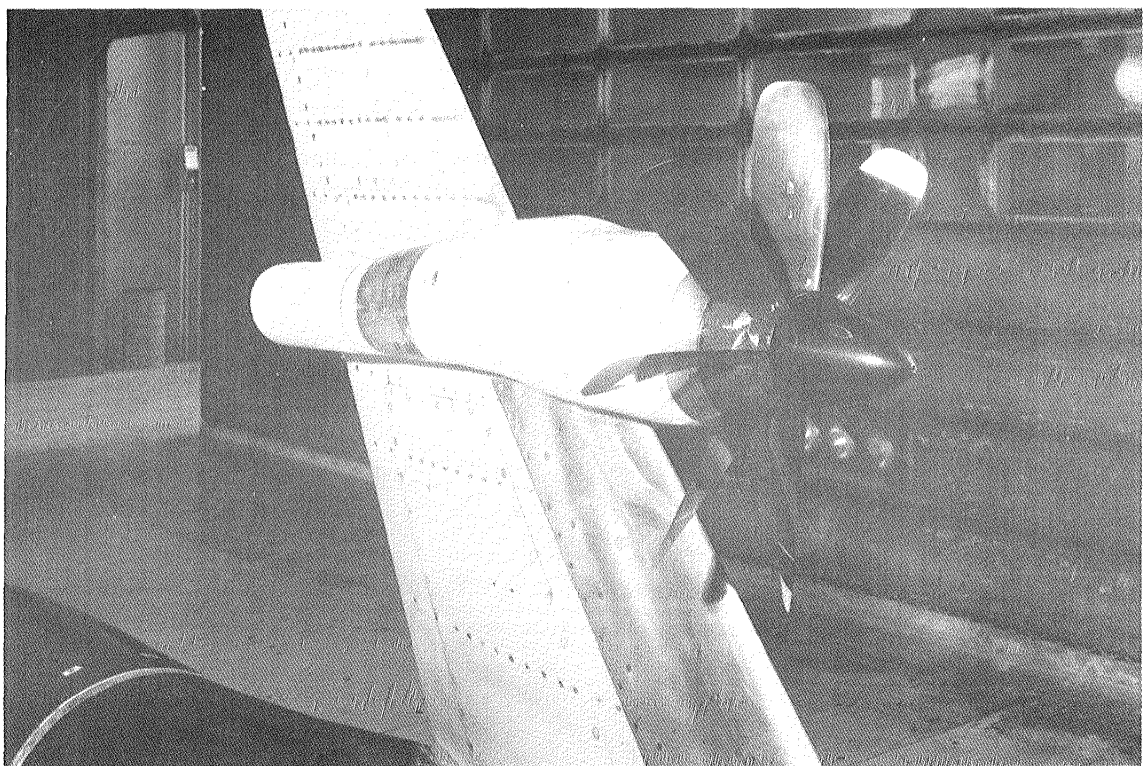
(b) OTW nacelle, front view.

Figure 1.- Continued.



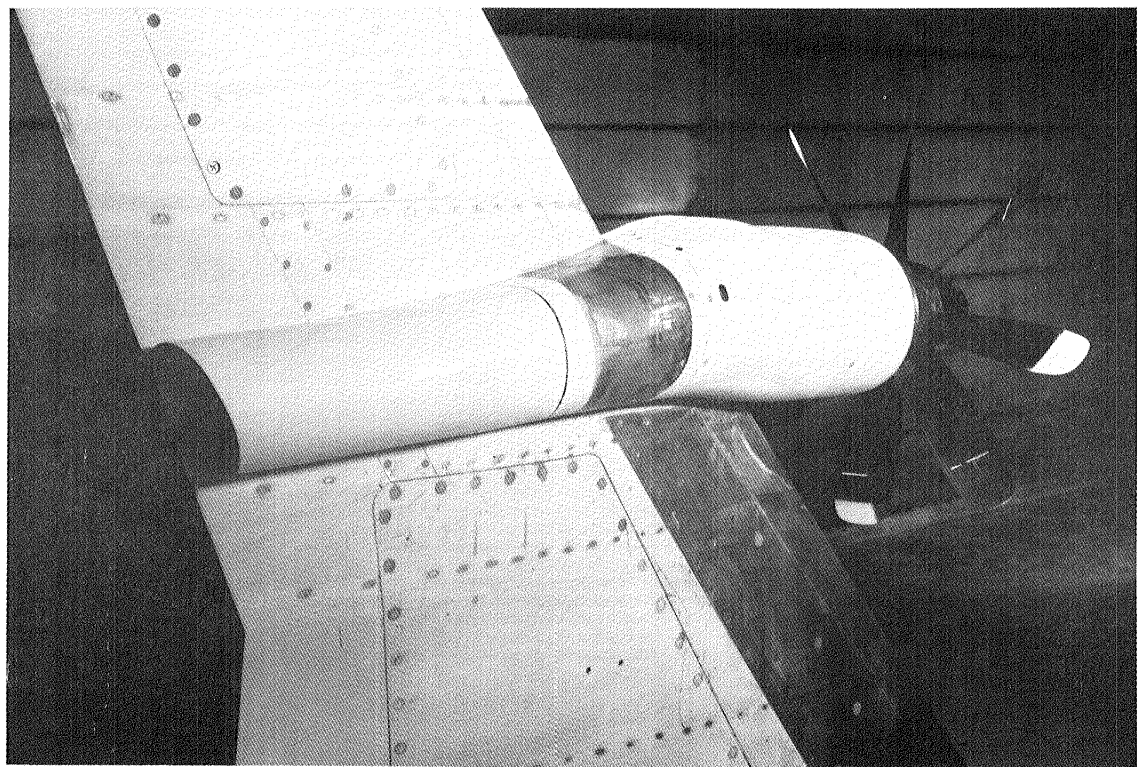
(c) OTW nacelle, rear view.

Figure 1.- Continued.



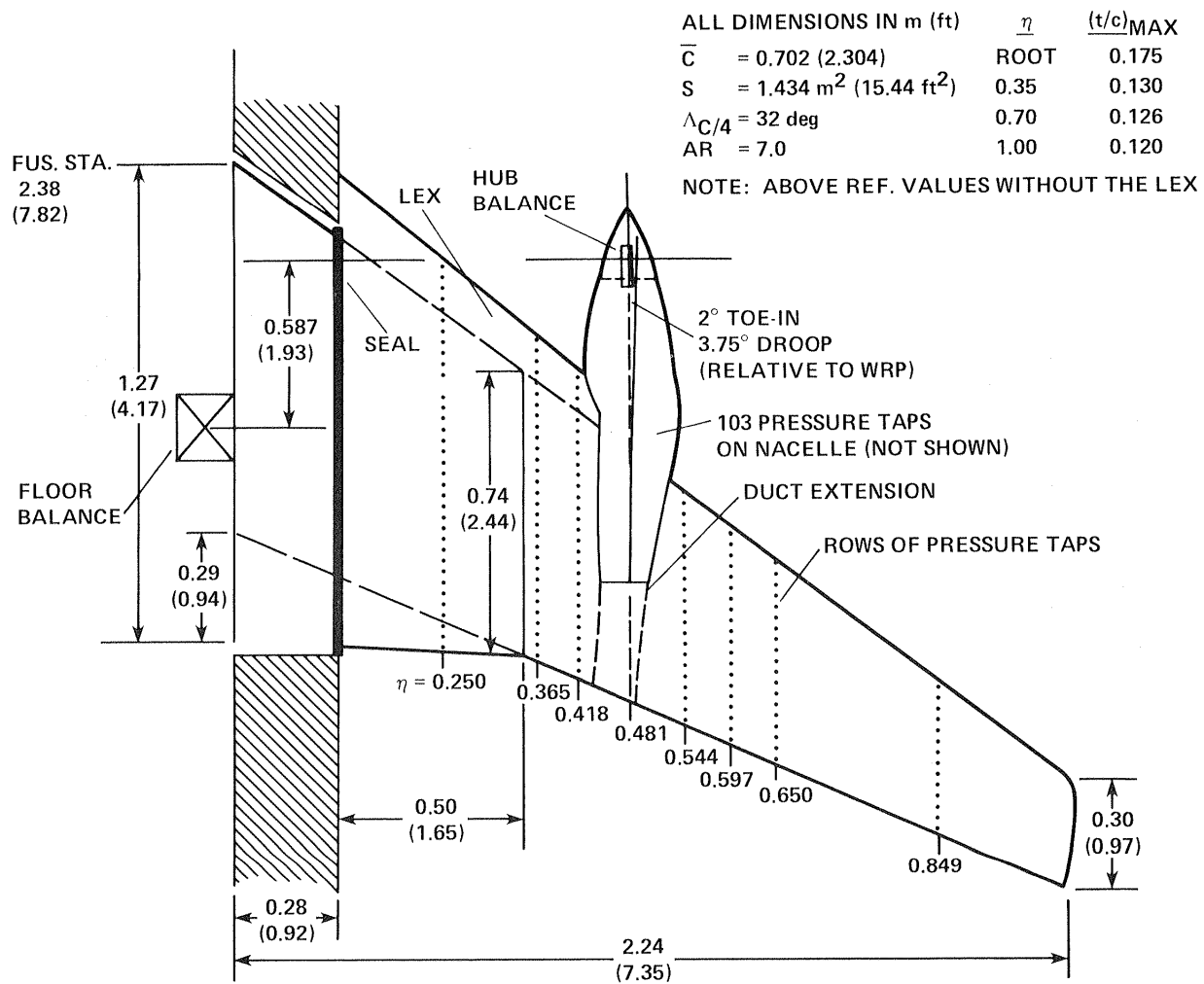
(d) Extended duct configuration, front view.

Figure 1.- Continued.



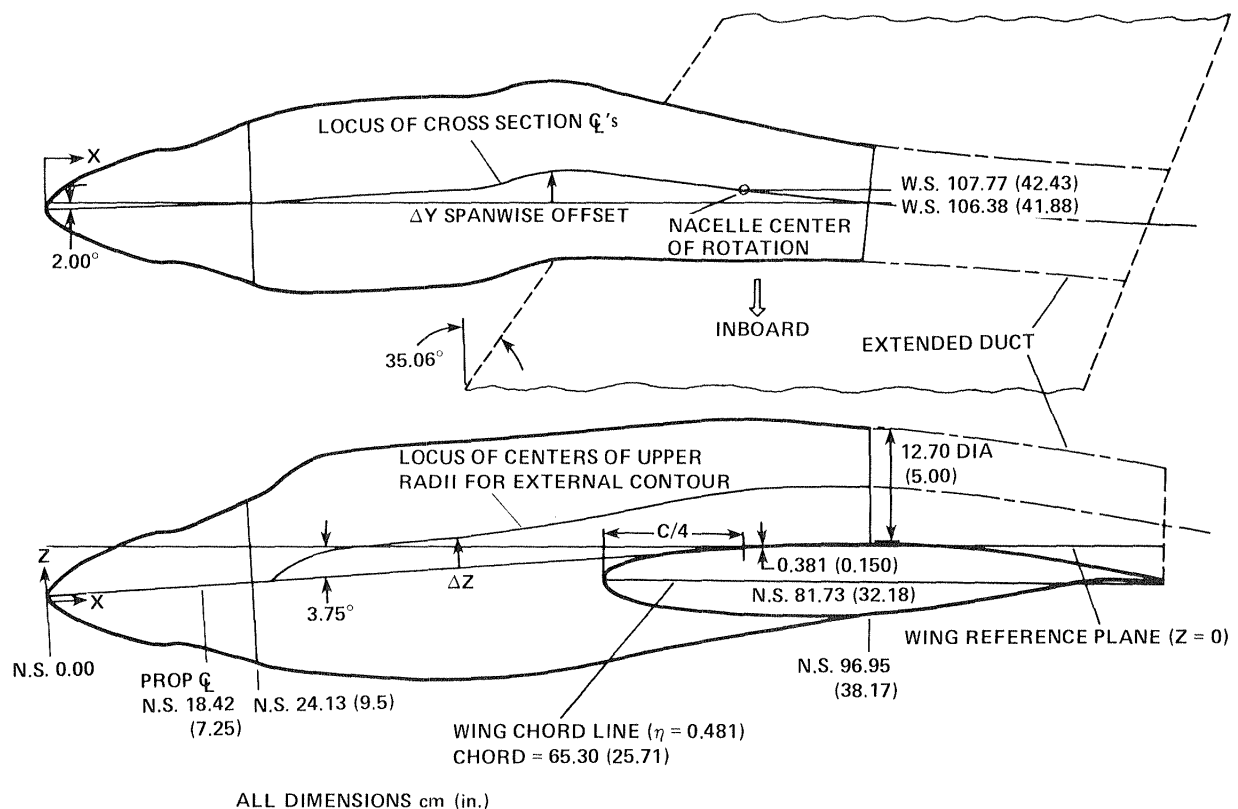
(e) Extended duct configuration, rear view.

Figure 1.- Concluded.



(a) Planform details.

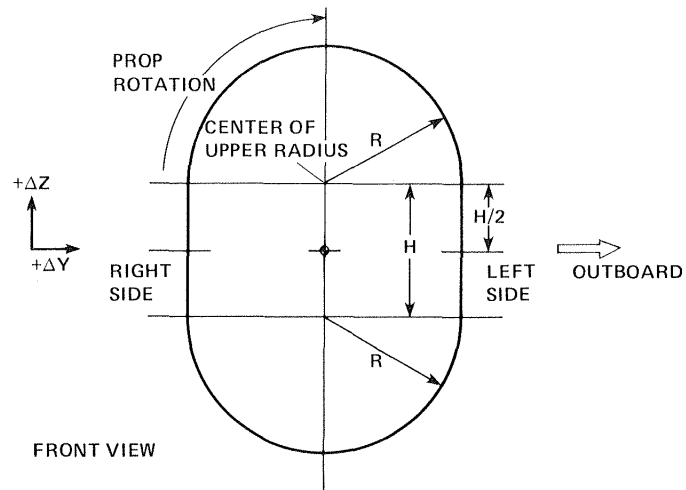
Figure 2.- Configuration geometry.



(b) Nacelle geometry.

Figure 2.- Continued.

NACELLE STATION		R		H		$\Delta Y$		$\Delta Z$	
cm	in.	cm	in.	cm	in.	cm	in.	cm	in.
24.13	9.5	9.474	3.730	0.0	0.0	0.0	0.0	0.0	0.0
25.40	10.0	9.908	3.901	0.038	0.015	0.058	0.023	0.0	0.0
26.67	10.5	10.244	4.033	0.356	0.140	0.122	0.048	0.277	0.109
27.94	11.0	10.505	4.136	1.148	0.452	0.185	0.073	1.021	0.402
29.21	11.5	10.696	4.211	1.936	0.762	0.254	0.100	1.750	0.689
30.48	12.0	10.831	4.264	2.578	1.015	0.328	0.129	2.327	0.916
31.75	12.5	10.927	4.302	3.099	1.220	0.409	0.161	2.756	1.085
33.02	13.0	10.993	4.328	3.546	1.396	0.500	0.197	3.084	1.214
34.29	13.5	11.036	4.345	3.838	1.511	0.597	0.235	3.236	1.274
35.56	14.0	11.064	4.356	4.072	1.603	0.696	0.274	3.309	1.303
36.83	14.5	11.080	4.362	4.288	1.688	0.793	0.312	3.355	1.321
39.37	15.5	11.097	4.369	4.686	1.845	0.975	0.384	3.419	1.346
41.91	16.5	11.097	4.369	5.024	1.978	1.135	0.447	3.482	1.371
44.45	17.5	11.077	4.361	5.314	2.092	1.262	0.497	3.543	1.395
46.99	18.5	11.034	4.344	5.572	2.194	1.344	0.529	3.602	1.418
49.53	19.5	10.965	4.317	5.662	2.229	1.471	0.579	3.686	1.451
52.07	20.5	10.866	4.278	6.053	2.383	1.897	0.747	3.828	1.507
54.61	21.5	10.739	4.228	6.286	2.475	2.634	1.037	4.003	1.576
57.15	22.5	10.584	4.167	6.518	2.566	3.297	1.298	4.189	1.649
59.69	23.5	10.401	4.095	6.749	2.657	3.663	1.442	4.404	1.734
62.23	24.5	10.190	4.012	6.980	2.748	3.719	1.464	4.676	1.841
64.77	25.5	9.952	3.918	7.214	2.840	3.487	1.373	4.991	1.965
67.31	26.5	9.685	3.813	7.445	2.931	3.142	1.237	5.332	2.099
69.85	27.5	9.390	3.697	7.676	3.022	2.819	1.110	5.669	2.232
72.39	28.5	9.116	3.589	7.907	3.113	2.517	0.991	5.982	2.355
74.93	29.5	8.852	3.485	8.138	3.204	2.217	0.873	6.281	2.473
77.47	30.5	8.590	3.382	8.369	3.295	1.910	0.752	6.571	2.587
80.01	31.5	8.331	3.280	8.600	3.386	1.603	0.631	6.807	2.680
82.55	32.5	8.075	3.179	8.738	3.440	1.308	0.515	6.942	2.733
85.09	33.5	7.823	3.080	8.766	3.451	1.047	0.412	6.965	2.742
87.63	34.5	7.569	2.980	8.697	3.424	0.803	0.316	6.894	2.714
90.17	35.5	7.315	2.880	8.565	3.372	0.549	0.216	6.759	2.661
92.71	36.5	7.060	2.780	8.410	3.311	0.295	0.116	6.599	2.598
95.25	37.5	6.807	2.680	8.240	3.244	0.038	0.015	6.426	2.530
96.95	38.17	6.640	2.614	8.126	3.199	-0.130	-0.051	6.309	2.484



(c) Nacelle cross-section geometry.

Figure 2.- Concluded.

SYMBOL	CONFIGURATION	MACH	ALPHA	EPR
—○—	W B OTWB L H2	.798	1.98	1.007
—□—	W B OTWB L H2	.793	1.99	1.266
—◇—	W B OTWB L H2	.798	1.98	1.963

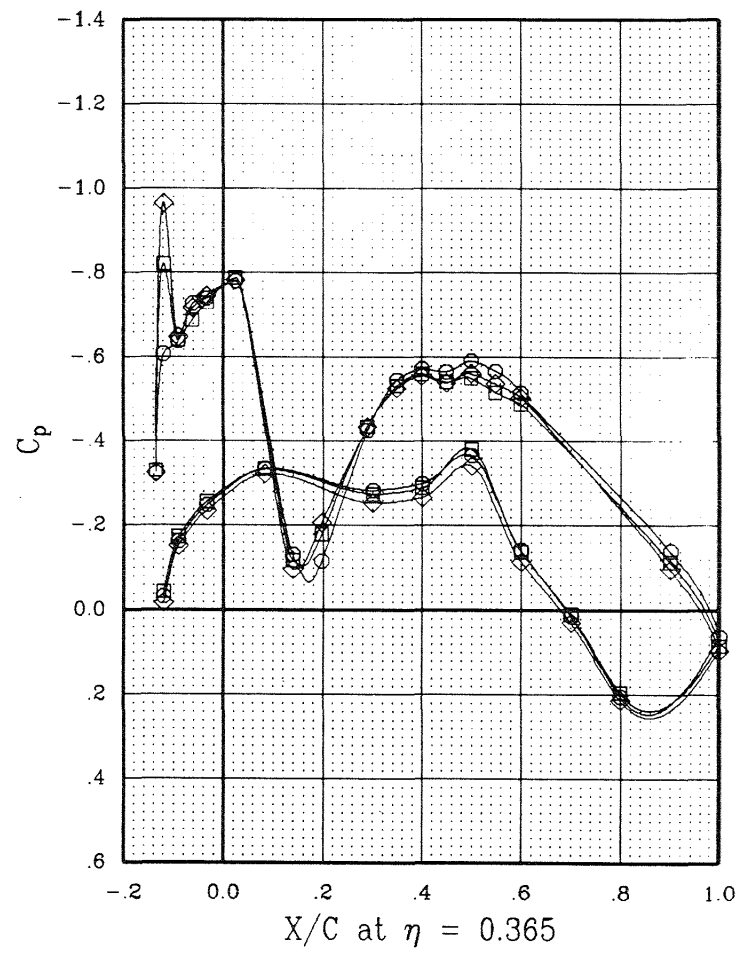
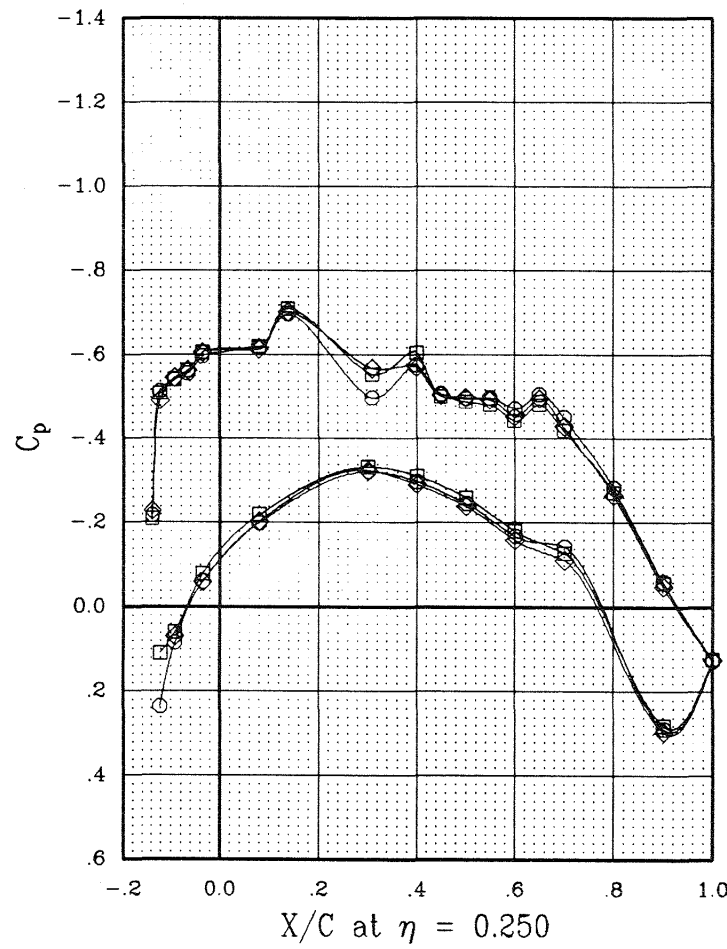
(a)  $\eta = 0.250$  and  $0.365$ .

Figure 3.- Jet effect on wing pressures; baseline configuration.

SYMBOL	CONFIGURATION	MACH	ALPHA	EPR
—○—	W B OTWB L H2	.798	1.98	1.007
—□—	W B OTWB L H2	.793	1.99	1.266
—◇—	W B OTWB L H2	.798	1.98	1.963

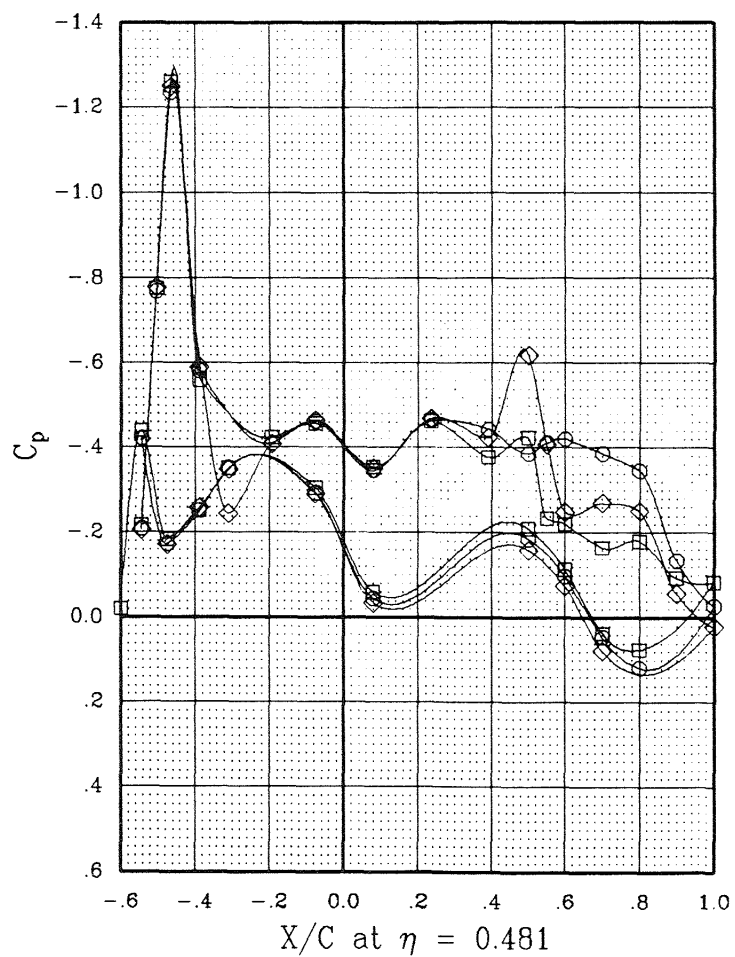
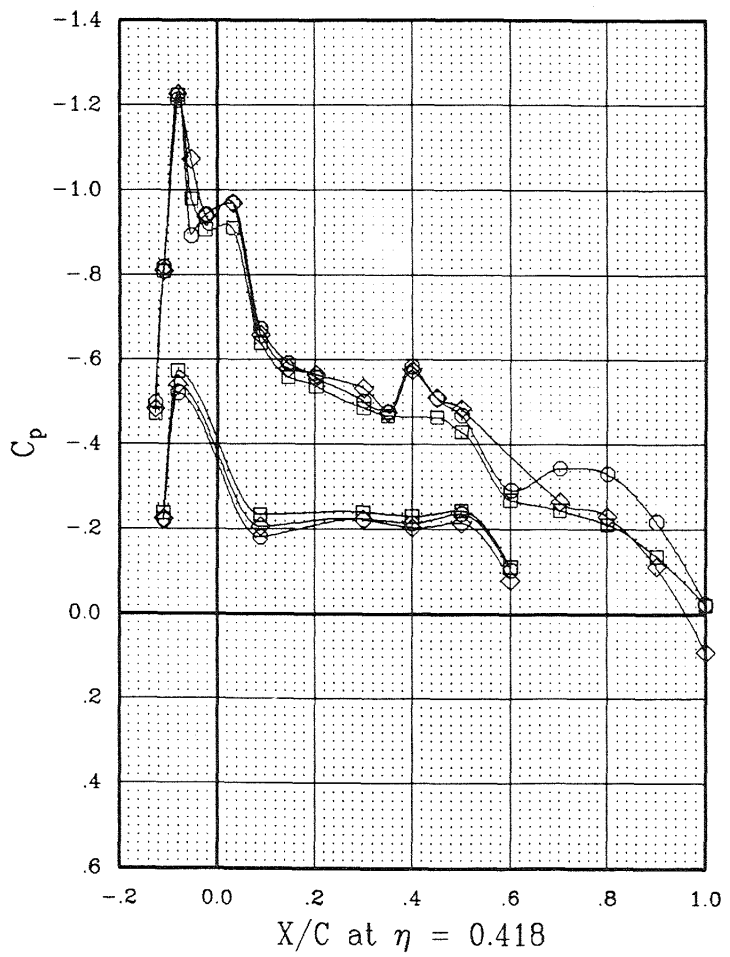
(b)  $\eta = 0.418$  and  $0.481$ .

Figure 3.- Continued.

SYMBOL	CONFIGURATION	MACH	ALPHA	EPR
○	W B OTWB L H2	.798	1.98	1.007
□	W B OTWB L H2	.793	1.99	1.266
◇	W B OTWB L H2	.798	1.98	1.963

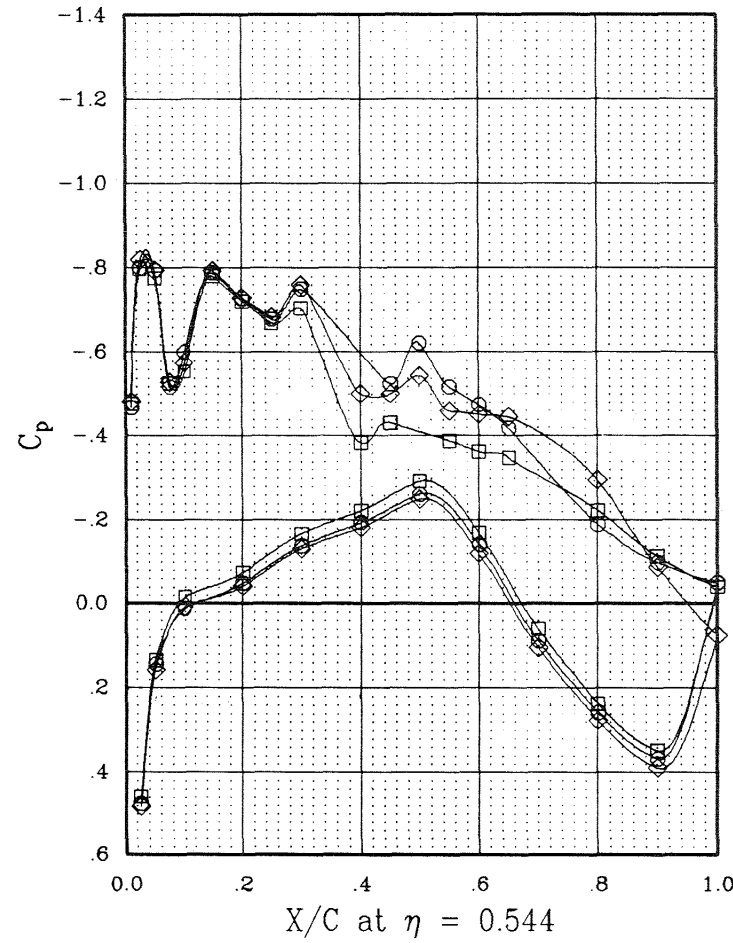
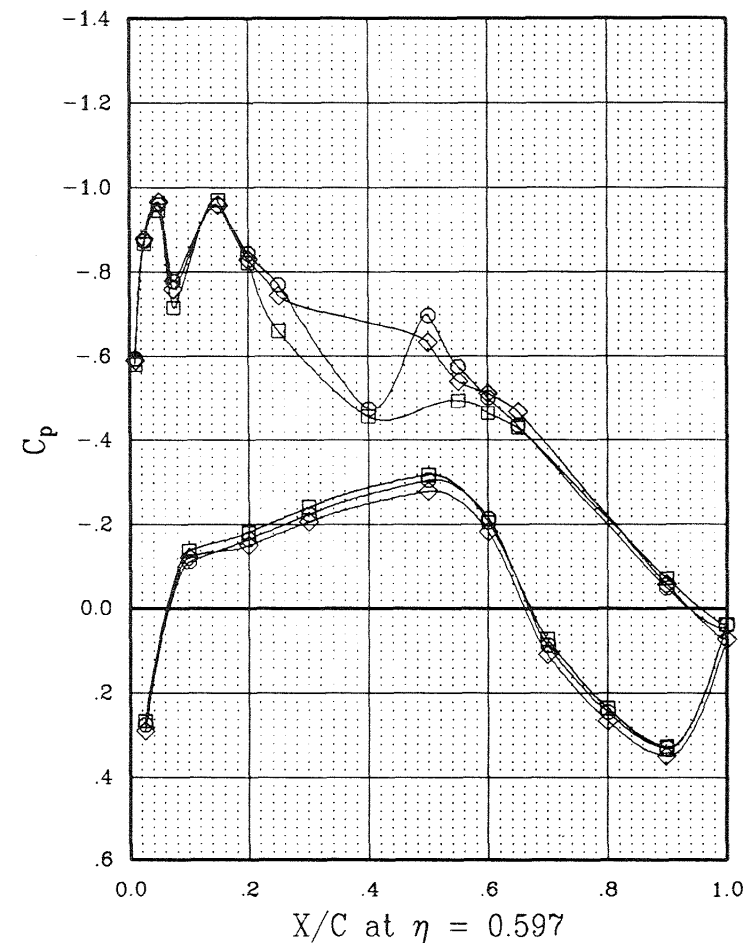
(c)  $\eta = 0.544$  and  $0.597$ .

Figure 3.- Continued.

SYMBOL	CONFIGURATION	MACH	ALPHA	EPR
—○—	W B OTWB L H2	.798	1.98	1.007
—□—	W B OTWB L H2	.793	1.99	1.266
—◇—	W B OTWB L H2	.798	1.98	1.963

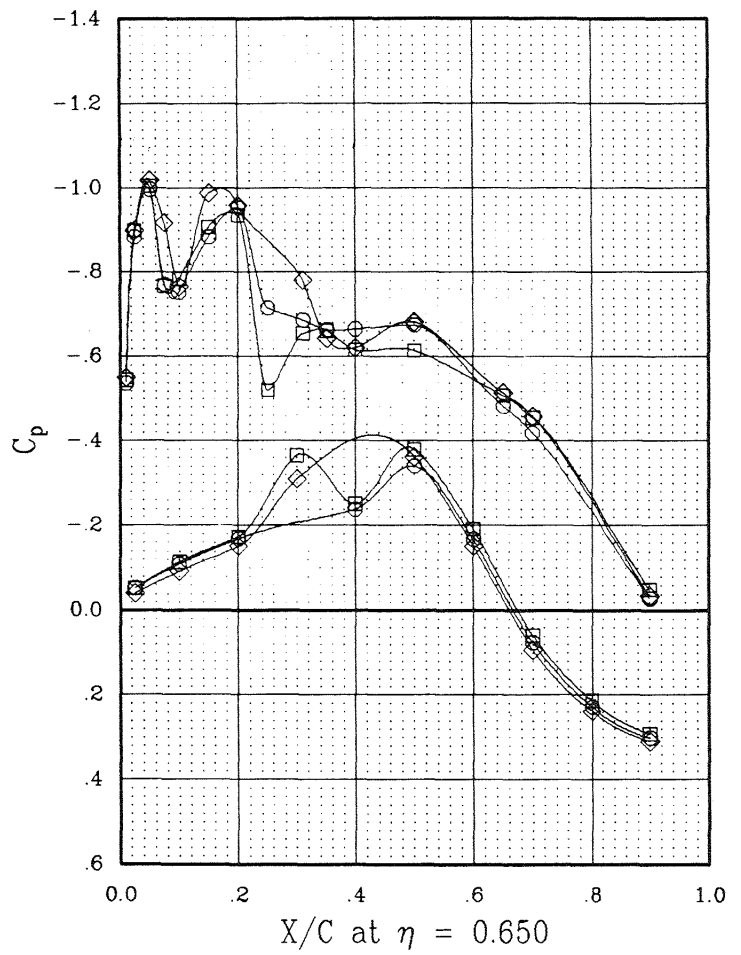
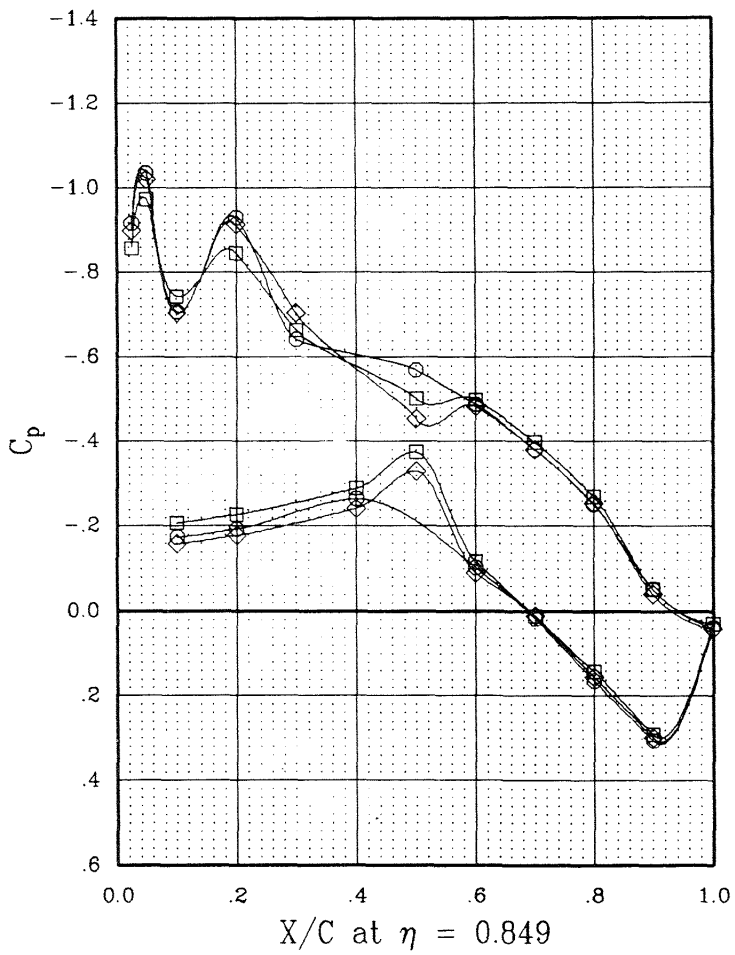
(d)  $\eta = 0.650$  and  $0.849$ .

Figure 3.- Concluded.

SYMBOL	CONFIGURATION	MACH	ALPHA	EPR
—○—	W B OTWB L H2 E	.791	1.97	1.000
—□—	W B OTWB L H2 E	.803	1.97	1.195
—◇—	W B OTWB L H2 E	.799	1.96	1.898

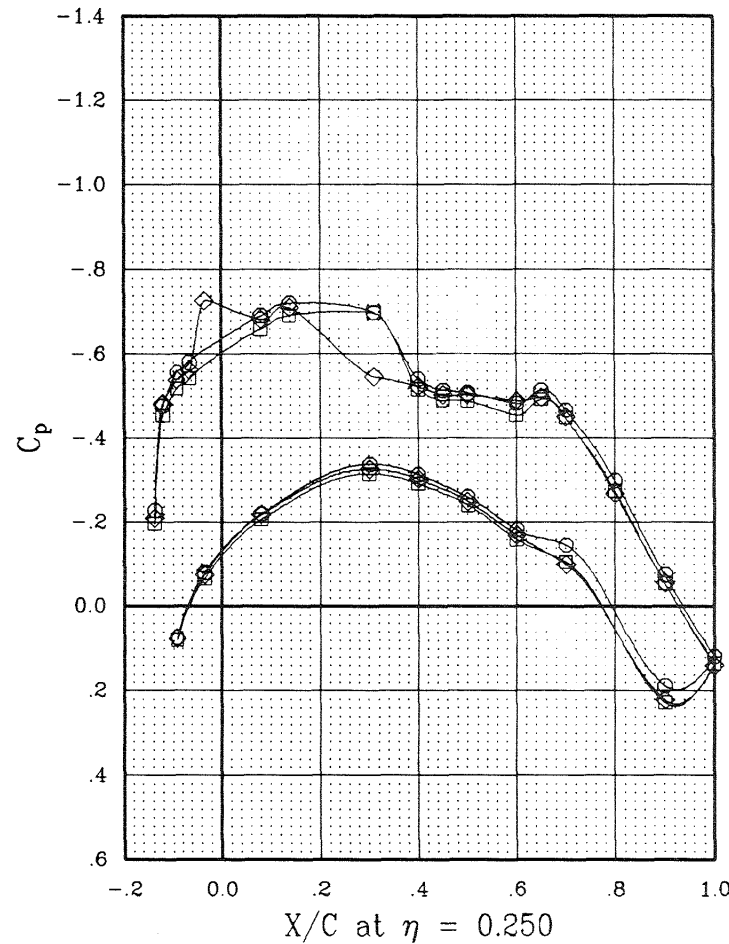
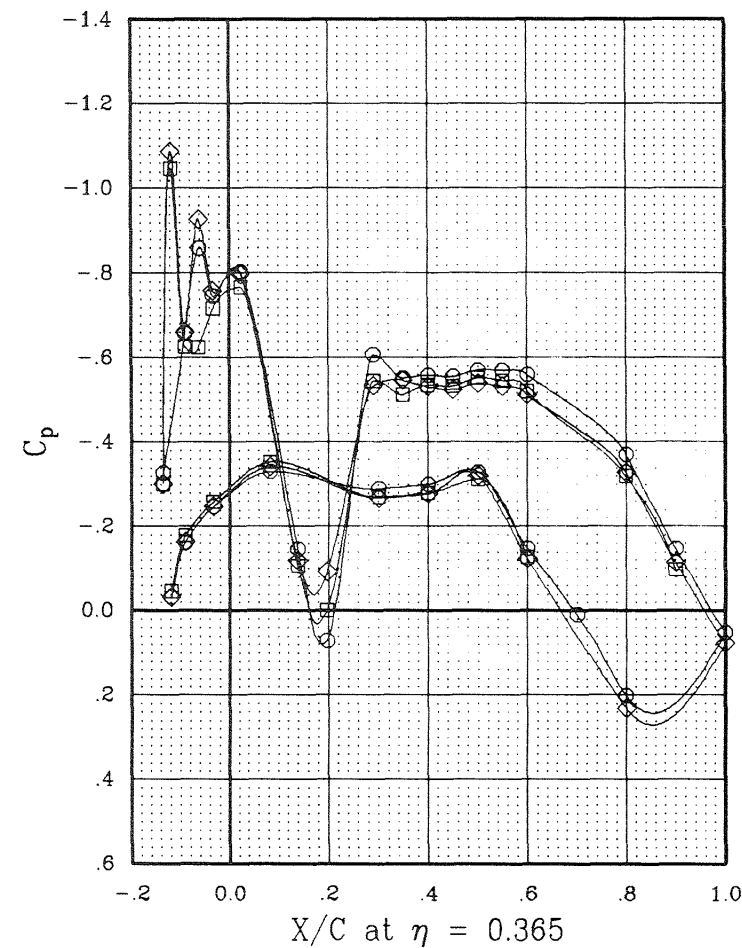
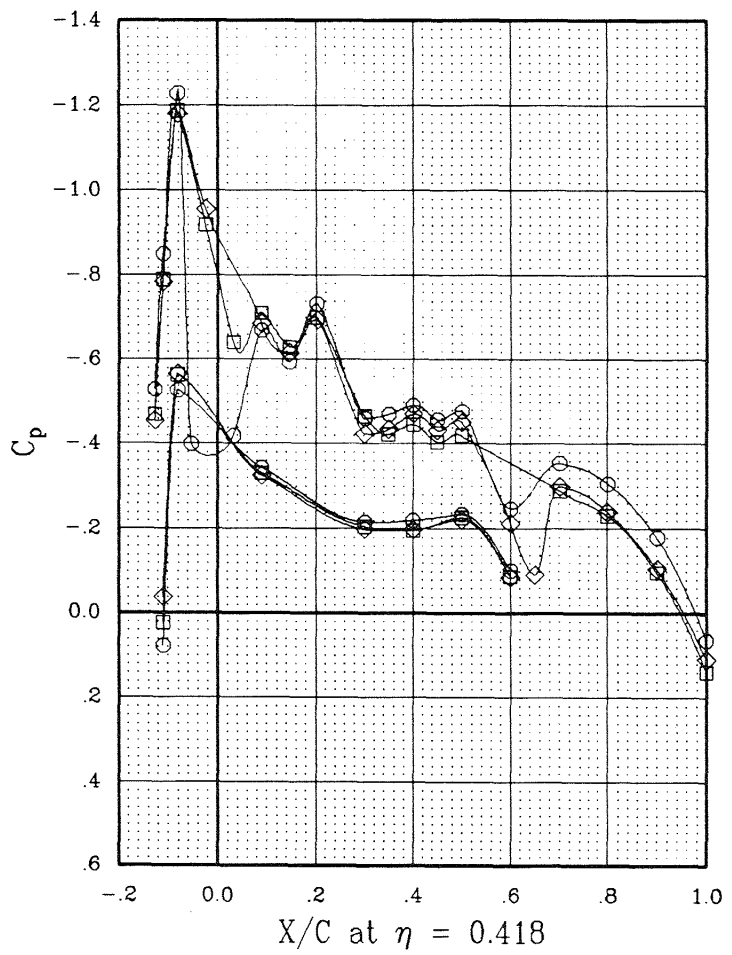
(a)  $\eta = 0.250$  and  $0.365$ .

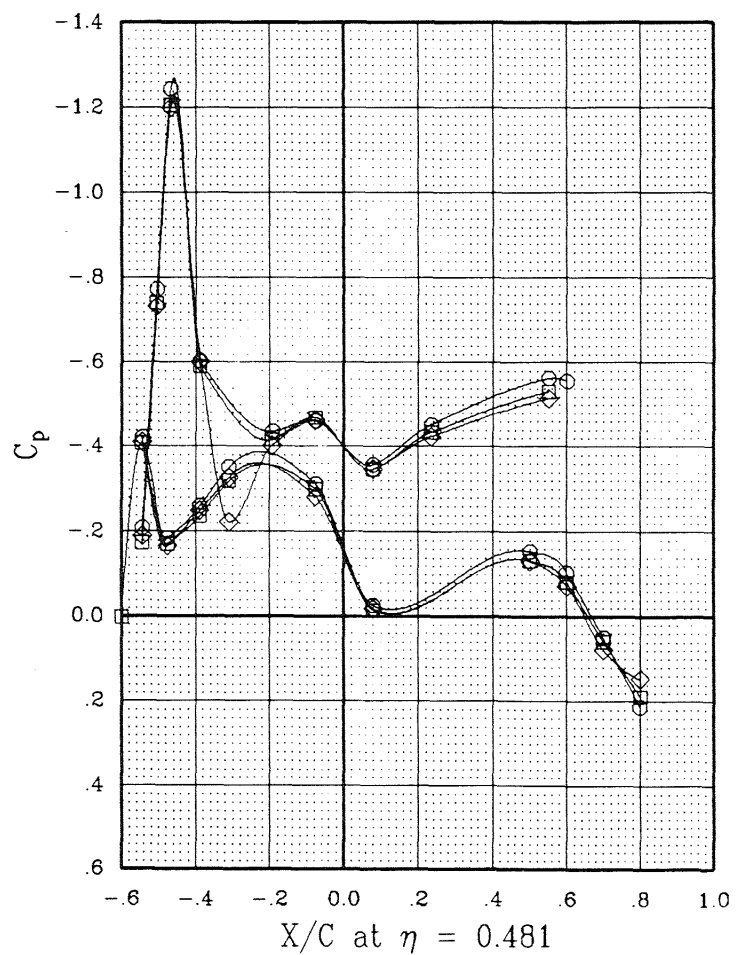
Figure 4.- Jet effect on wing pressures; extended duct configuration.

SYMBOL	CONFIGURATION	MACH	ALPHA	EPR
—○—	W B OTWB L H2 E	.791	1.97	1.000
—□—	W B OTWB L H2 E	.803	1.97	1.195
—◇—	W B OTWB L H2 E	.799	1.96	1.898

30



$X/C$  at  $\eta = 0.418$

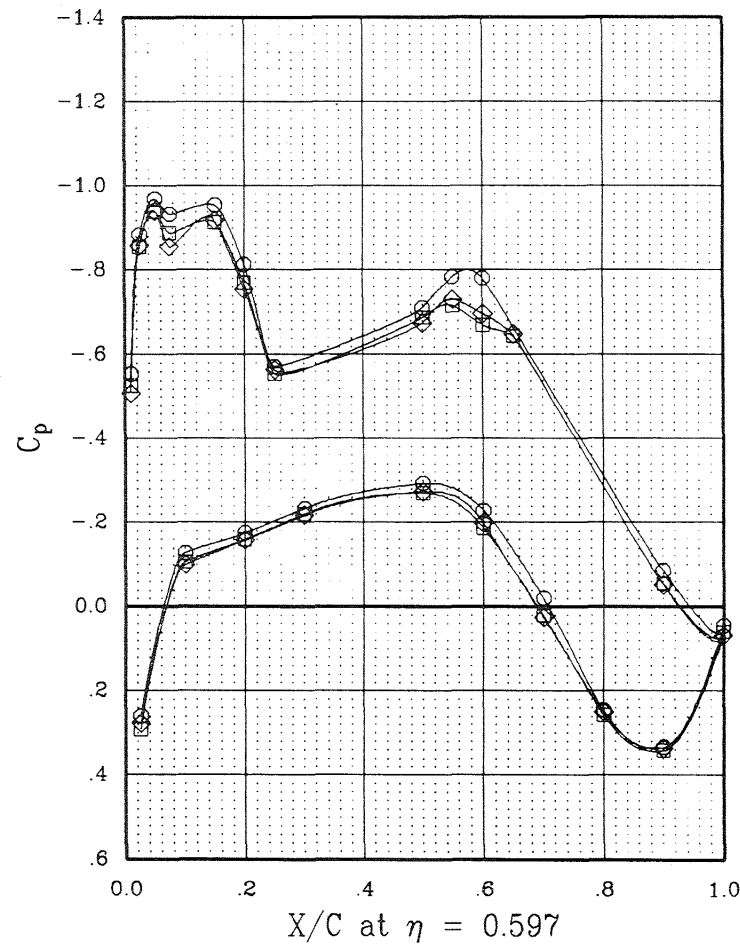
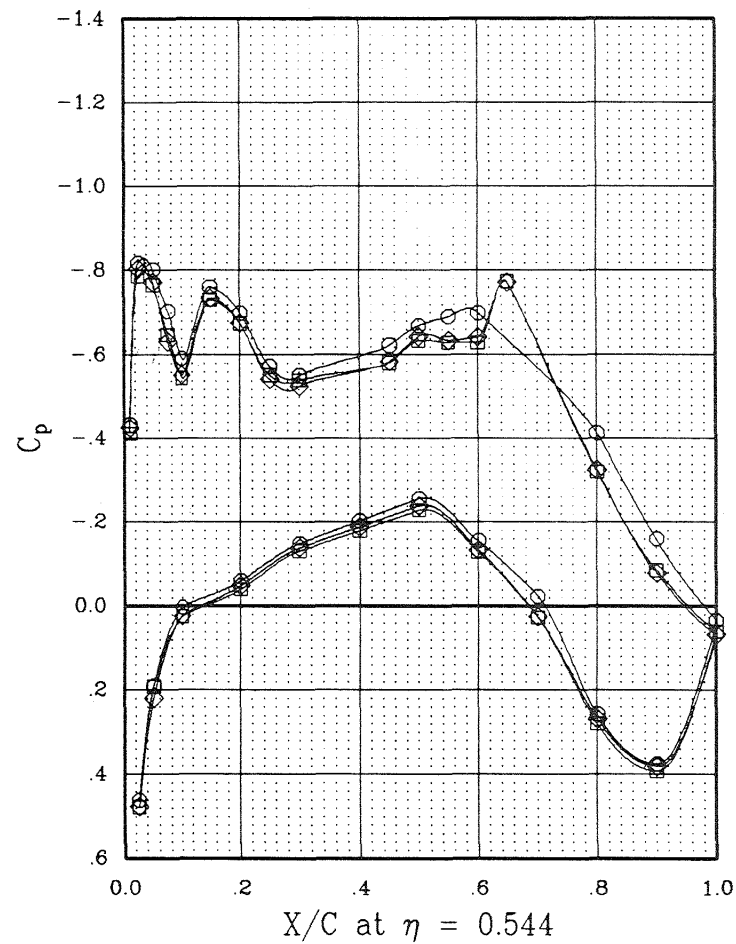


(b)  $\eta = 0.418$  and  $0.481$ .

Figure 4-- Continued.

SYMBOL	CONFIGURATION	MACH	ALPHA	EPR
—○—	W B OTWB L H2 E	.791	1.97	1.000
—□—	W B OTWB L H2 E	.803	1.97	1.195
—◇—	W B OTWB L H2 E	.799	1.96	1.898

31



(c)  $\eta = 0.544$  and  $0.597$ .

Figure 4.- Continued.

SYMBOL	CONFIGURATION	MACH	ALPHA	EPR
—○—	W B OTWB L H2 E	.791	1.97	1.000
—□—	W B OTWB L H2 E	.803	1.97	1.195
—◇—	W B OTWB L H2 E	.799	1.96	1.898

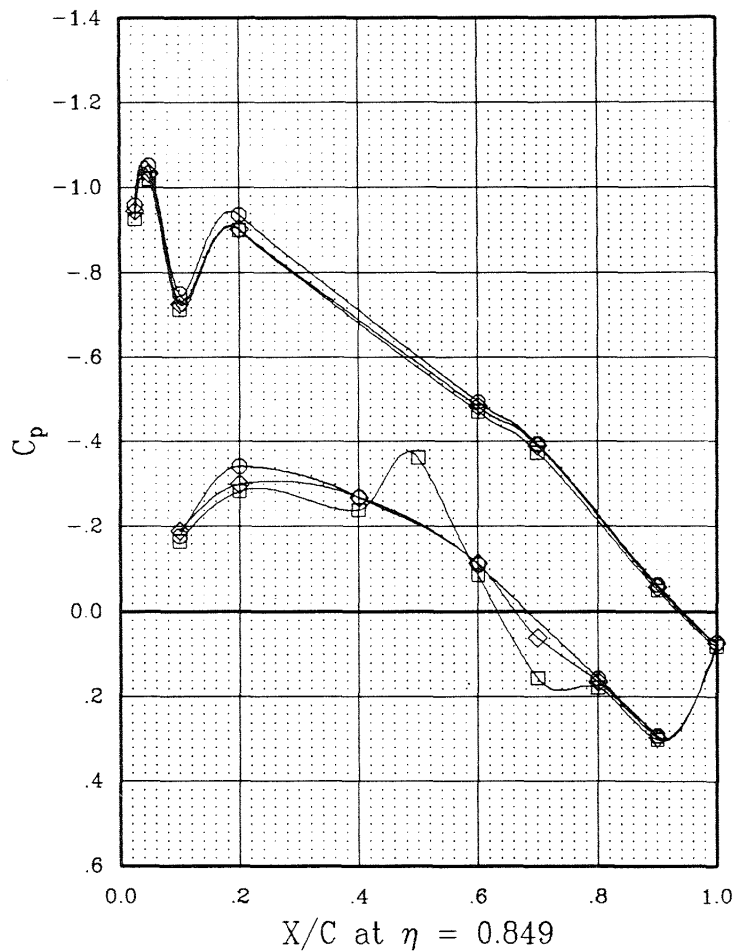
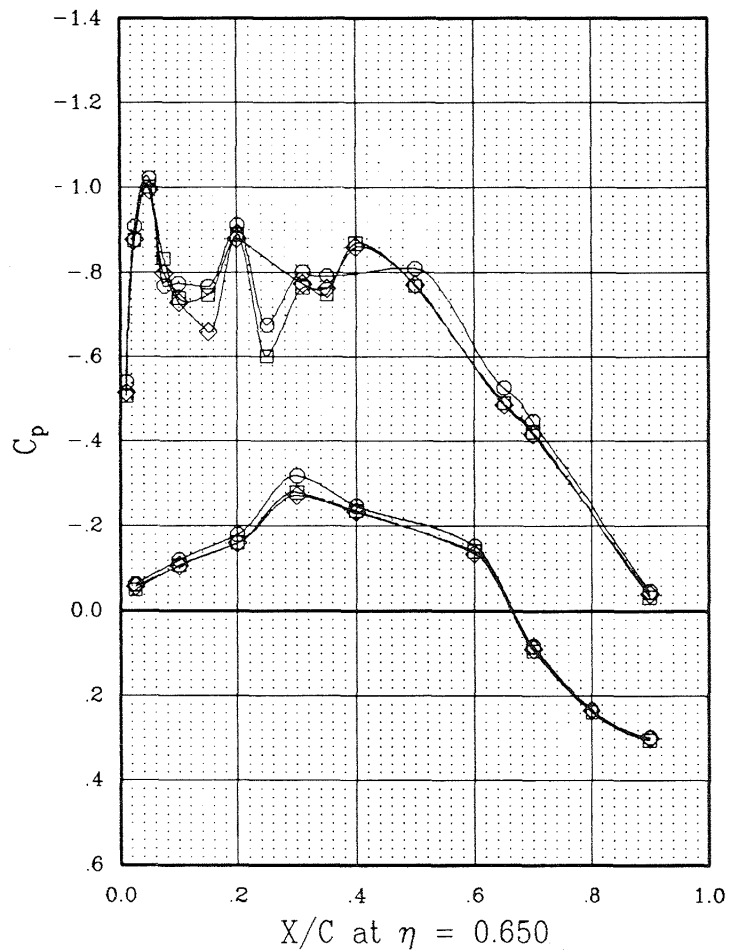
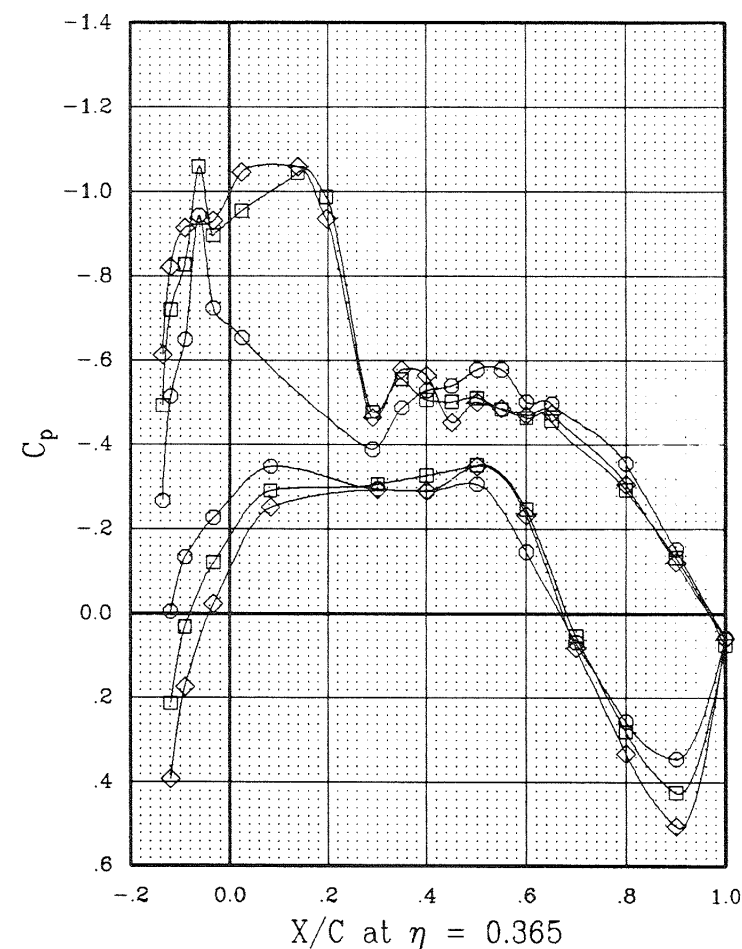
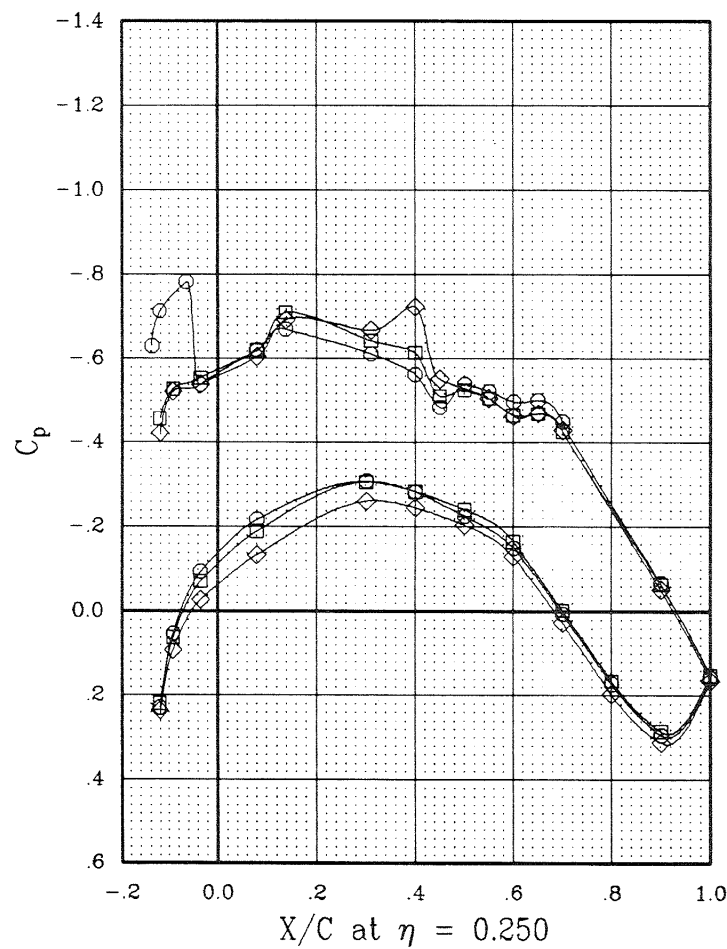
(d)  $\eta = 0.650$  and  $0.849$ .

Figure 4.- Concluded.

SYMBOL	CONFIGURATION	MACH	ALPHA	BETAP	EPR	RPM
—○—	W B OTW L H2 P2	.798	1.93	56.4	1.001	6629
—□—	W B OTW L H2 P2	.788	1.95	56.4	1.185	7562
—◇—	W B OTW L H2 P2	.796	1.94	56.4	1.908	8347

33

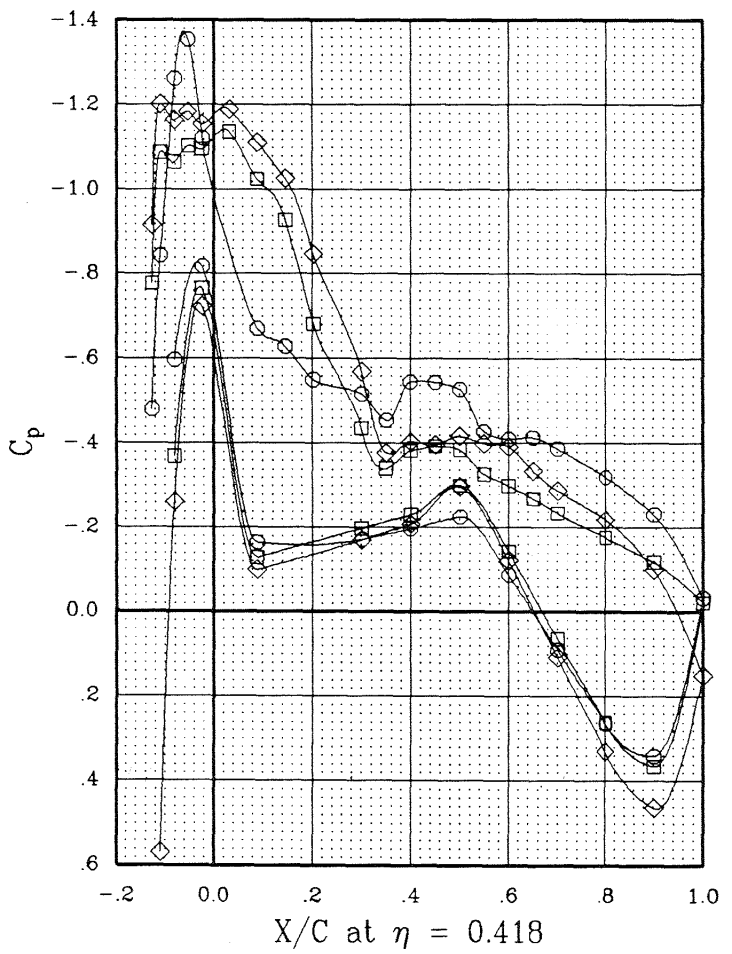


(a)  $\eta = 0.250$  and  $0.365$ .

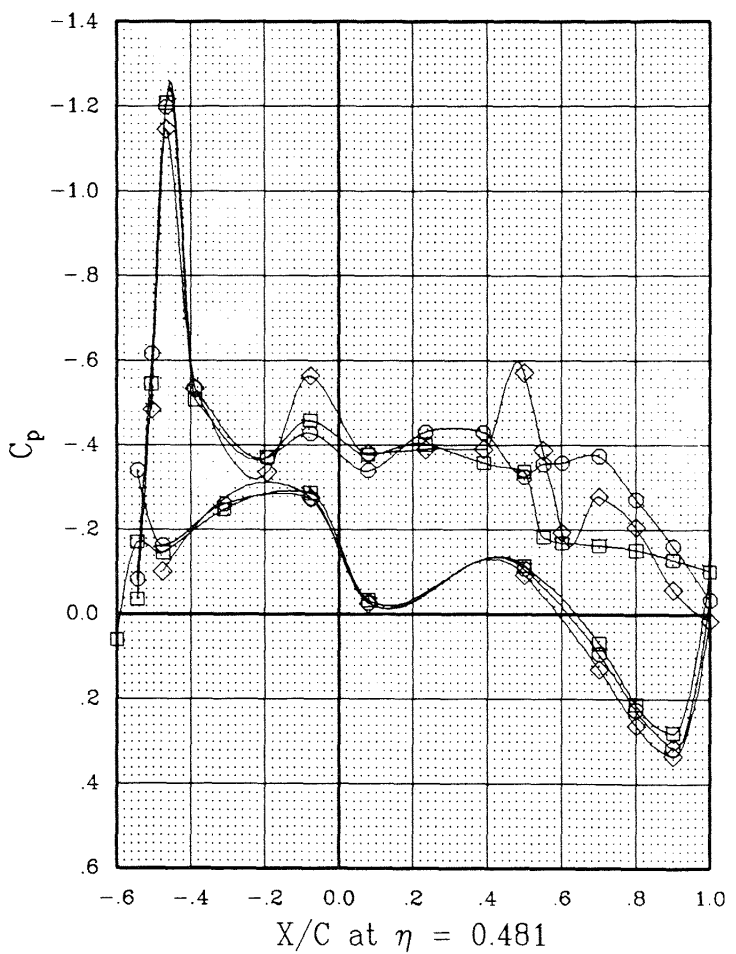
Figure 5.- Effect of propeller speed on wing pressures; baseline.

SYMBOL	CONFIGURATION	MACH	ALPHA	BETAP	EPR	RPM
—○—	W B OTW L H2 P2	.798	1.93	56.4	1.001	6629
—□—	W B OTW L H2 P2	.788	1.95	56.4	1.185	7562
—◇—	W B OTW L H2 P2	.798	1.94	56.4	1.908	8347

34



X/C at  $\eta = 0.418$

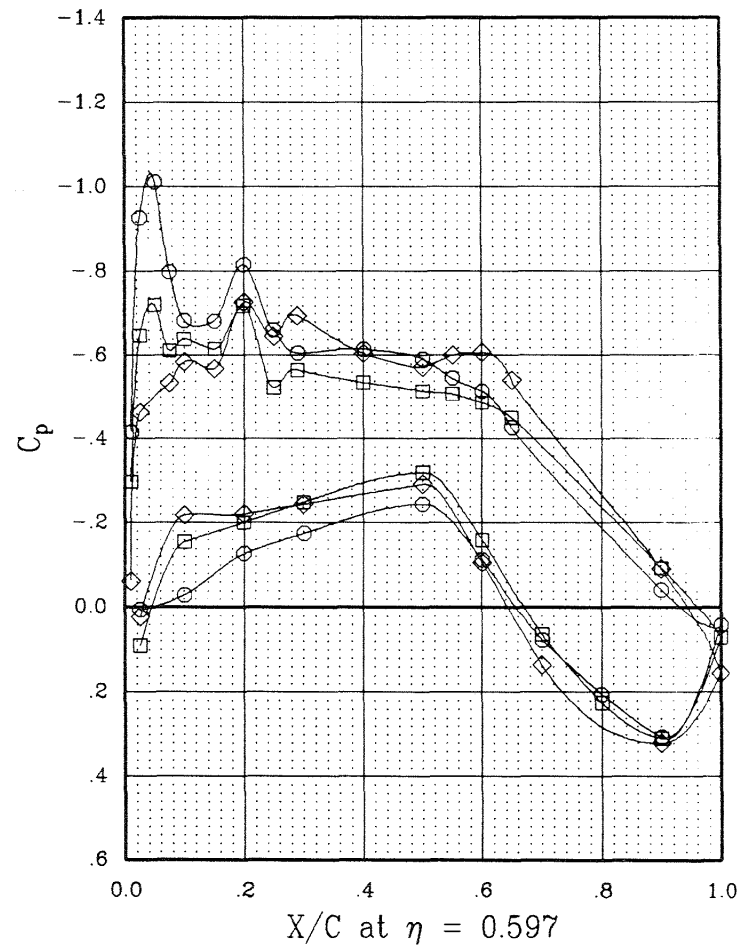
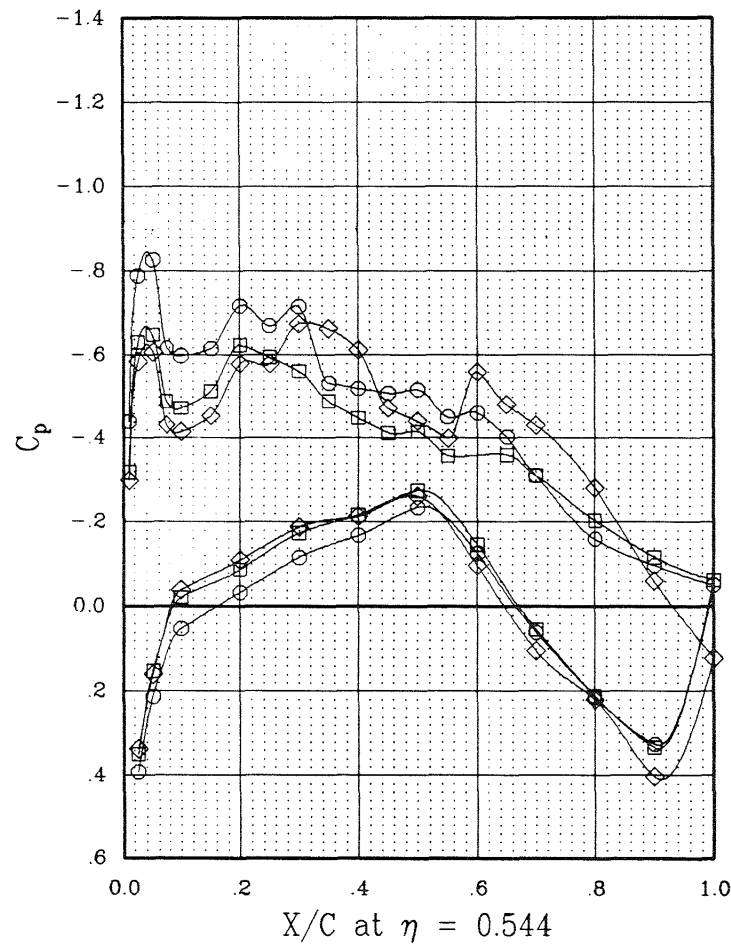


(b)  $\eta = 0.418$  and  $0.481$ .

Figure 5.- Continued.

SYMBOL	CONFIGURATION	MACH	ALPHA	BETAP	EPR	RPM
—○—	W B OTW L H2 P2	.798	1.93	56.4	1.001	6629
—□—	W B OTW L H2 P2	.798	1.95	56.4	1.185	7562
—◇—	W B OTW L H2 P2	.796	1.94	56.4	1.908	8347

35



(c)  $\eta = 0.544$  and  $0.597$ .

Figure 5.- Continued.

SYMBOL	CONFIGURATION	MACH	ALPHA	BETAP	EPR	RPM
—○—	W B OTW L H2 P2	.798	1.93	56.4	1.001	6629
—□—	W B OTW L H2 P2	.788	1.95	56.4	1.185	7562
—◇—	W B OTW L H2 P2	.796	1.94	56.4	1.908	8347

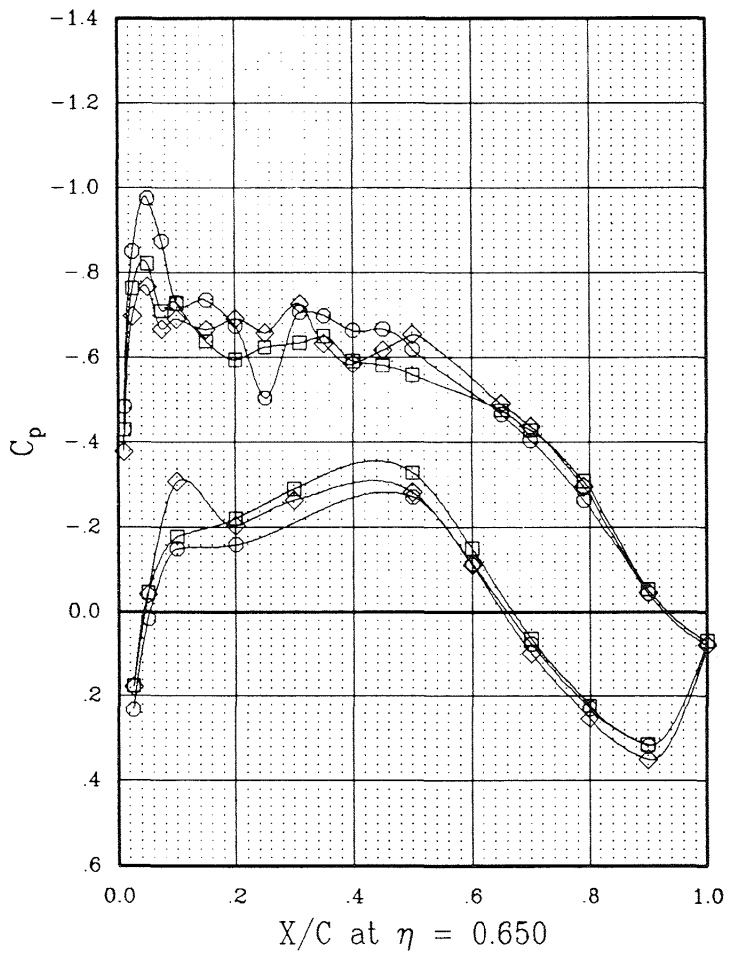
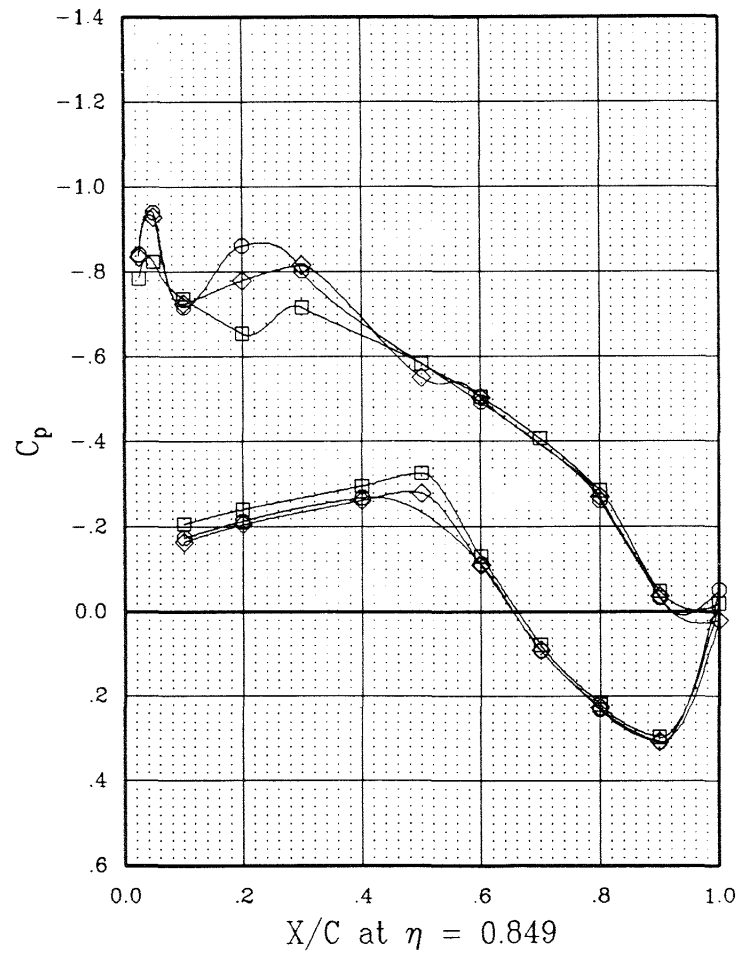
(d)  $\eta = 0.650$  and  $0.849$ .

Figure 5.- Concluded.

SYMBOL	CONFIGURATION	MACH	ALPHA	BETAP	EPR	RPM
—○—	W B OTW L H2 P2 E	.790	1.94	56.4	1.040	6661
—□—	W B OTW L H2 P2 E	.794	1.94	56.4	1.253	8001
—◇—	W B OTW L H2 P2 E	.798	1.94	56.4	1.582	8427

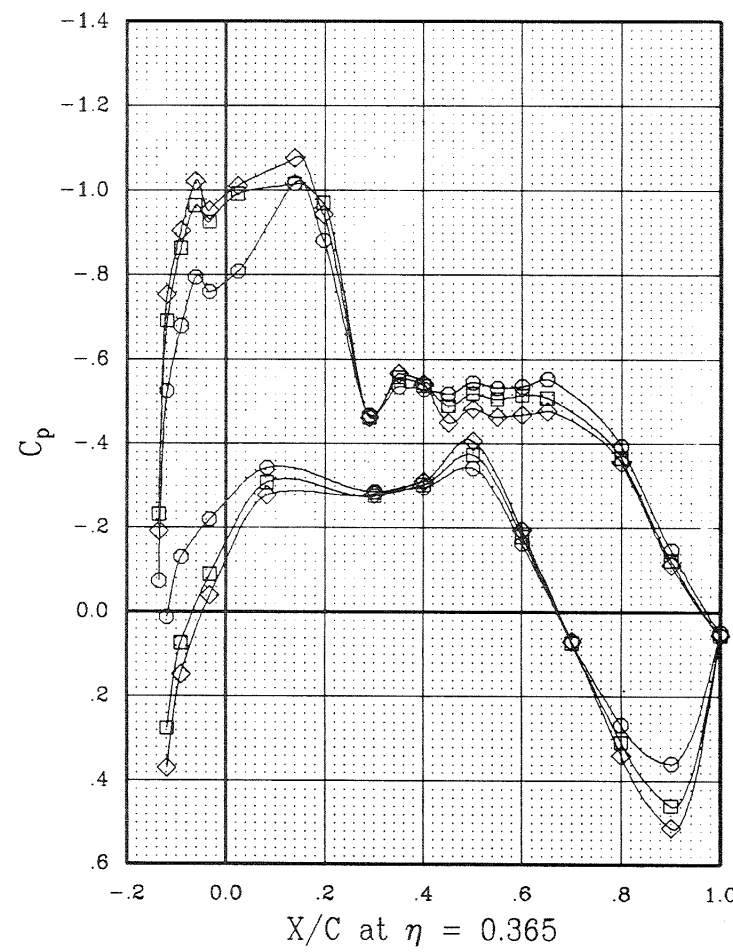
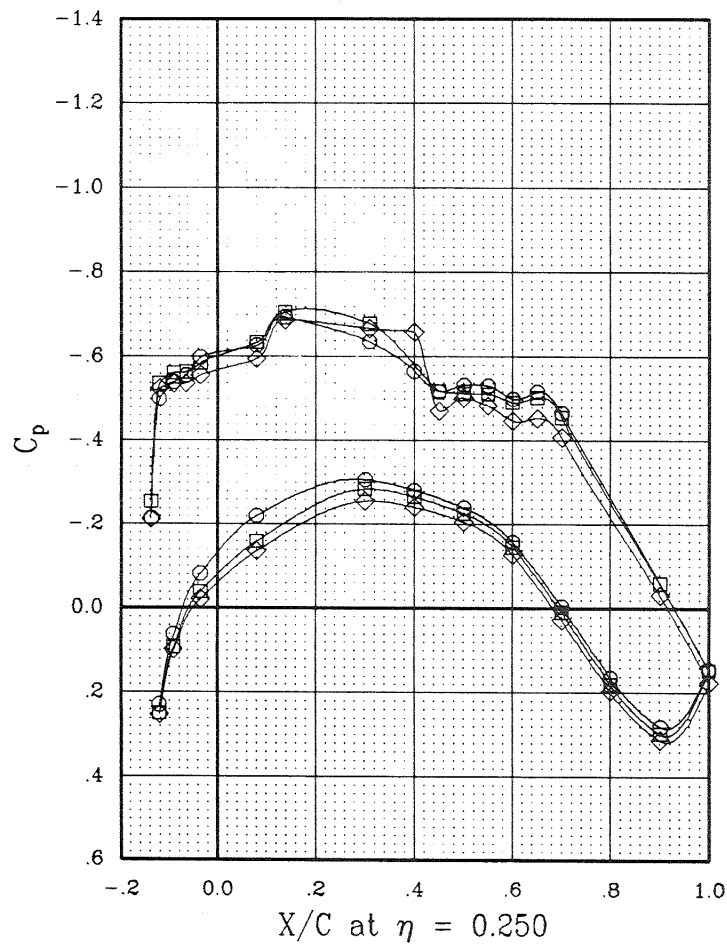
(a)  $\eta = 0.250$  and  $0.365$ .

Figure 6.- Effect of propeller speed on wing pressures; extended duct.

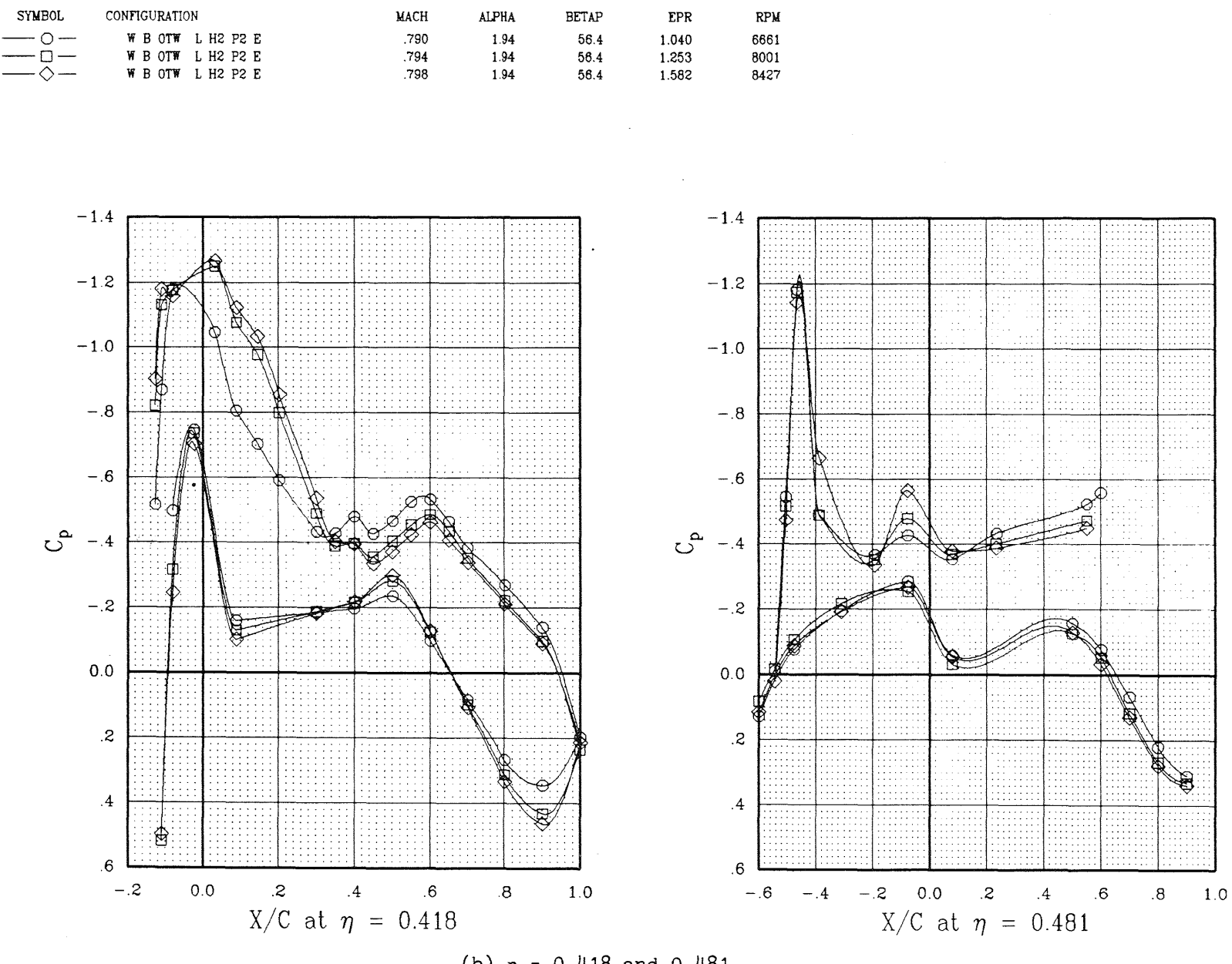
(b)  $\eta = 0.418$  and  $0.481$ .

Figure 6.- Continued.

SYMBOL	CONFIGURATION	MACH	ALPHA	BETAP	EPR	RPM
—○—	W B OTW L H2 P2 E	.790	1.94	56.4	1.040	6661
—□—	W B OTW L H2 P2 E	.794	1.94	56.4	1.253	8001
—◇—	W B OTW L H2 P2 E	.798	1.94	56.4	1.582	8427

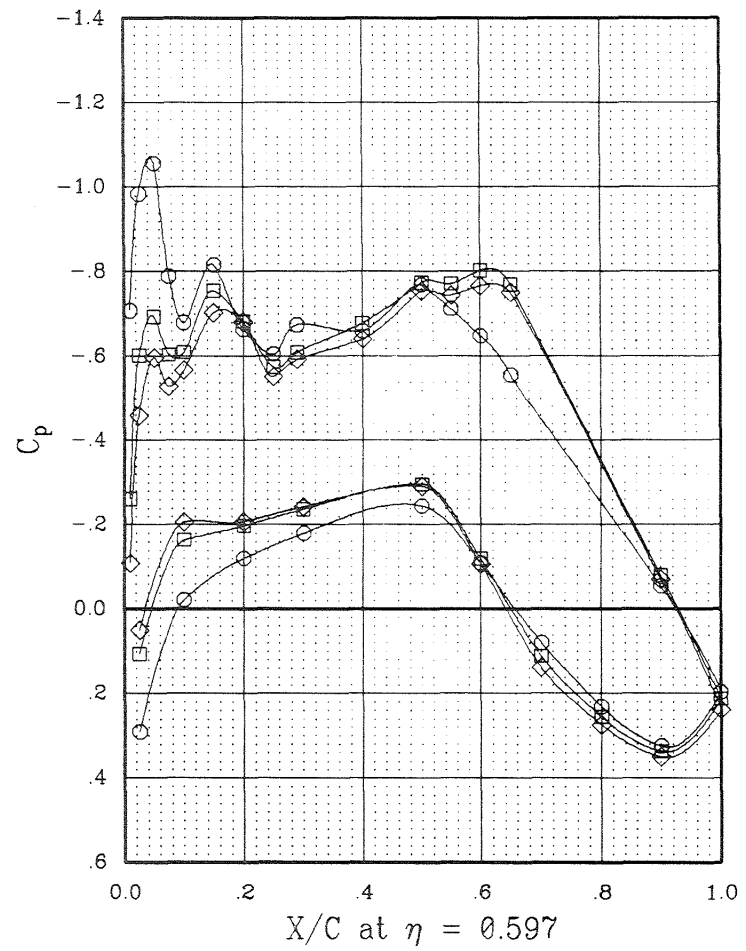
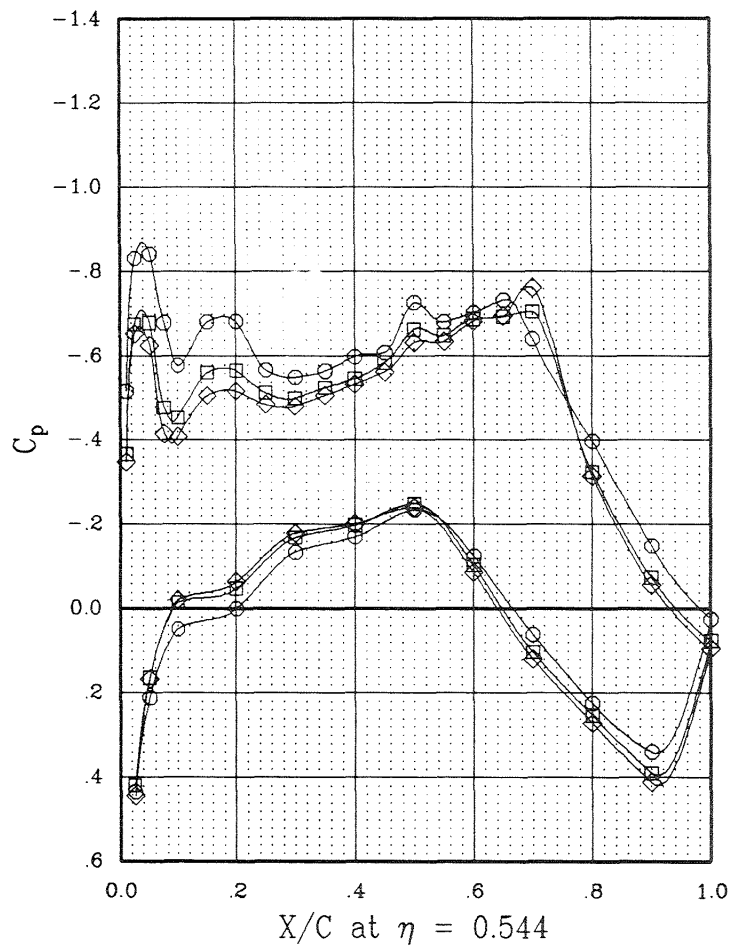
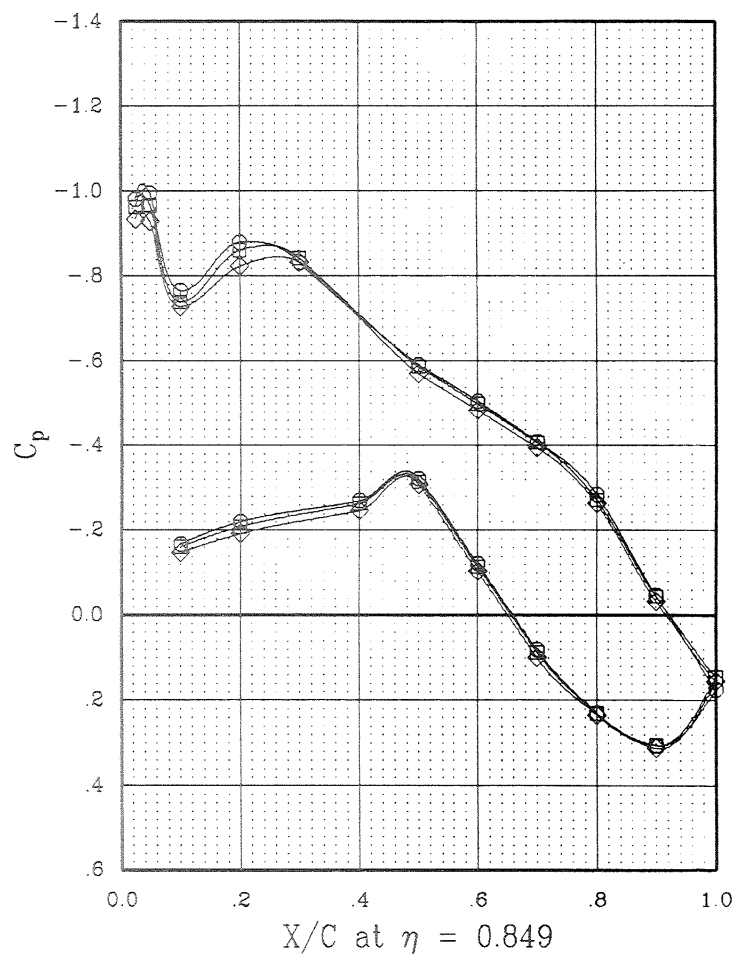
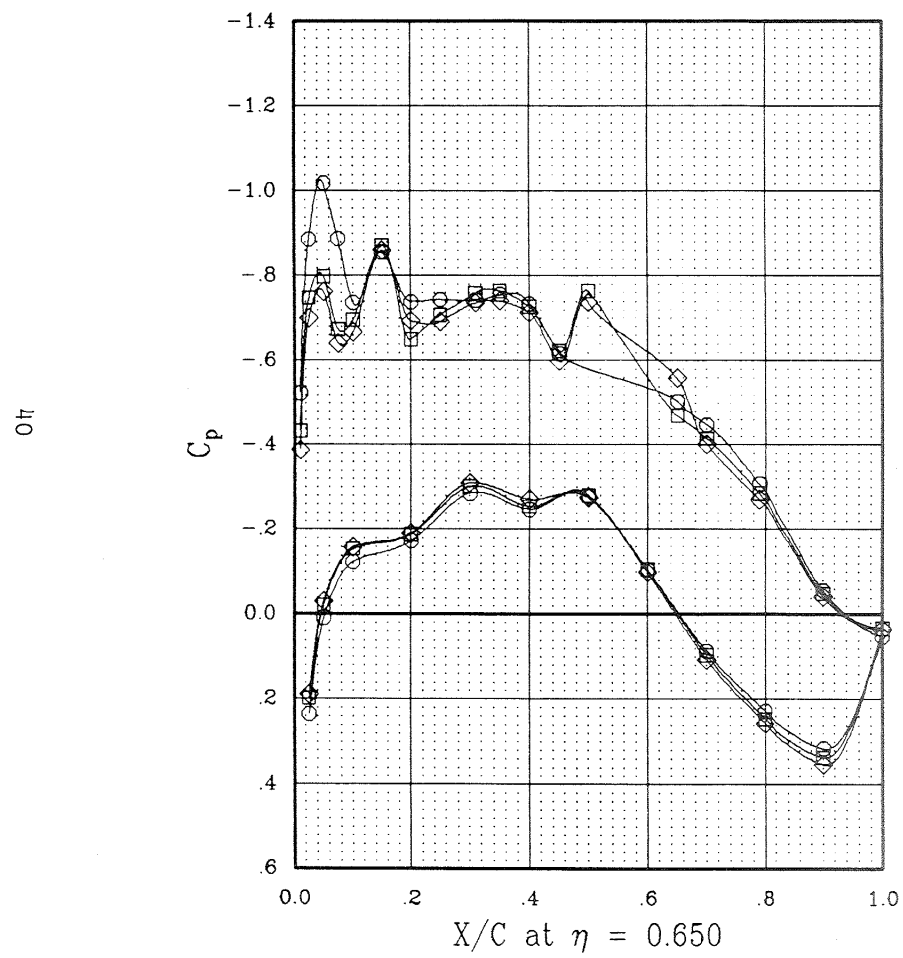
(c)  $\eta = 0.544$  and  $0.597$ .

Figure 6.- Continued.

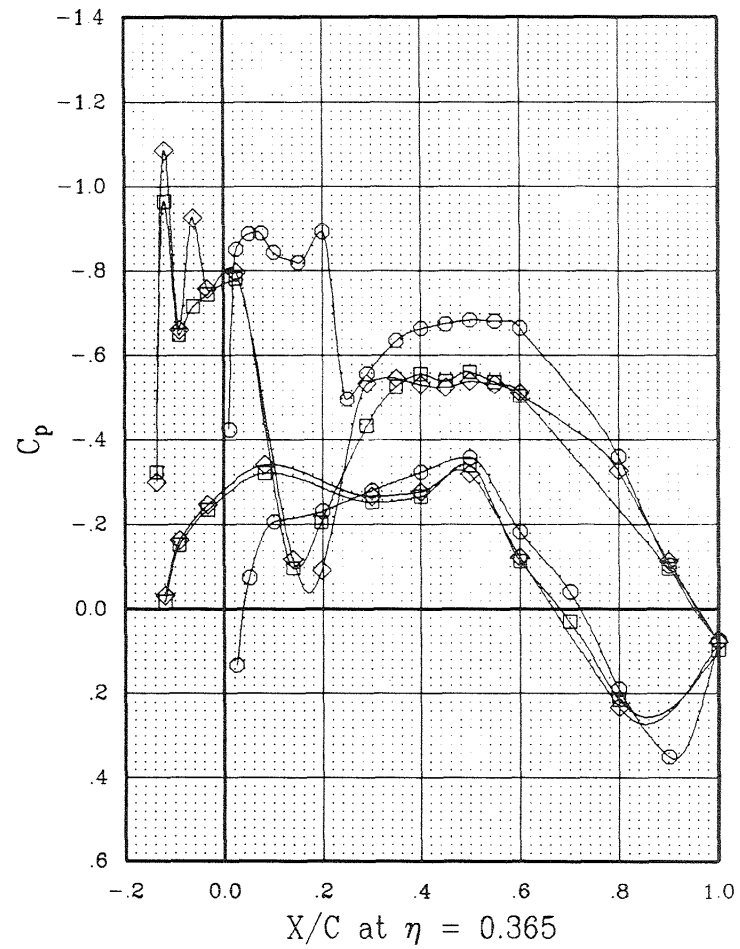
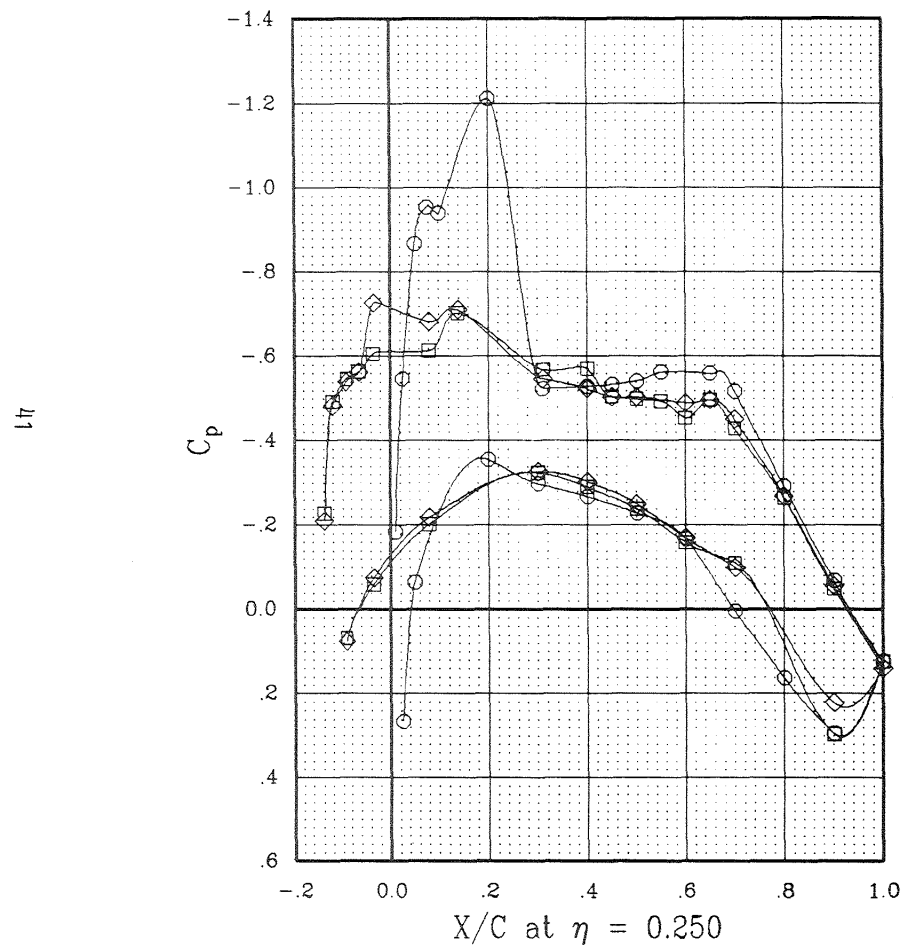
SYMBOL	CONFIGURATION	MACH	ALPHA	BETAP	EPR	RPM
—○—	W B OTW L H2 P2 E	.790	1.94	56.4	1.040	6661
—□—	W B OTW L H2 P2 E	.794	1.94	56.4	1.253	8001
—◇—	W B OTW L H2 P2 E	.798	1.94	56.4	1.582	8427



(d)  $\eta = 0.650$  and  $0.849$ .

Figure 6.- Concluded.

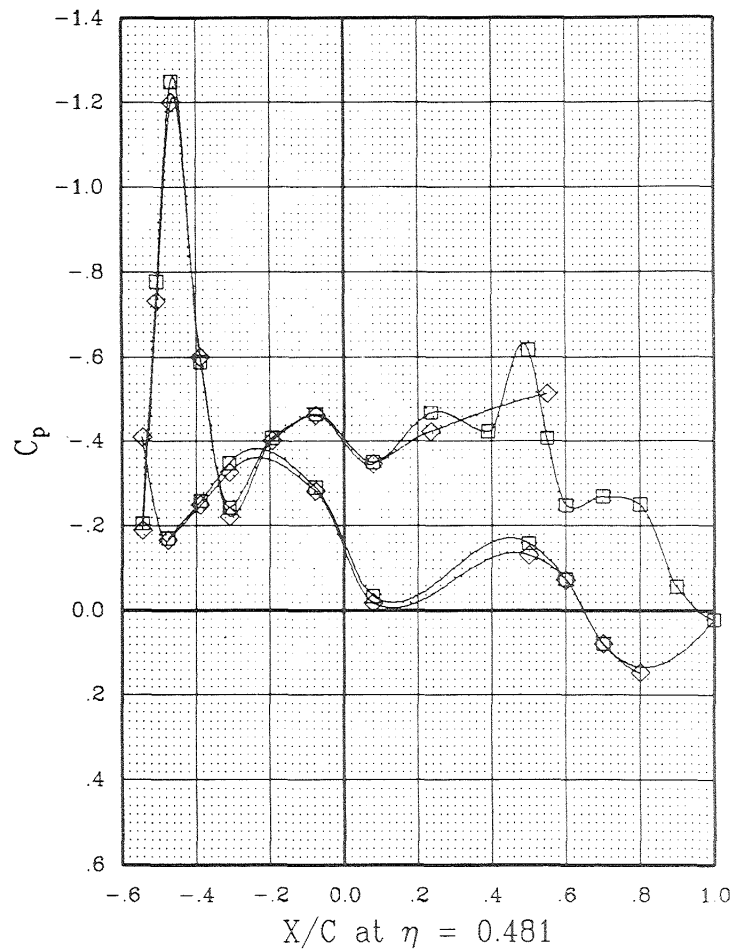
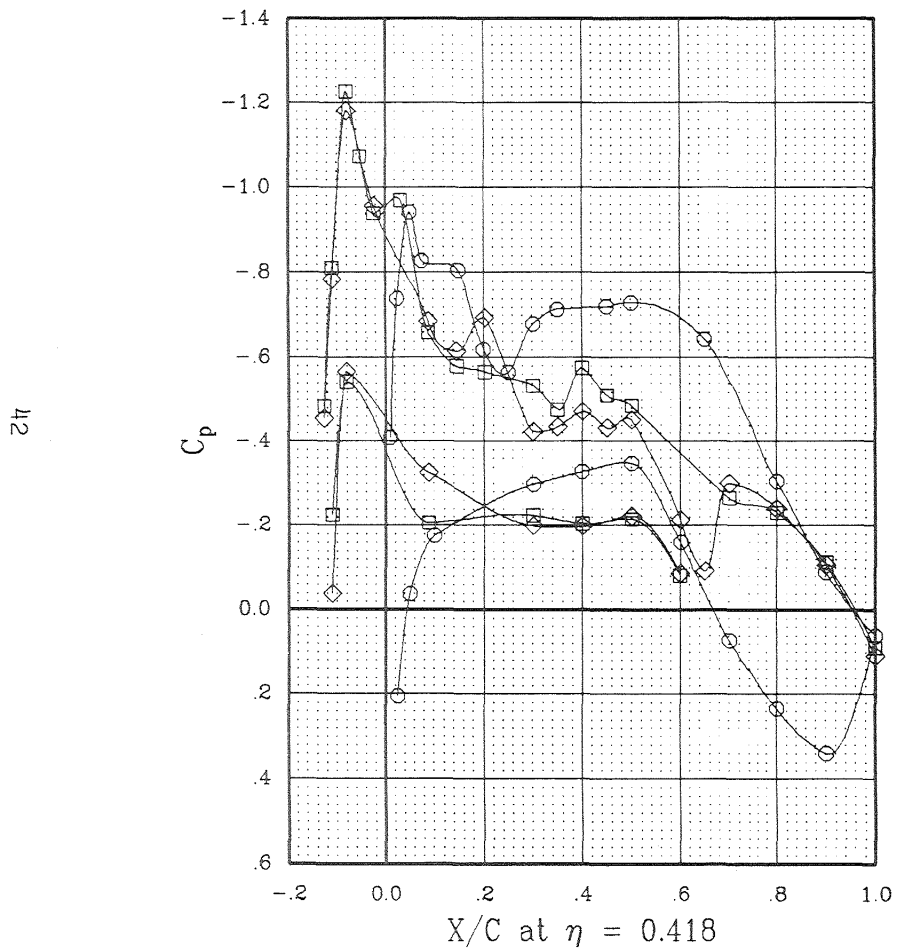
SYMBOL	CONFIGURATION	MACH	ALPHA	EPR
—○—	W B	.801	1.99	1.000
—□—	W B OTWB L H2	.798	1.98	1.963
—◇—	W B OTWB L H2 E	.799	1.98	1.898



(a)  $\eta = 0.250$  and  $0.365$ .

Figure 7.- Blades-off pressure distributions at cruise power.

SYMBOL	CONFIGURATION	MACH	ALPHA	EPR
—○—	W B	.801	1.99	1.000
—□—	W B OTWB L H2	.798	1.98	1.963
—◇—	W B OTWB L H2 E	.799	1.96	1.898

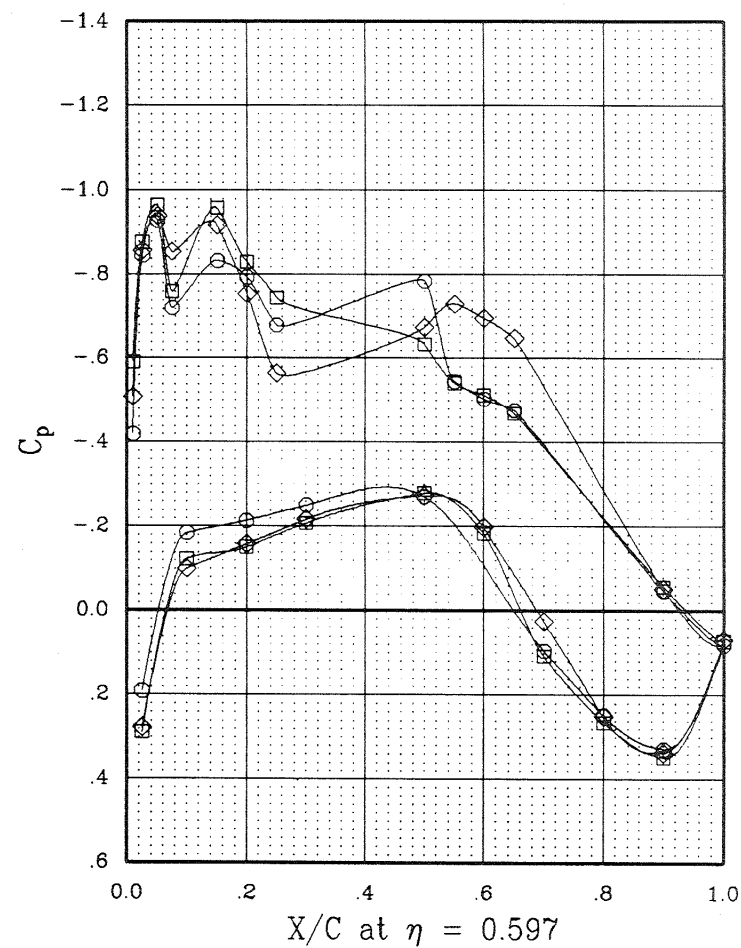
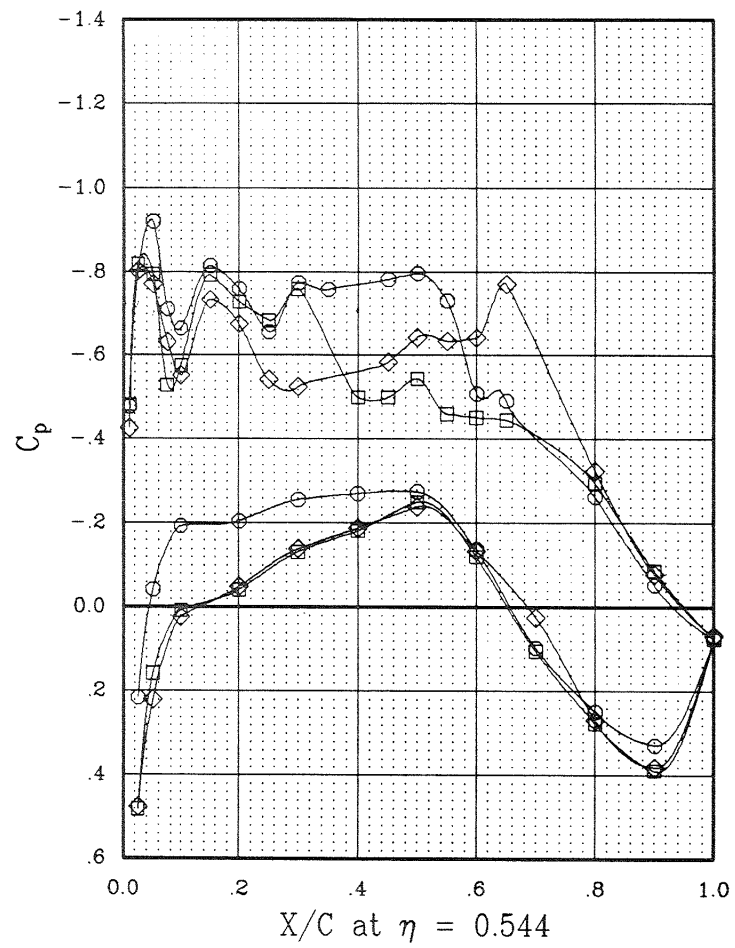


(b)  $\eta = 0.418$  and  $0.481$ .

Figure 7.- Continued.

SYMBOL	CONFIGURATION	MACH	ALPHA	EPR
—○—	W B	.801	1.99	1.000
—□—	W B OTWB L H2	.798	1.98	1.963
—◇—	W B OTWB L H2 E	.799	1.96	1.898

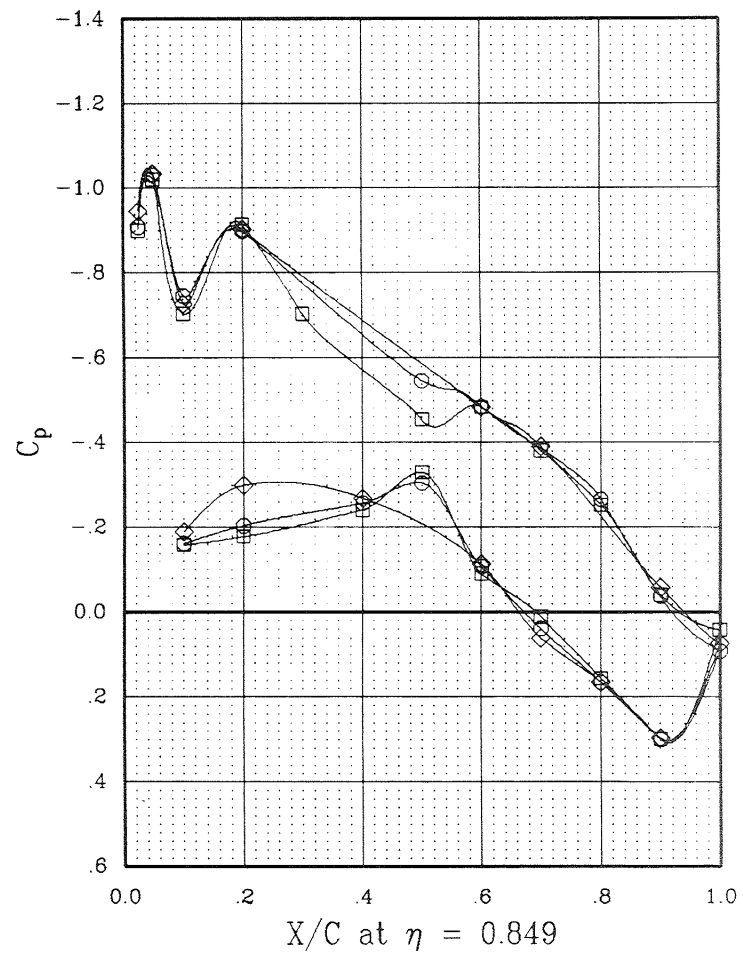
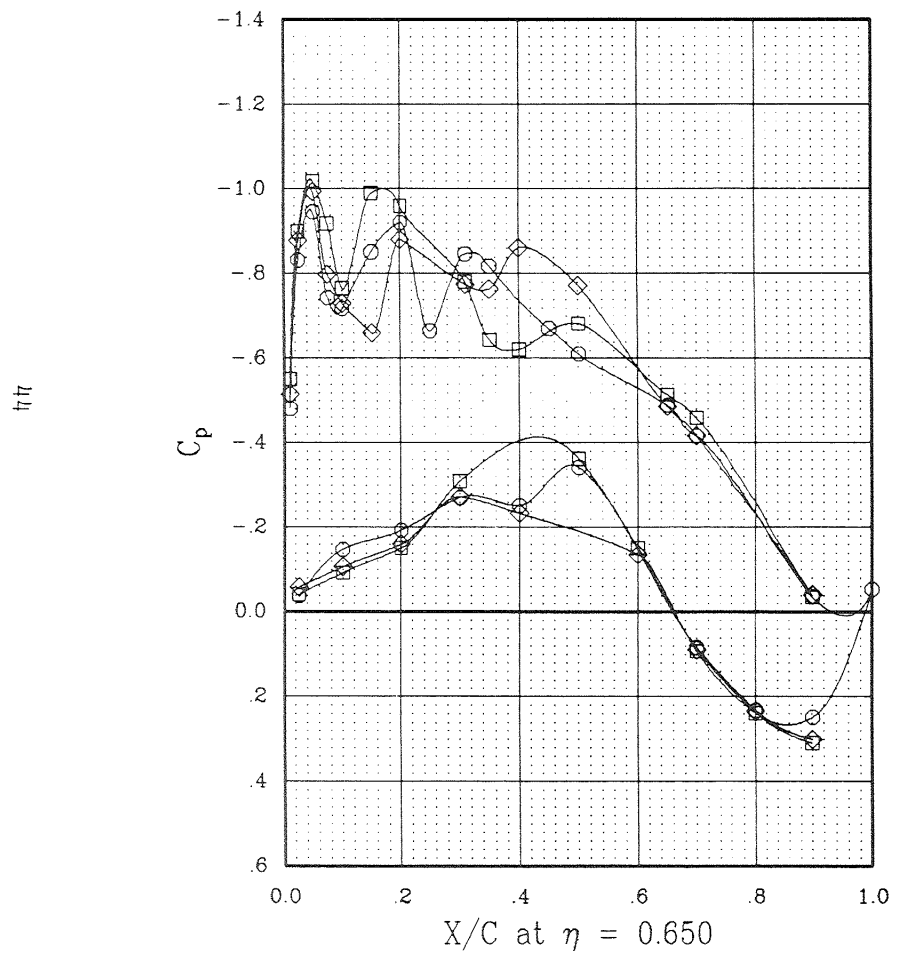
43



(c)  $\eta = 0.544$  and  $0.597$ .

Figure 7.- Continued.

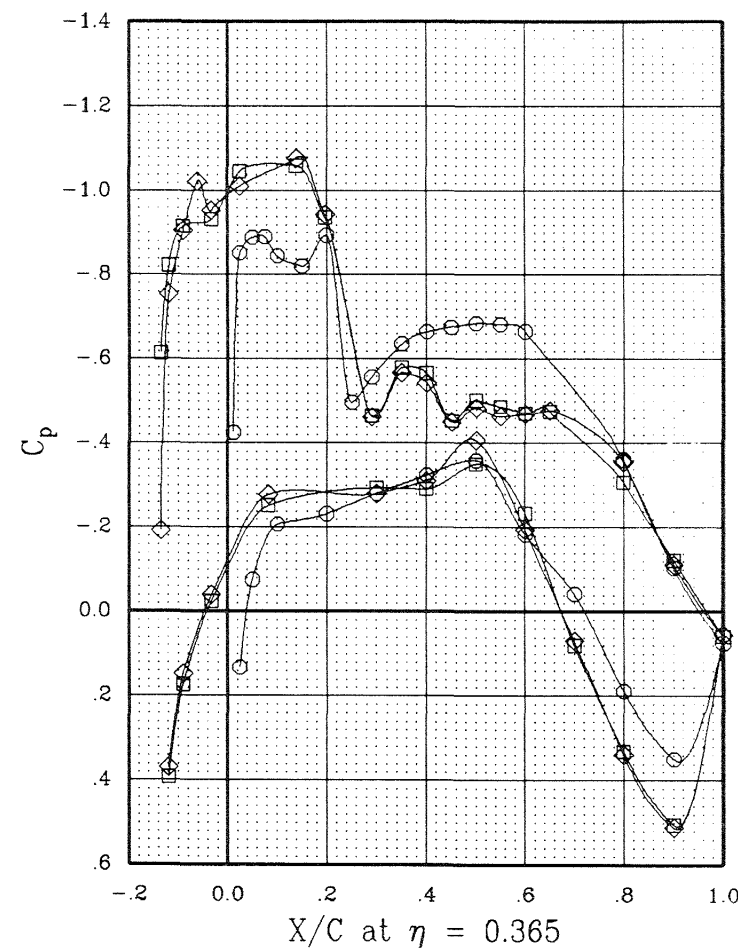
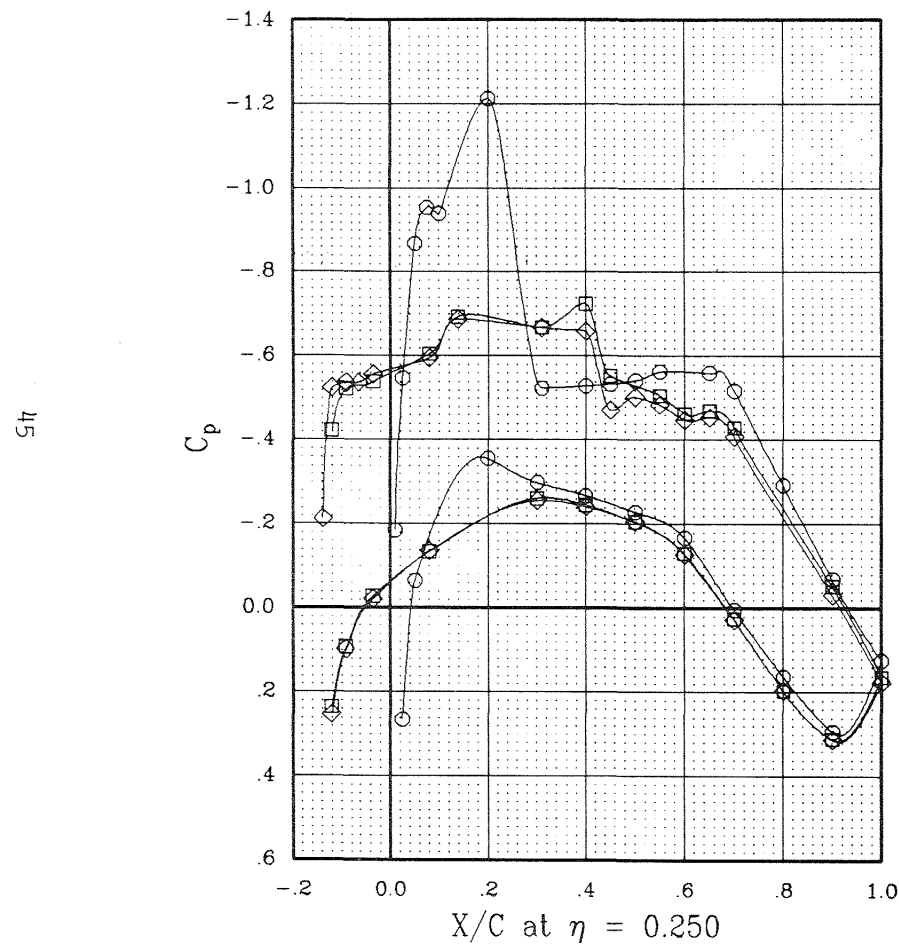
SYMBOL	CONFIGURATION	MACH	ALPHA	EPR
—○—	W B	.801	1.99	1.000
—□—	W B OTWB L H2	.798	1.98	1.963
—◇—	W B OTWB L H2 E	.799	1.98	1.898



(d)  $\eta = 0.650$  and  $0.849$ .

Figure 7.- Concluded.

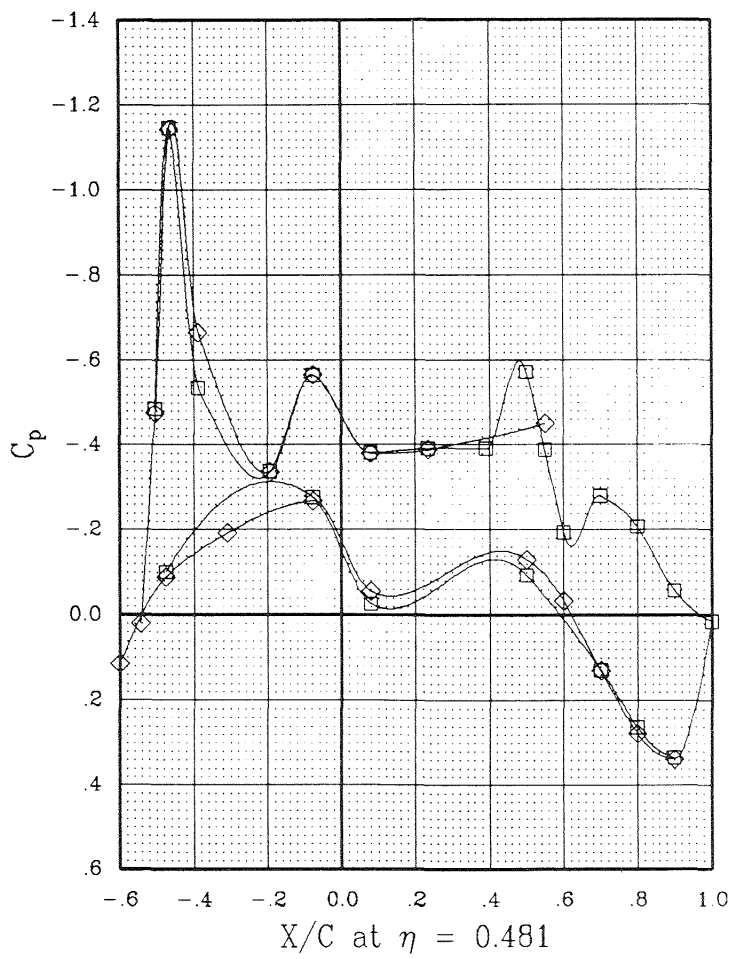
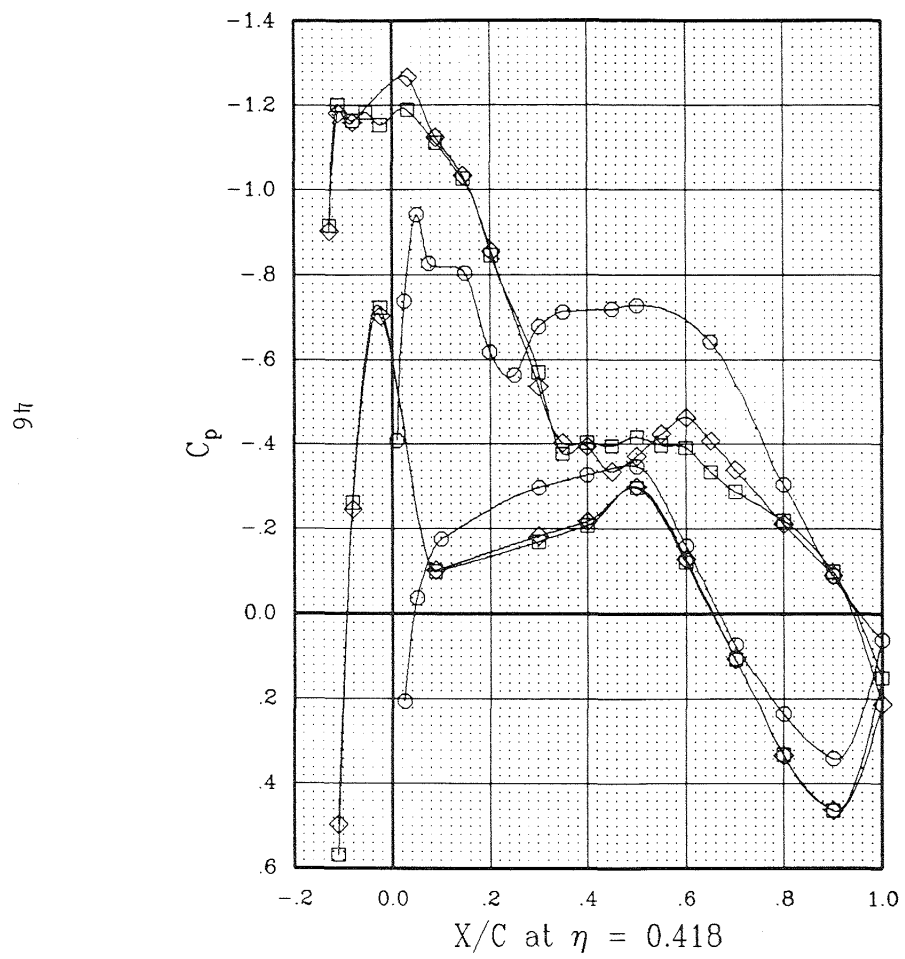
SYMBOL	CONFIGURATION	MACH	ALPHA	BETAP	EPR	RPM
—○—	W B	.801	1.99	0.0	1.000	0
—□—	W B OTW L H2 P2	.796	1.94	56.4	1.908	8347
—◇—	W B OTW L H2 P2 E	.798	1.94	56.4	1.582	8427



(a)  $\eta = 0.250$  and  $0.365$ .

Figure 8.- Blades-on pressure distributions at cruise power.

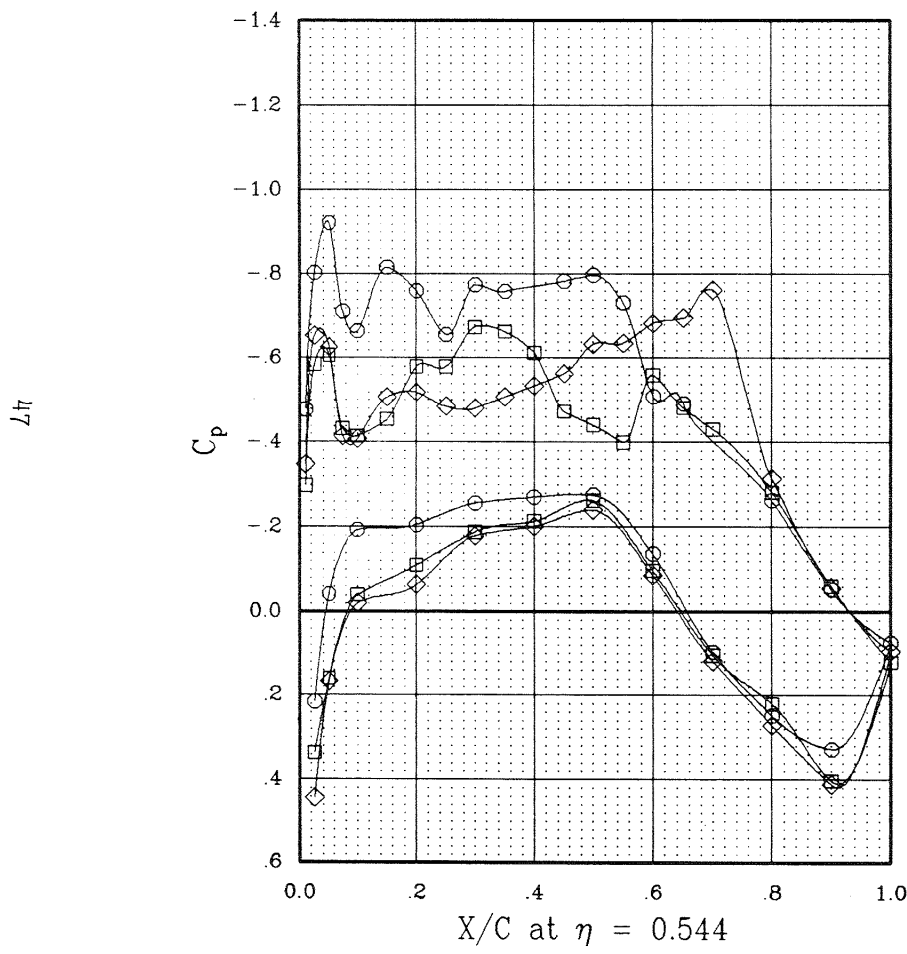
SYMBOL	CONFIGURATION	MACH	ALPHA	BETAP	EPR	RPM
—○—	W B	.801	1.99	0.0	1.000	0
—□—	W B OTW L H2 P2	.798	1.94	56.4	1.908	8347
—◇—	W B OTW L H2 P2 E	.798	1.94	56.4	1.582	8427



(b)  $\eta = 0.418$  and  $0.481$ .

Figure 8.- Continued.

SYMBOL	CONFIGURATION	MACH	ALPHA	BETAP	EPR	RPM
—○—	W B	.801	1.99	0.0	1.000	0
—□—	W B OTW L H2 P2	.796	1.94	56.4	1.908	8347
—◇—	W B OTW L H2 P2 E	.798	1.94	56.4	1.582	8427



(c)  $\eta = 0.544$  and  $0.597$ .

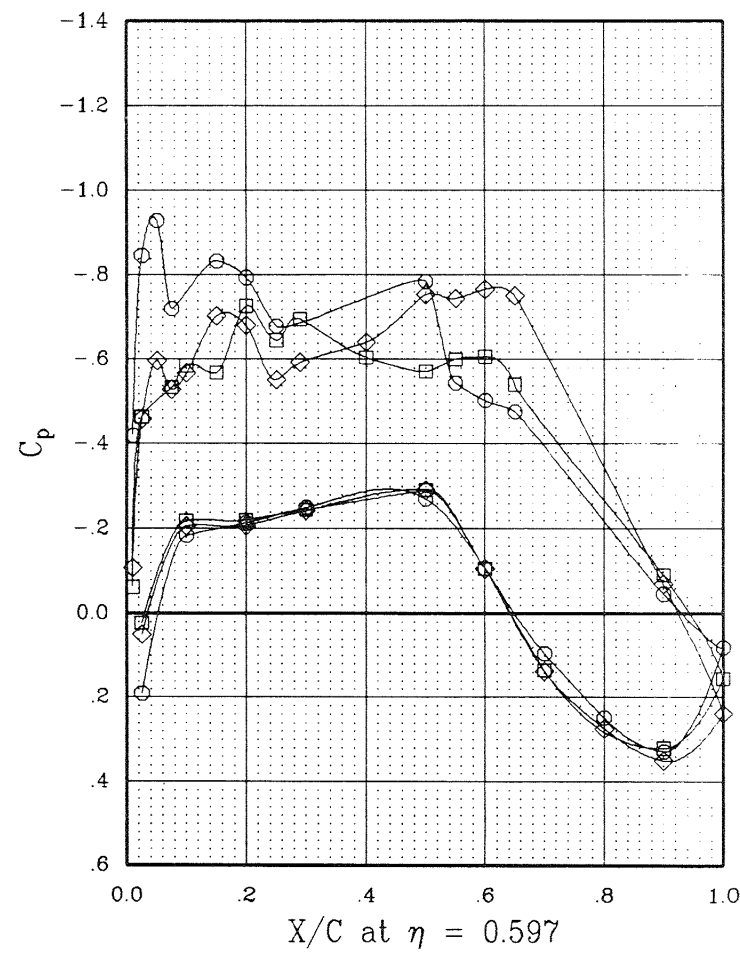
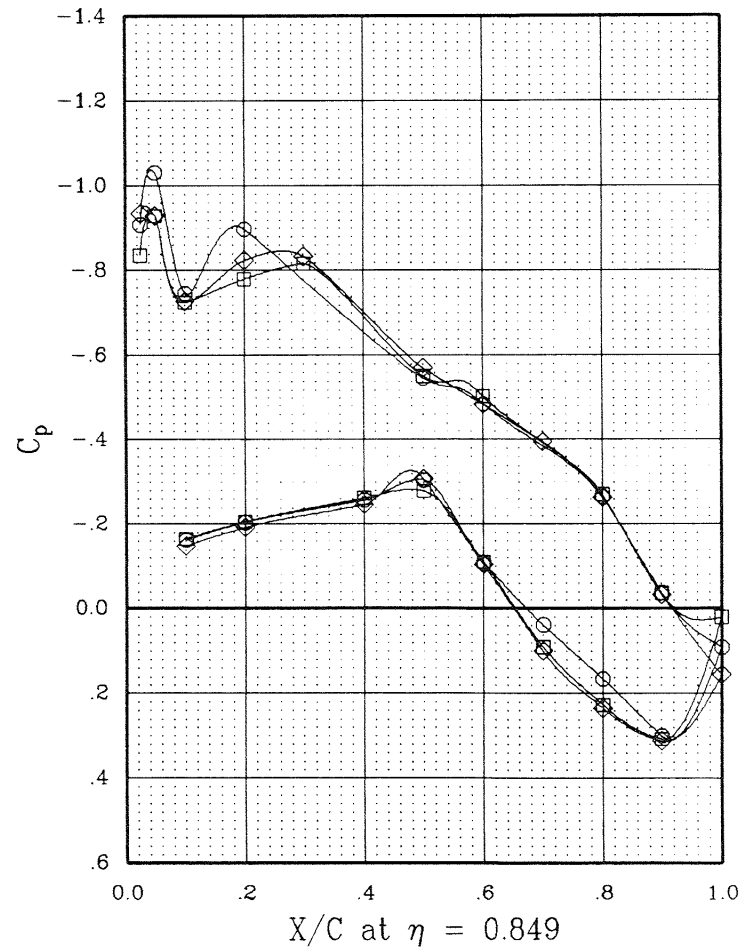
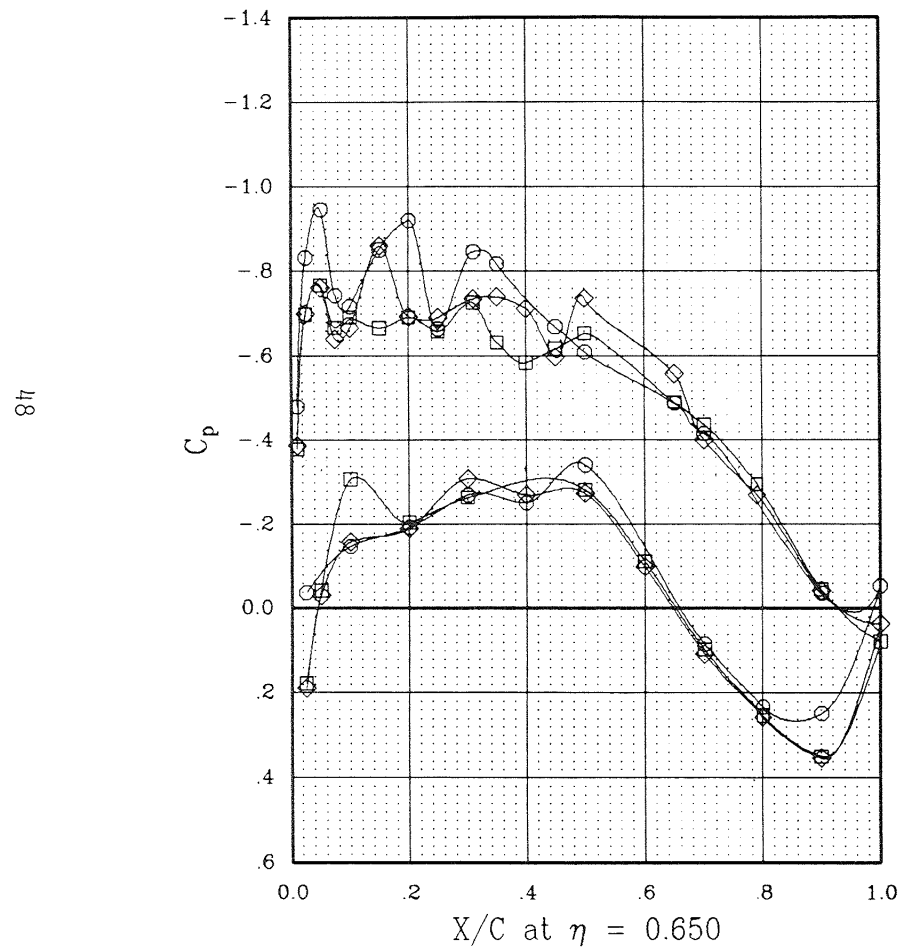


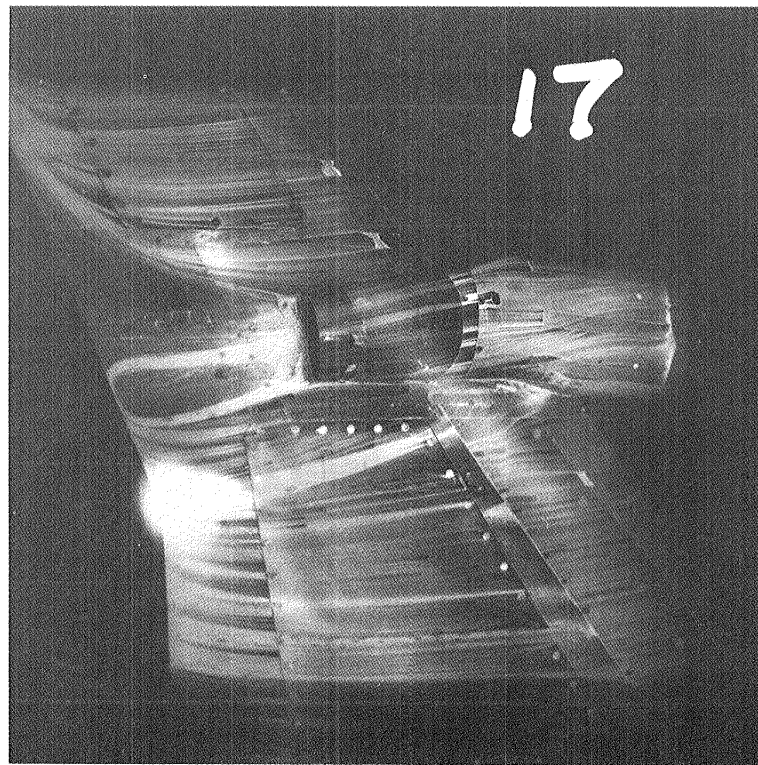
Figure 8.- Continued.

SYMBOL	CONFIGURATION	MACH	ALPHA	BETAP	EPR	RPM
—○—	W B	.801	1.99	0.0	1.000	0
—□—	W B OTW L H2 P2	.796	1.94	56.4	1.908	8347
—◇—	W B OTW L H2 P2 E	.798	1.94	56.4	1.582	8427

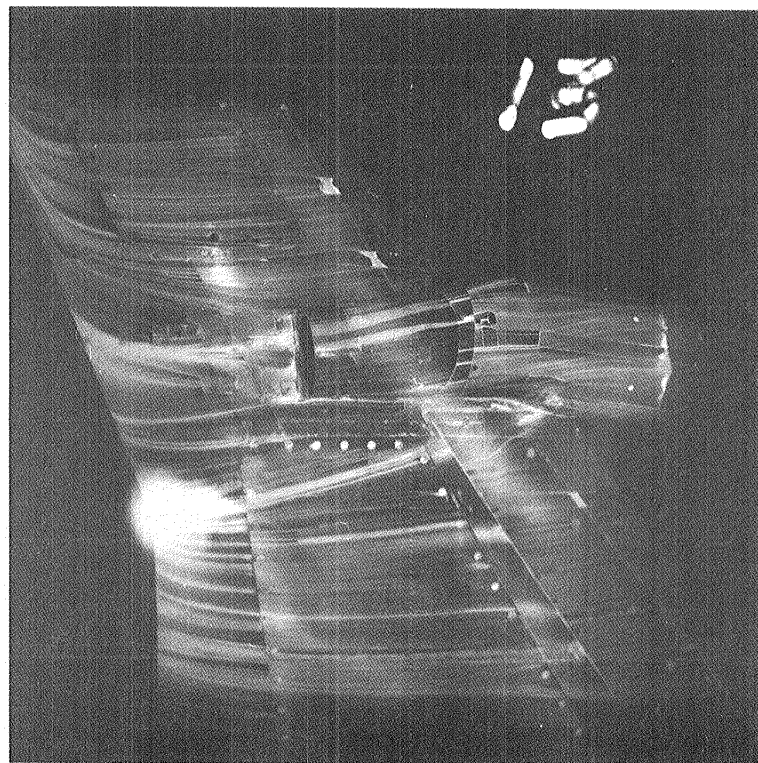


(d)  $\eta = 0.650$  and  $0.849$ .

Figure 8.- Concluded.



(a) Baseline;  $M = 0.8$ ,  $EPR = 1.0$ .

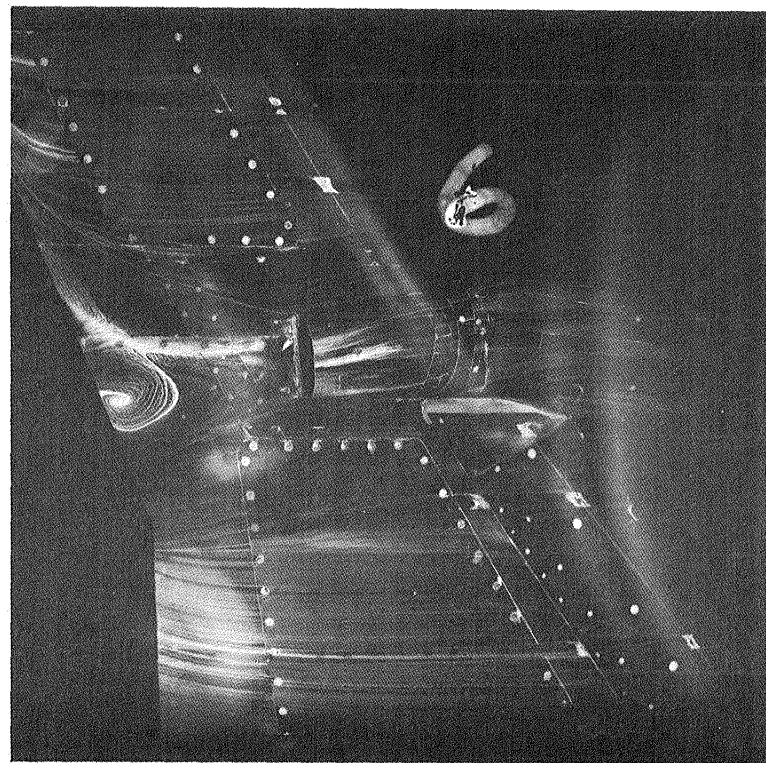


(b) Baseline;  $M = 0.8$ ,  $EPR = 1.8$ .

Figure 9.- Oil flow visualization studies.

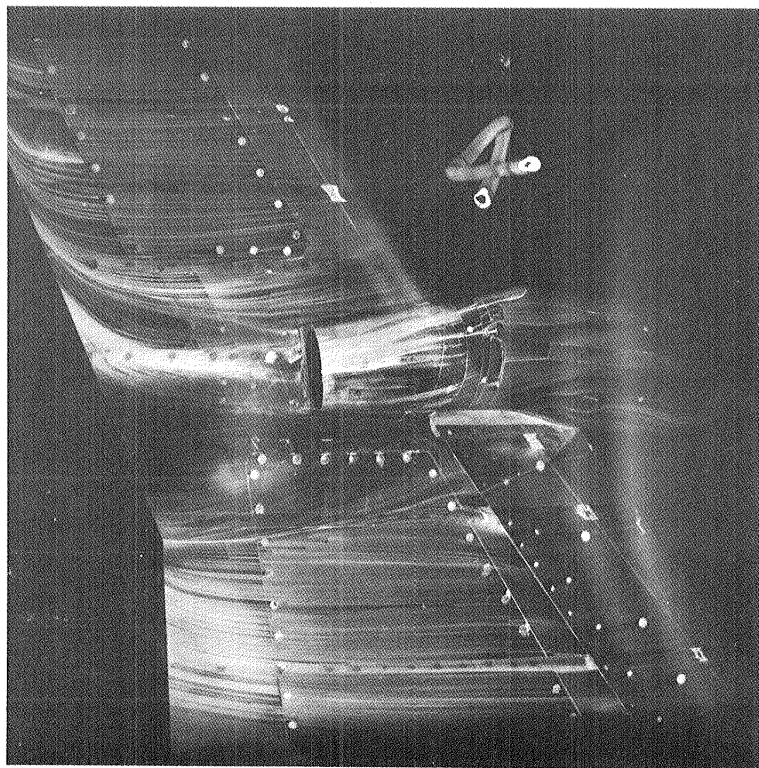


(c) Extended duct;  $M = 0.8$ ,  $EPR = 1.8$ .

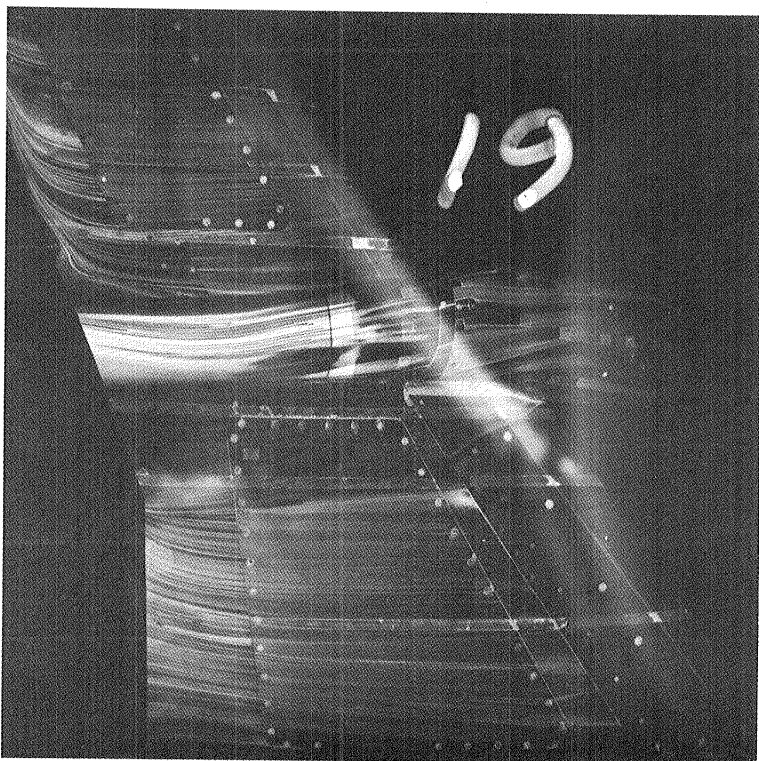


(d) Baseline;  $M = 0.8$ ,  $N = 7400$  rpm.

Figure 9.- Continued.

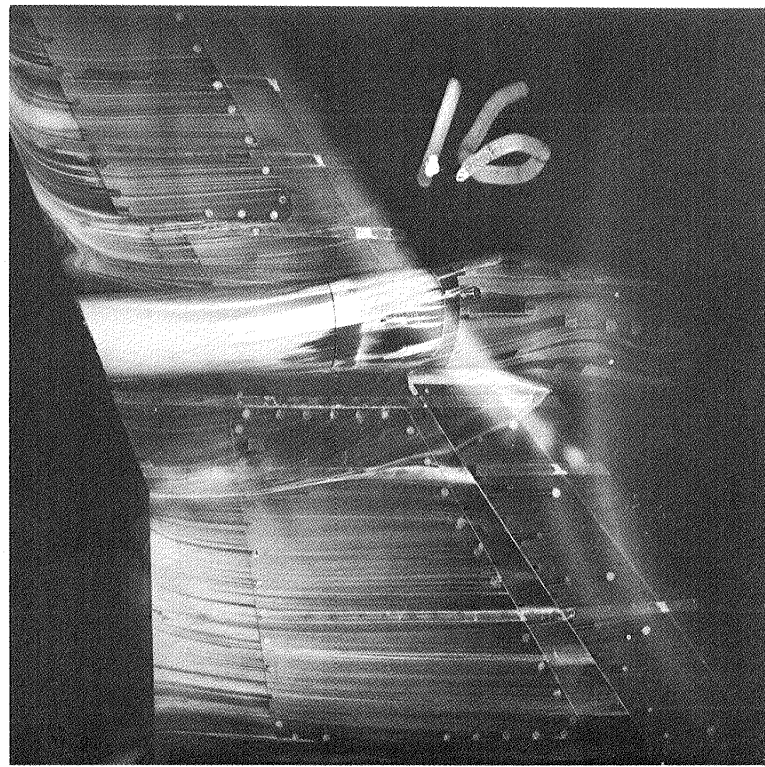


(e) Baseline;  $M = 0.8$ ,  $N = 8400$  rpm.

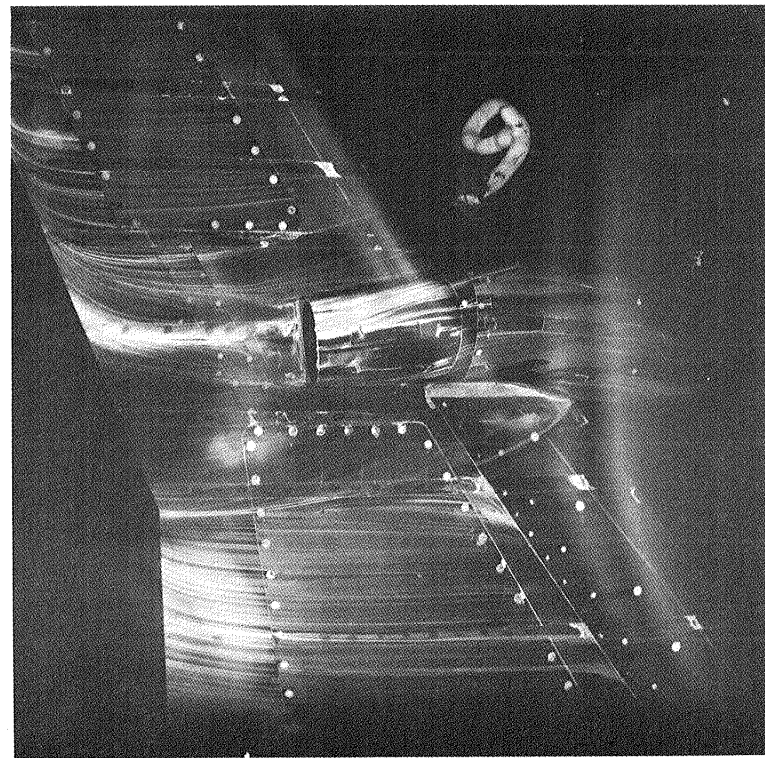


(f) Extended duct;  $M = 0.8$ ,  $N = 7400$  rpm.

Figure 9.- Continued.



(g) Extended duct;  $M = 0.8$ ,  $N = 8400$  rpm.



(h) Baseline;  $M = 0.78$ ,  $N = 8400$  rpm.

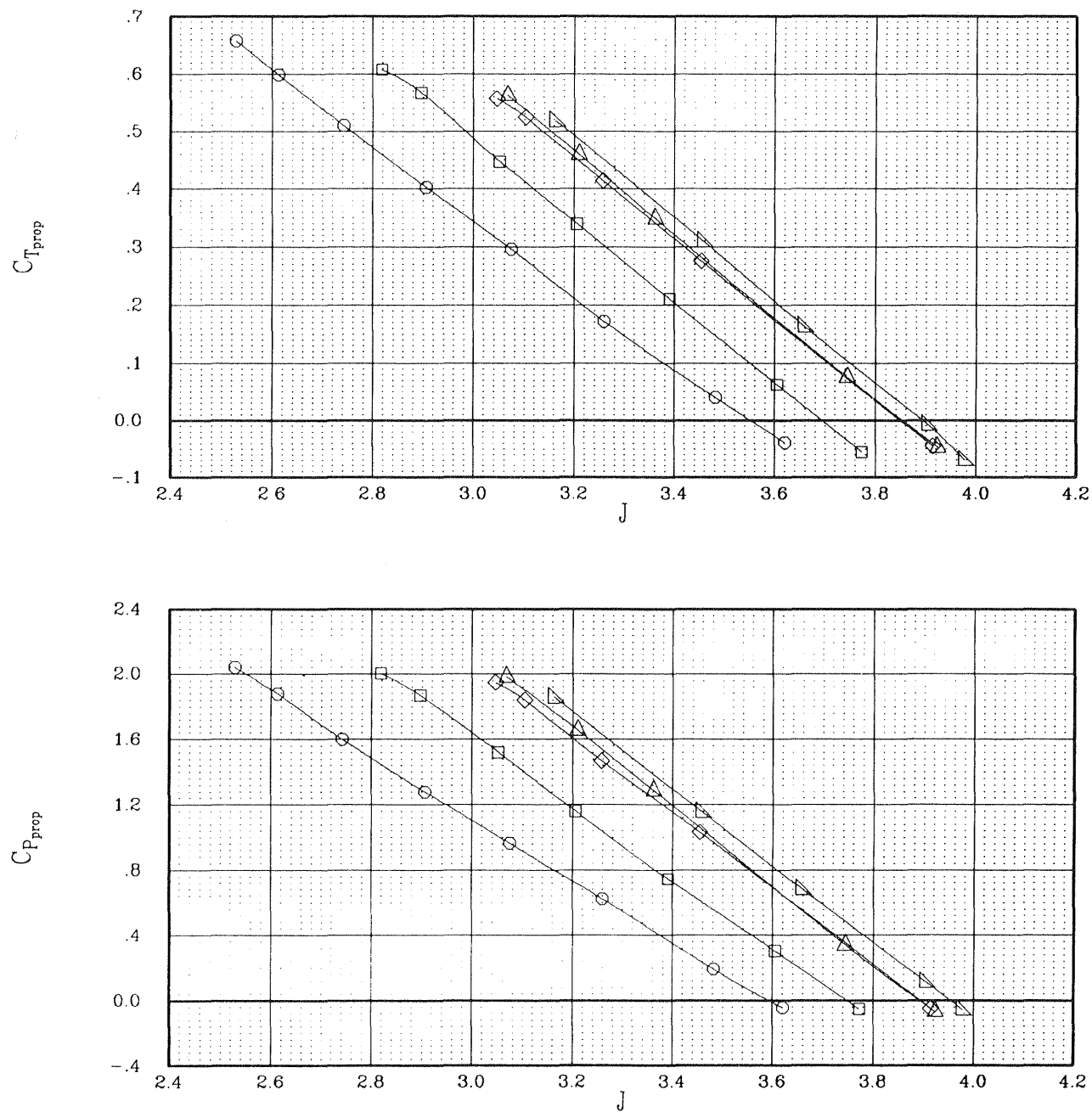
Figure 9.- Continued.



(i) Extended duct;  $M = 0.78$ ,  $N = 8400$  rpm.

Figure 9.- Concluded.

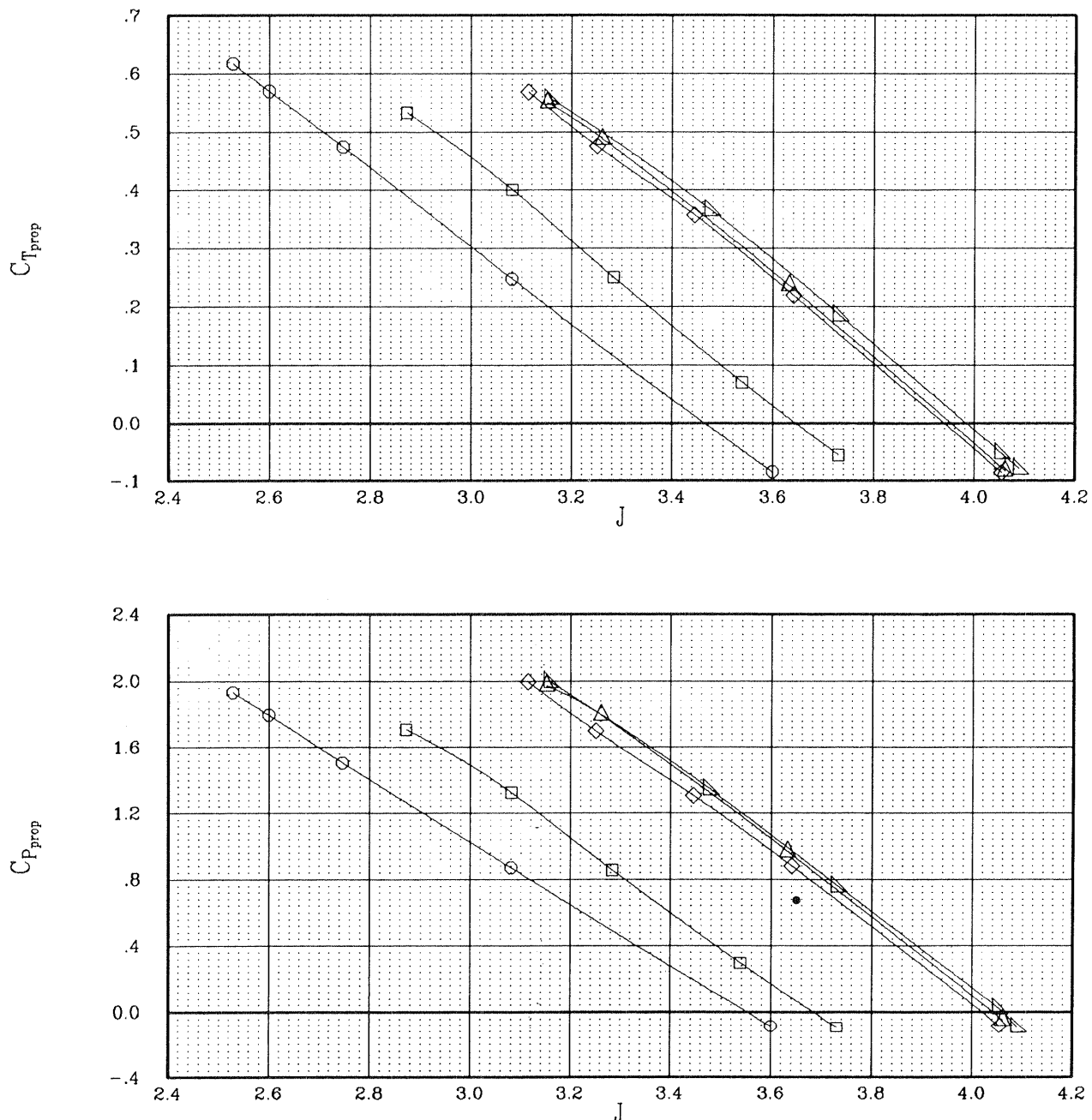
SYMBOL	CONFIGURATION	MACH	ALPHA	BETAP
—○—	W B OTW L H2 P2	.590	2.04	54.8
—□—	W B OTW L H2 P2	.694	2.00	55.6
—◇—	W B OTW L H2 P2	.746	1.97	56.4
—△—	W B OTW L H2 P2	.771	1.96	56.4
—▽—	W B OTW L H2 P2	.798	1.93	56.4



(a) Baseline configuration.

Figure 10.- Effect of Mach number on propeller performance.

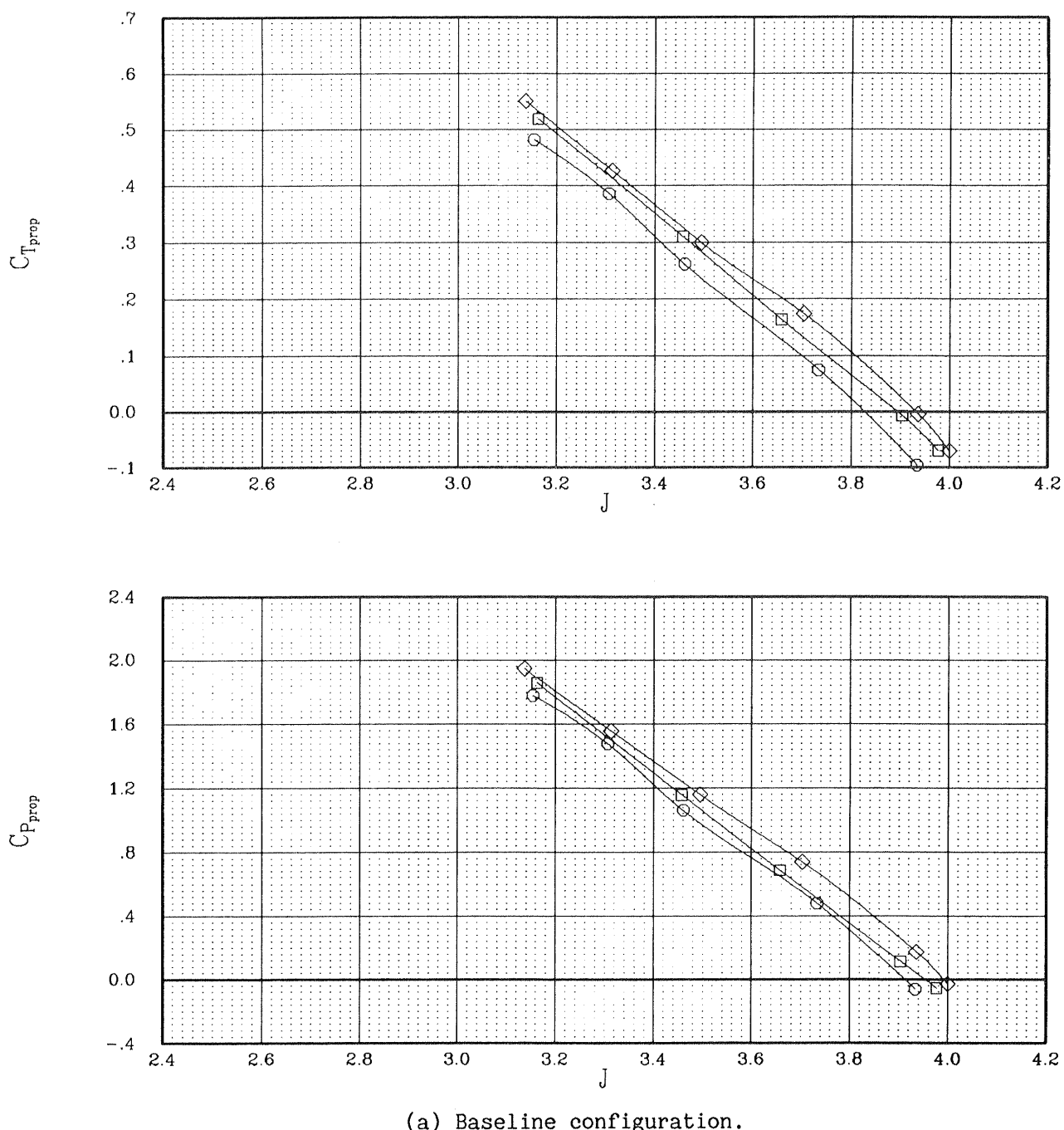
SYMBOL	CONFIGURATION	MACH	ALPHA	BETAP
—○—	W B OTW L H2 P2 E	.592	1.99	54.8
—□—	W B OTW L H2 P2 E	.696	1.98	55.6
—◇—	W B OTW L H2 P2 E	.742	1.99	56.6
—△—	W B OTW L H2 P2 E	.779	1.99	56.8
—▽—	W B OTW L H2 P2 E	.797	1.93	56.6



(b) Extended duct configuration.

Figure 10.- Concluded.

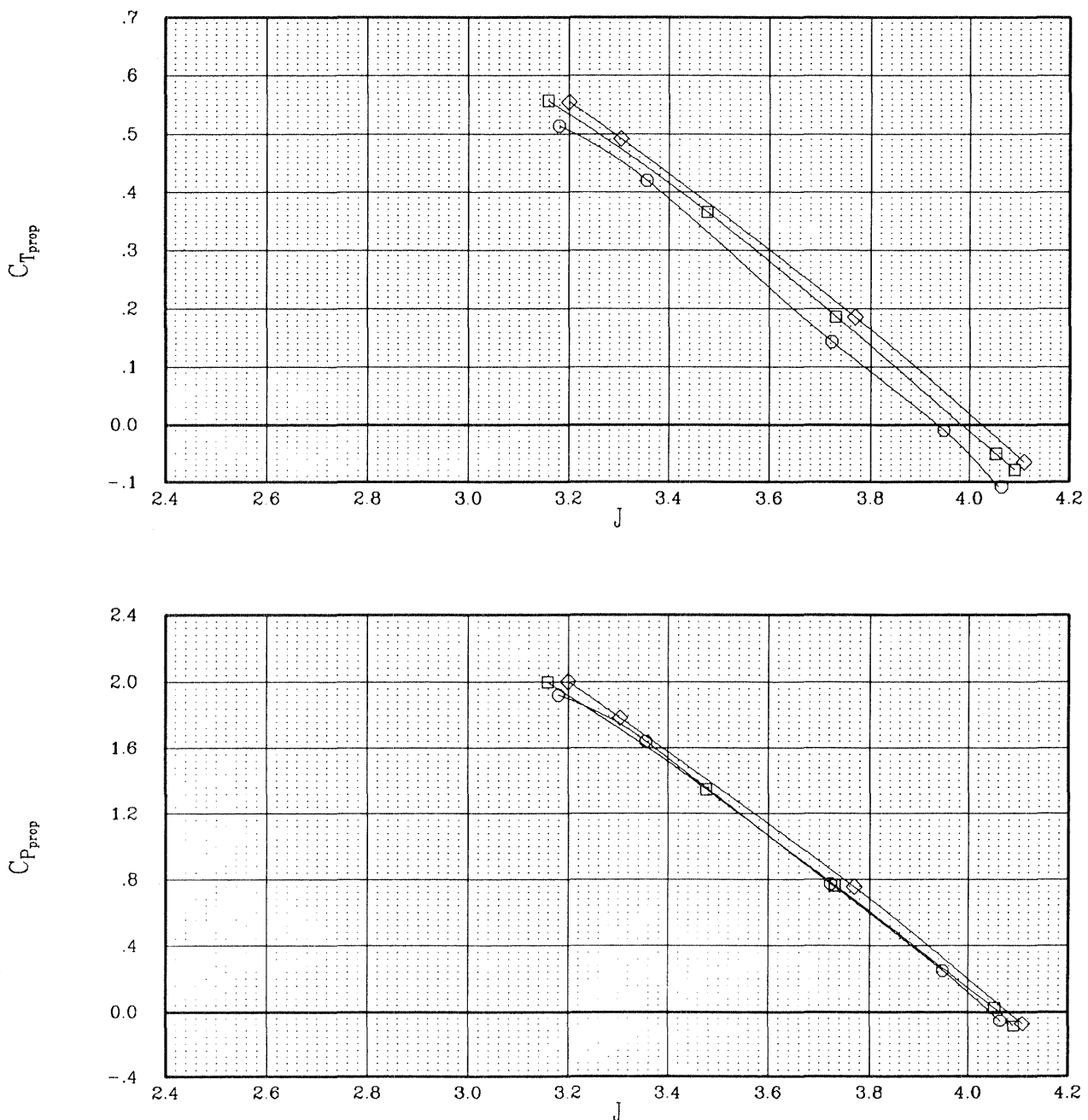
SYMBOL	CONFIGURATION	MACH	ALPHA	BETAP
—○—	W B OTW L H2 P2	.801	.43	56.4
—□—	W B OTW L H2 P2	.798	1.93	56.4
—◇—	W B OTW L H2 P2	.790	3.97	56.4



(a) Baseline configuration.

Figure 11.- Effect of angle of attack on propeller performance.

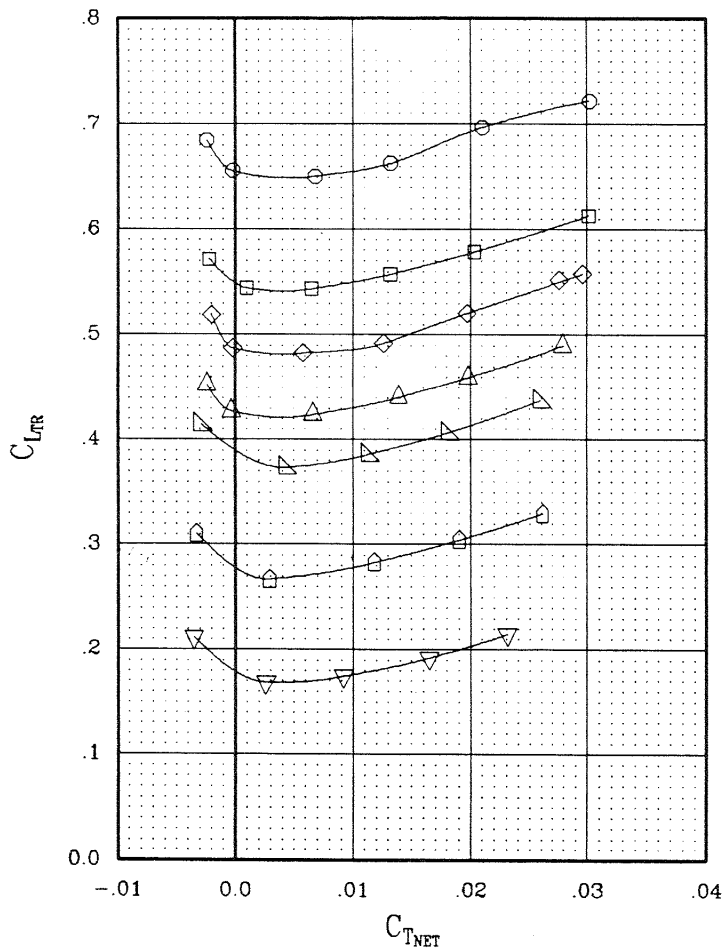
SYMBOL	CONFIGURATION	MACH	ALPHA	BETAP
—○—	W B OTW L H2 P2 E	.803	.46	56.6
—□—	W B OTW L H2 P2 E	.797	1.93	56.6
—◇—	W B OTW L H2 P2 E	.795	3.98	56.6



(b) Extended duct configuration.

Figure 11.- Concluded.

SYMBOL	CONFIGURATION	MACH	ALPHA	BETAP
—○—	W B OTW L H2 P2	.790	3.97	56.4
—□—	W B OTW L H2 P2	.793	3.00	56.4
—◇—	W B OTW L H2 P2	.793	2.47	56.4
—△—	W B OTW L H2 P2	.798	1.93	56.4
—△—	W B OTW L H2 P2	.793	1.46	56.4
—□—	W B OTW L H2 P2	.801	.43	56.4
—▽—	W B OTW L H2 P2	.801	-.55	56.4



(a) Baseline configuration.

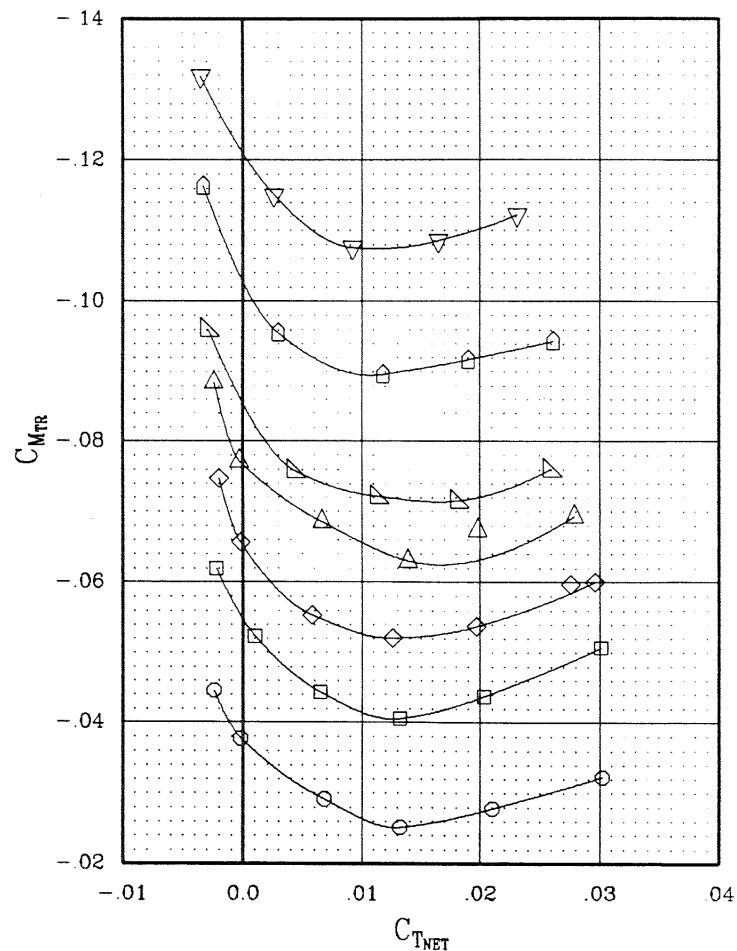
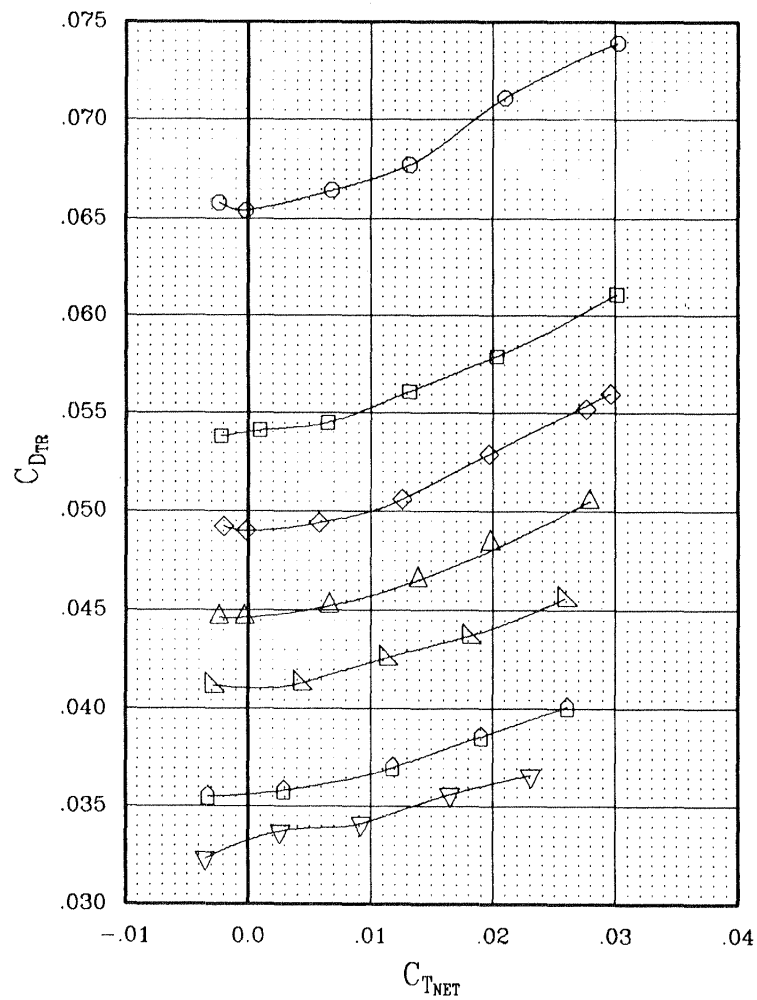


Figure 12.- Effect of thrust on the aerodynamic characteristics.

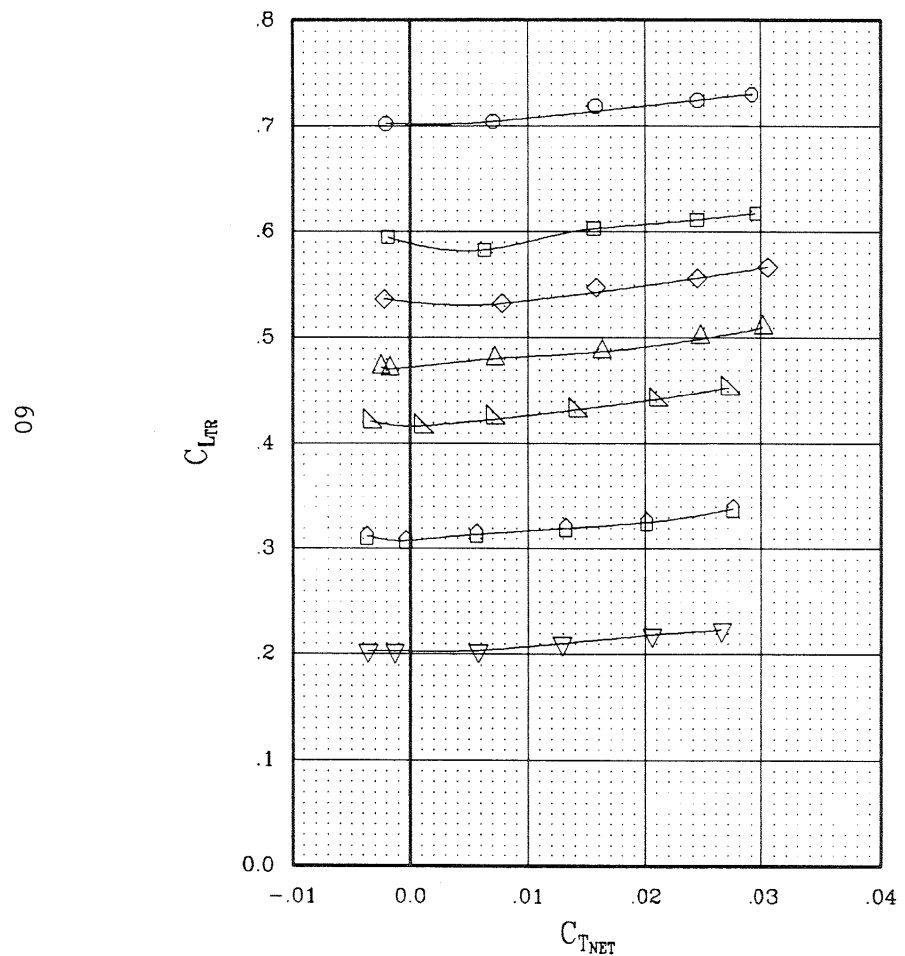
SYMBOL	CONFIGURATION	MACH	ALPHA	BETAP
—○—	W B OTW L H2 P2	.790	3.97	56.4
—□—	W B OTW L H2 P2	.793	3.00	56.4
—◇—	W B OTW L H2 P2	.793	2.47	56.4
—△—	W B OTW L H2 P2	.798	1.93	56.4
—△—	W B OTW L H2 P2	.793	1.46	56.4
—◇—	W B OTW L H2 P2	.801	.43	56.4
—▽—	W B OTW L H2 P2	.801	-.55	56.4



(a) Concluded.

Figure 12.- Continued.

SYMBOL	CONFIGURATION	MACH	ALPHA	BETAP
—○—	W B OTW L H2 P2 E	.795	3.98	56.6
—□—	W B OTW L H2 P2 E	.802	2.95	56.6
—◇—	W B OTW L H2 P2 E	.798	2.45	56.6
—△—	W B OTW L H2 P2 E	.797	1.93	56.6
—□—	W B OTW L H2 P2 E	.802	1.47	56.6
—◇—	W B OTW L H2 P2 E	.803	.46	56.6
—▽—	W B OTW L H2 P2 E	.803	-.55	56.6



(b) Extended duct configuration.

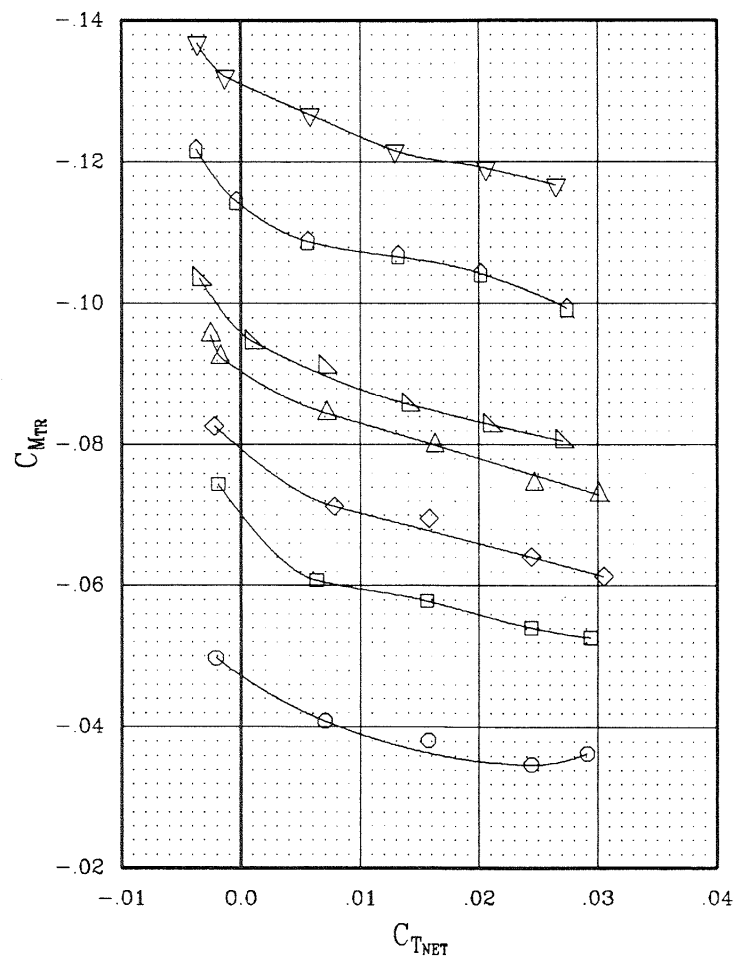
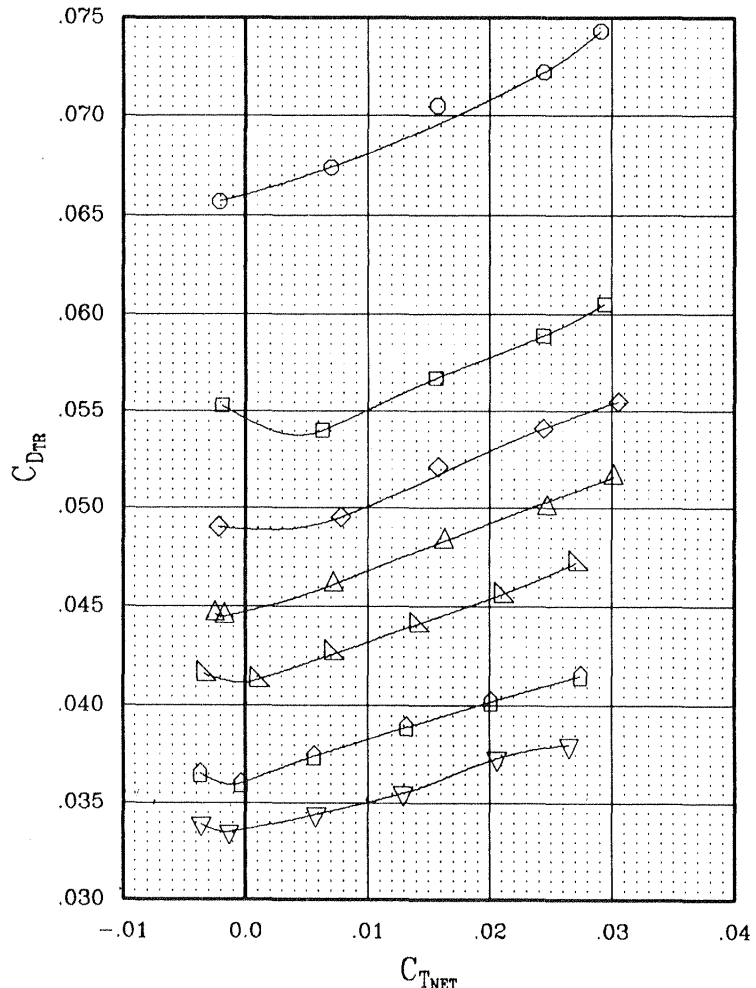


Figure 12.- Continued.

SYMBOL	CONFIGURATION	MACH	ALPHA	BETAP
—○—	W B OTW L H2 P2 E	.795	3.98	56.6
—□—	W B OTW L H2 P2 E	.802	2.95	56.6
—◇—	W B OTW L H2 P2 E	.796	2.45	56.6
—△—	W B OTW L H2 P2 E	.797	1.93	56.6
—▽—	W B OTW L H2 P2 E	.802	1.47	56.6
—◇—	W B OTW L H2 P2 E	.803	.46	56.6
—▽—	W B OTW L H2 P2 E	.803	-.55	56.6

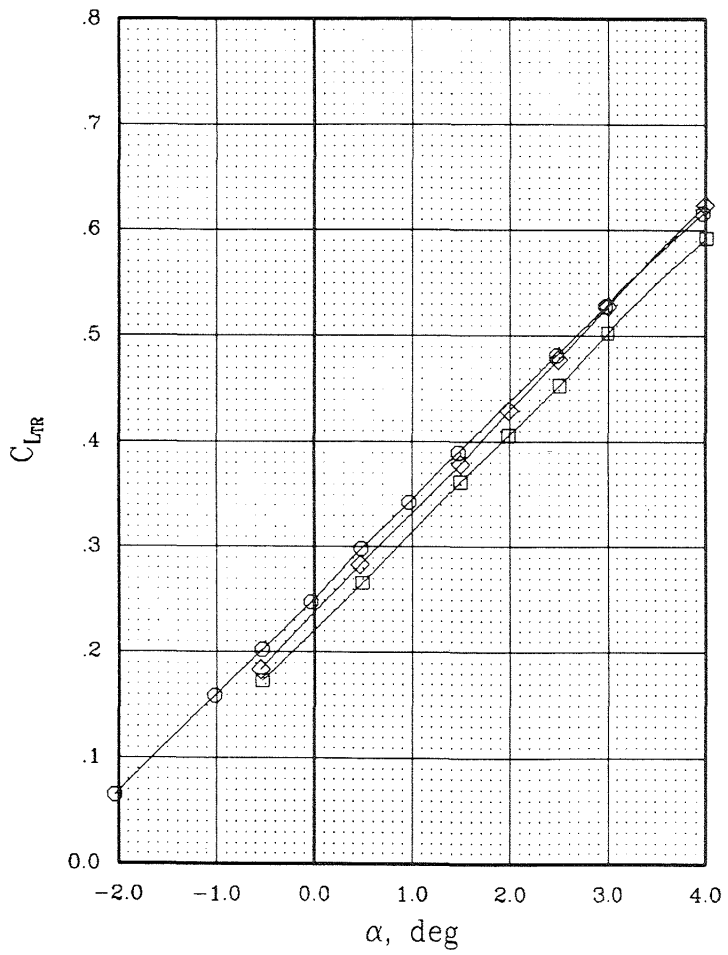


(b) Concluded.

Figure 12.- Concluded.

SYMBOL	CONFIGURATION	MACH	BETA	EPR	CTNET
—○—	W B	.597	0.0	1.000	0.0
—□—	W B OTWB L H2	.589	0.0	1.104	0.0
—◇—	W B OTW L H2 P2	.588	54.8	1.104	.025

62



(a)  $M_{\infty} = 0.60$ .

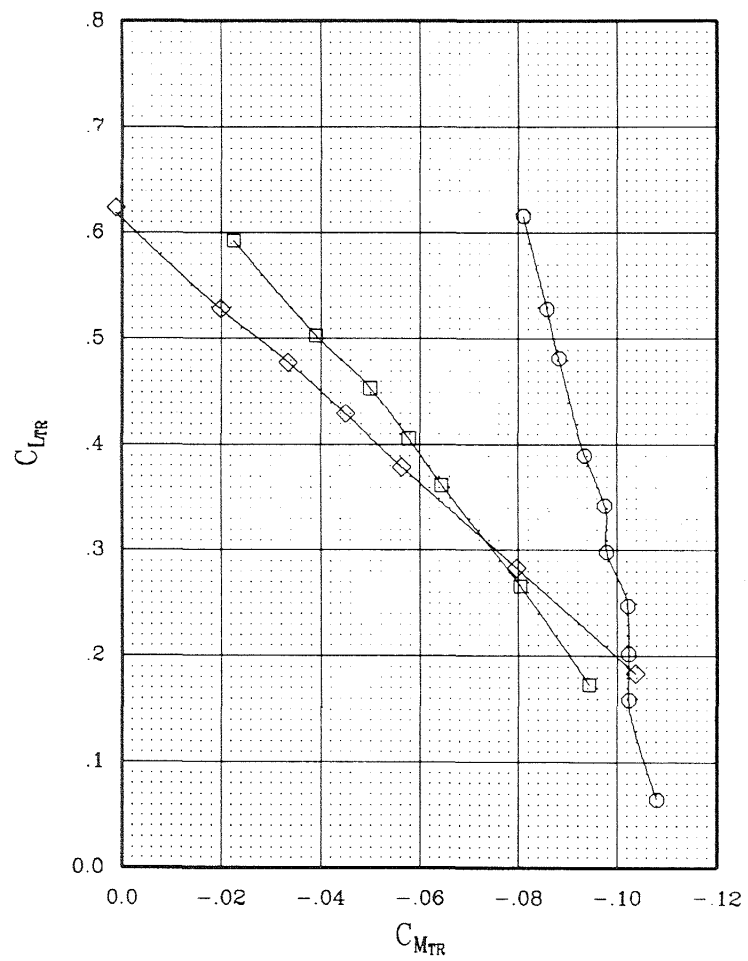
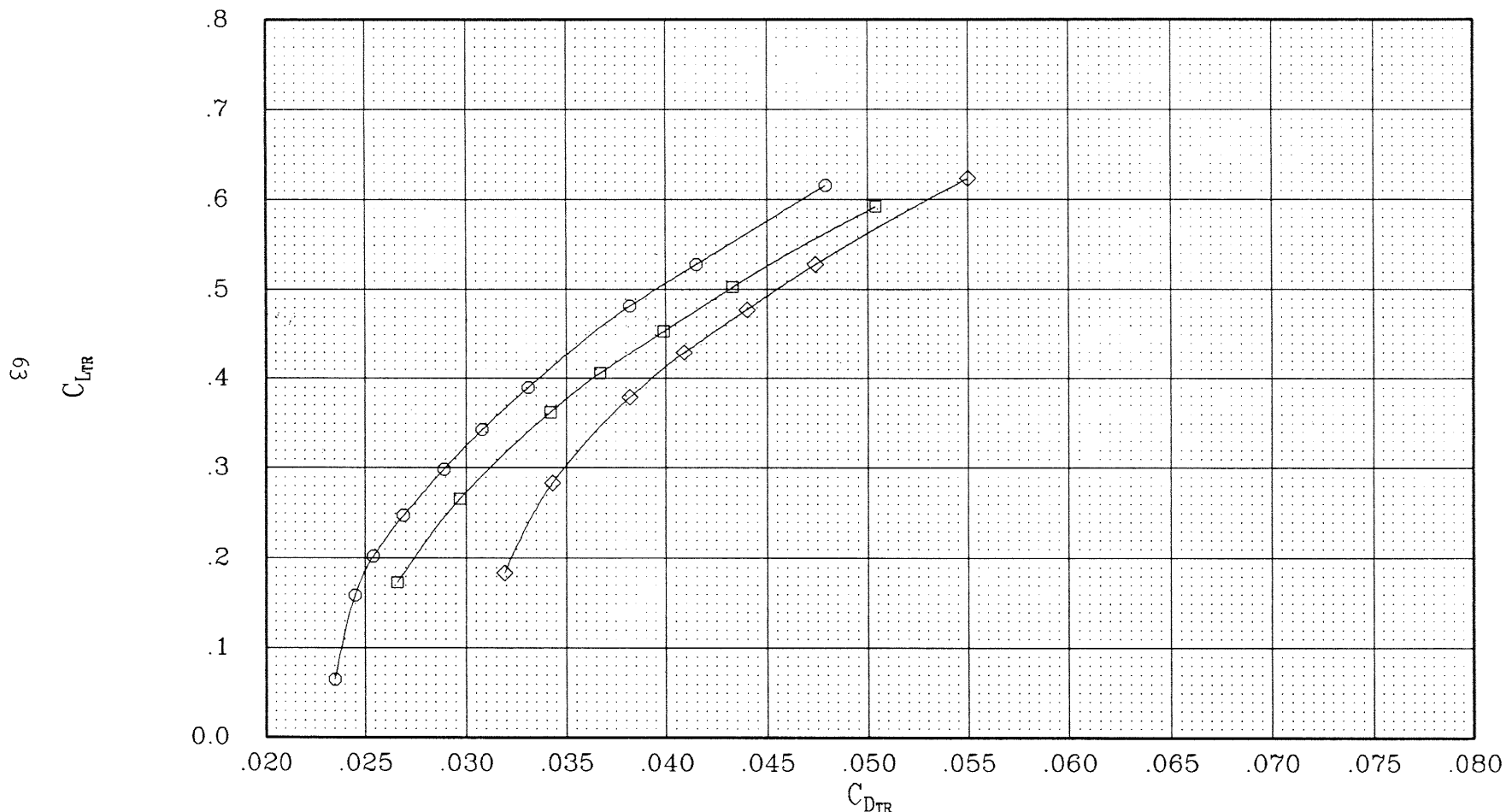


Figure 13.- Baseline aerodynamic characteristics at cruise power.

SYMBOL	CONFIGURATION	MACH	BETA	EPR	CTNET
—○—	W B	.597	0.0	1.000	0.0
—□—	W B OTWB L H2	.589	0.0	1.104	0.0
—◇—	W B OTW L H2 P2	.588	54.8	1.104	.025

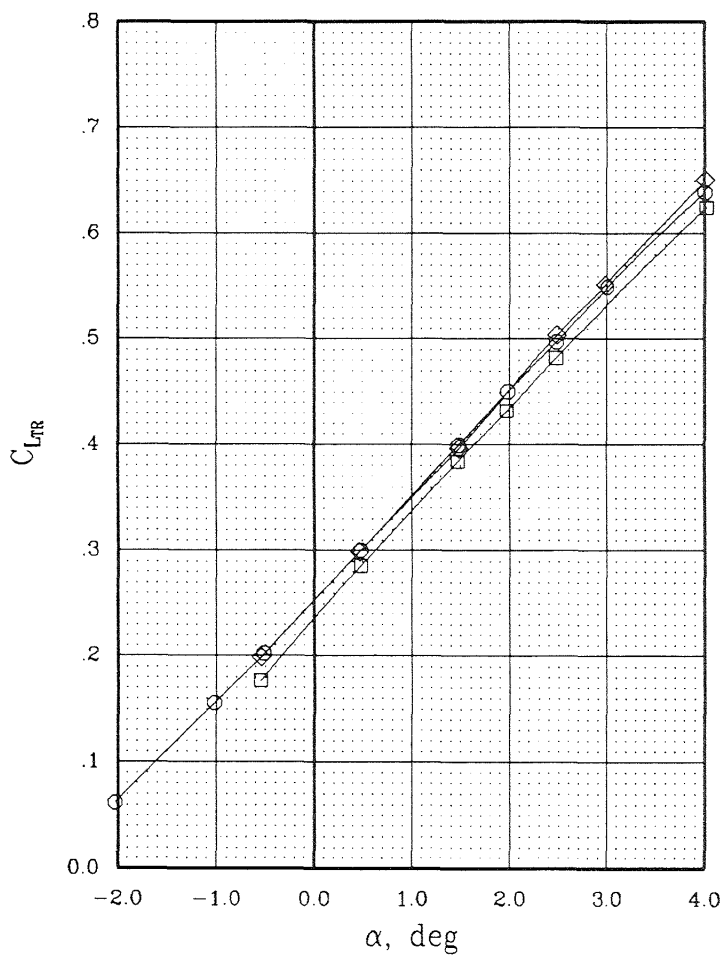


(a)  $M_\infty = 0.60$ .

Figure 13.- Continued.

SYMBOL	CONFIGURATION	MACH	BETA	EPR	CTNET
—○—	W B	.699	0.0	1.000	0.0
—□—	W B OTWB L H2	.699	0.0	1.274	0.0
—◇—	W B OTW L H2 P2	.702	55.6	1.274	.026

49



(b)  $M_{\infty} = 0.70$ .

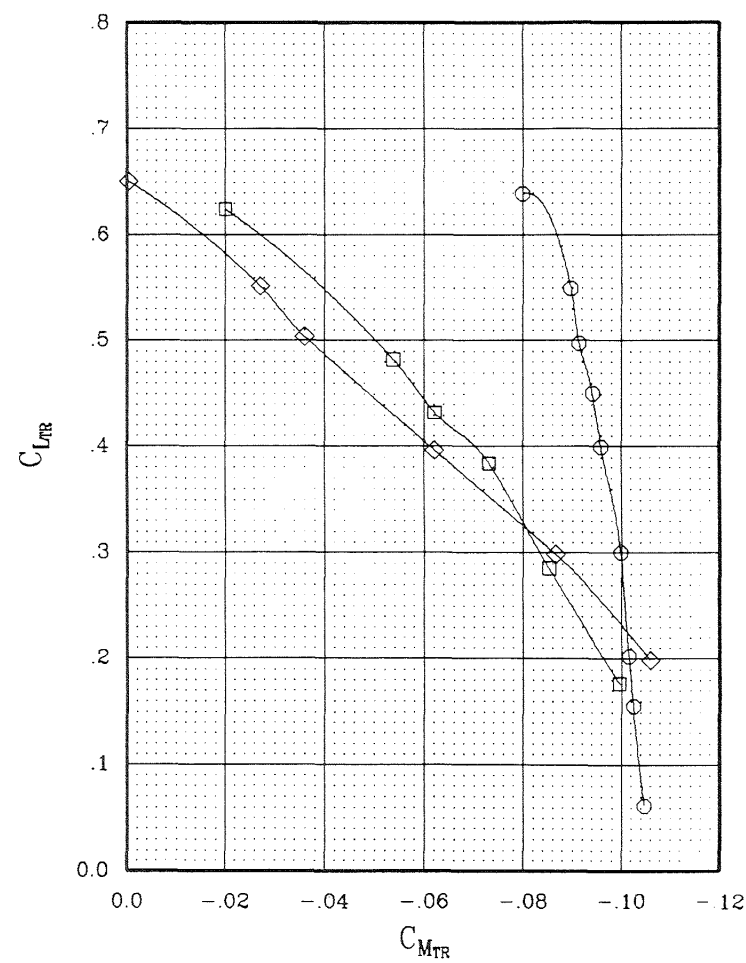
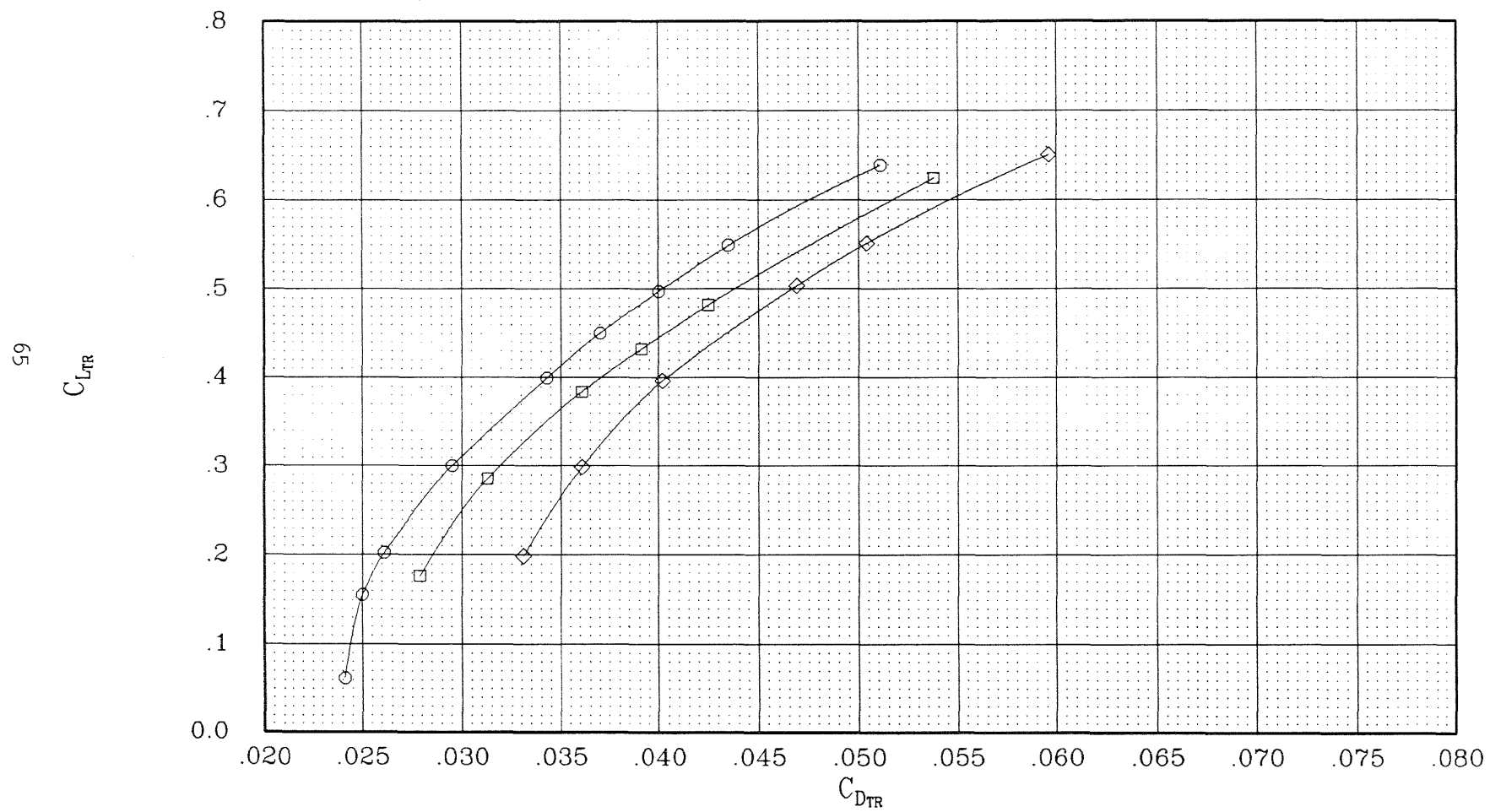


Figure 13.- Continued.

SYMBOL	CONFIGURATION	MACH	BETA	EPR	CTNET
—○—	W B	.699	0.0	1.000	0.0
—□—	W B OTWB L H2	.699	0.0	1.274	0.0
—◇—	W B OTW L H2 P2	.702	55.6	1.274	.026



(b)  $M_{\infty} = 0.70$ .

Figure 13.- Continued.

SYMBOL	CONFIGURATION	MACH	BETA	EPR	CTNET
—○—	W B	.749	0.0	1.000	0.0
—□—	W B OTWB L H2	.751	0.0	1.590	0.0
—◇—	W B OTW L H2 P2	.749	56.6	1.590	.028

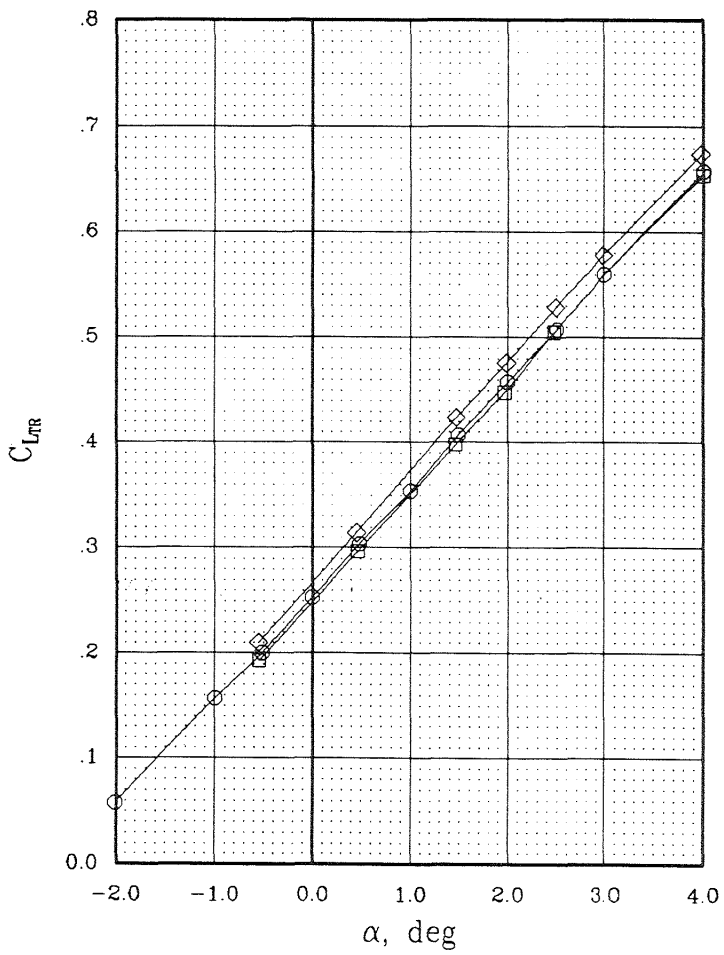
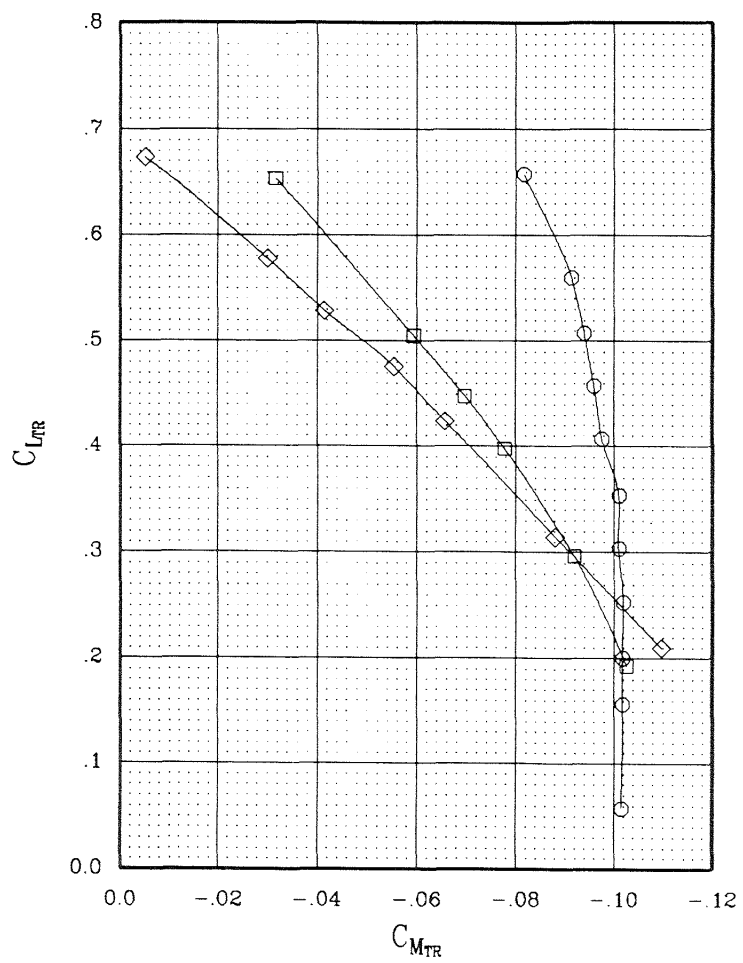
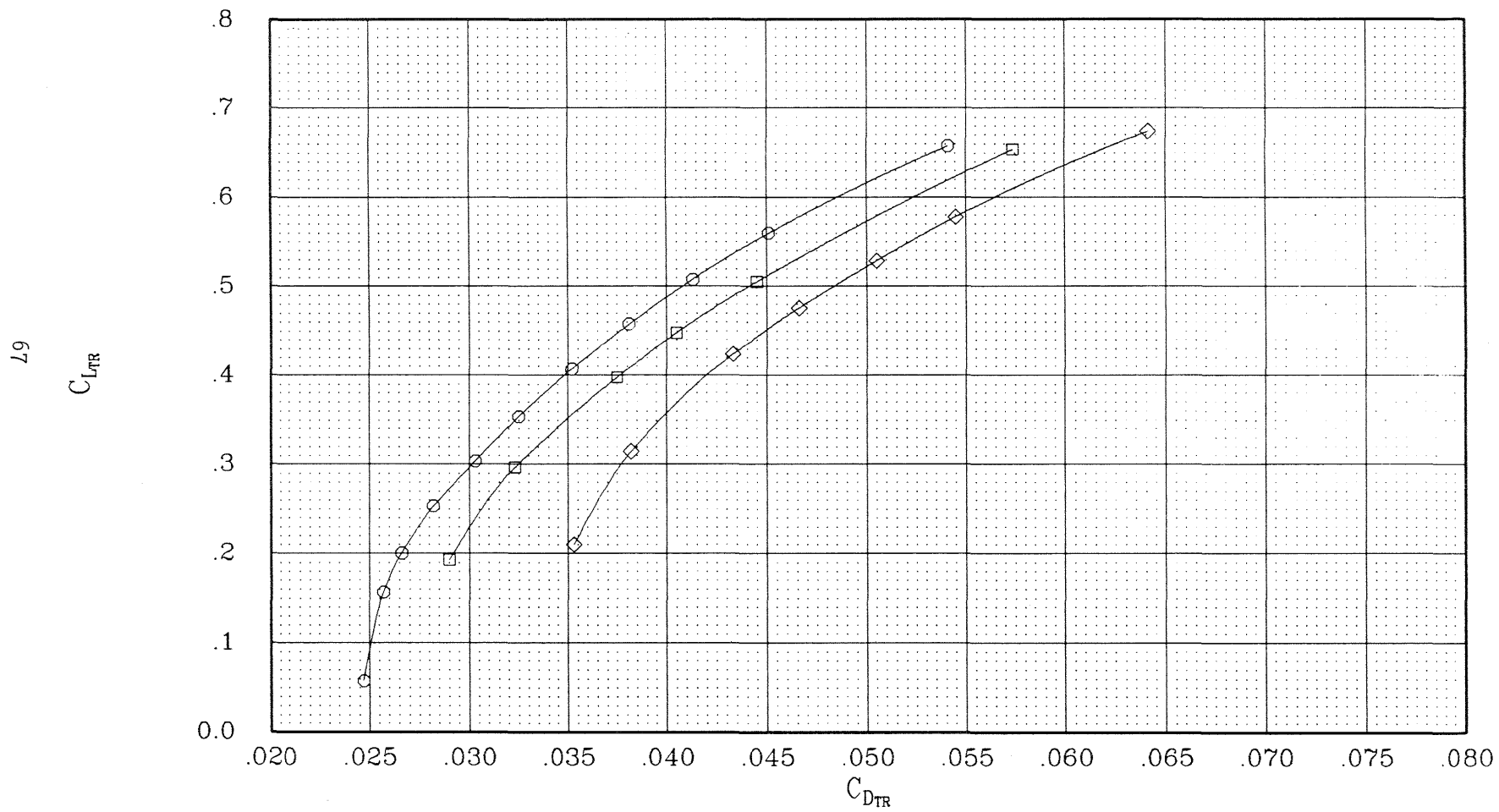
(c)  $M_{\infty} = 0.75$ .

Figure 13.- Continued.

SYMBOL	CONFIGURATION	MACH	BETA	EPR	CTNET
—○—	W B	.749	0.0	1.000	0.0
—□—	W B OTWB L H2	.751	0.0	1.590	0.0
—◇—	W B OTW L H2 P2	.749	56.6	1.590	.028



(c)  $M_{\infty} = 0.75$ .

Figure 13.- Continued.

SYMBOL	CONFIGURATION	MACH	BETA	EPR	CTNET
—○—	W B	.784	0.0	1.000	0.0
—□—	W B OTWB L H2	.773	0.0	1.712	0.0
—◇—	W B OTW L H2 P2	.776	56.6	1.712	.028

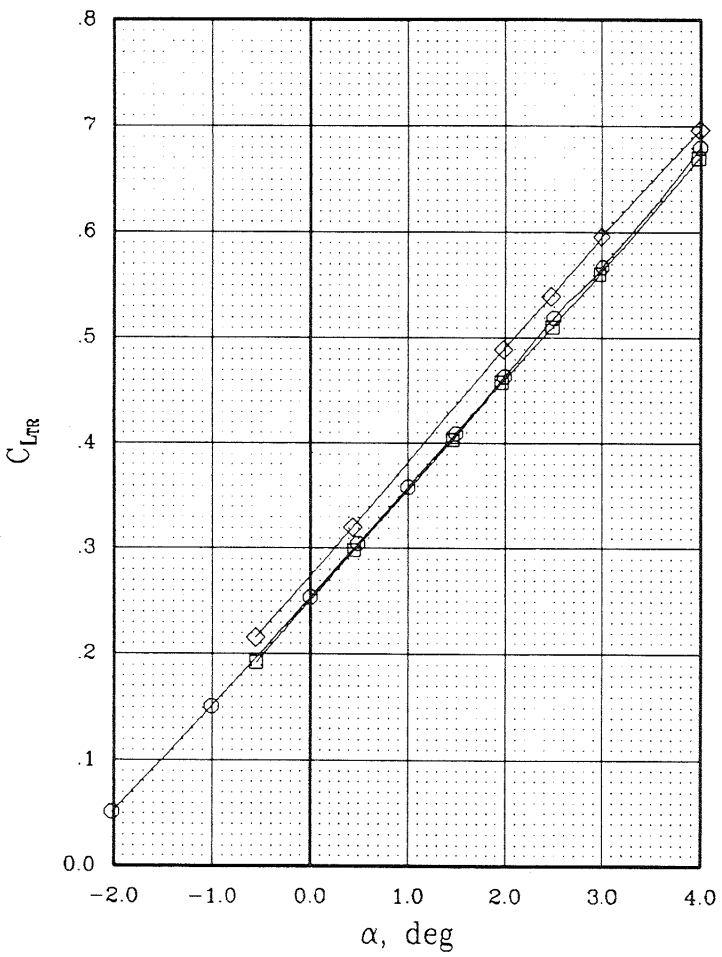
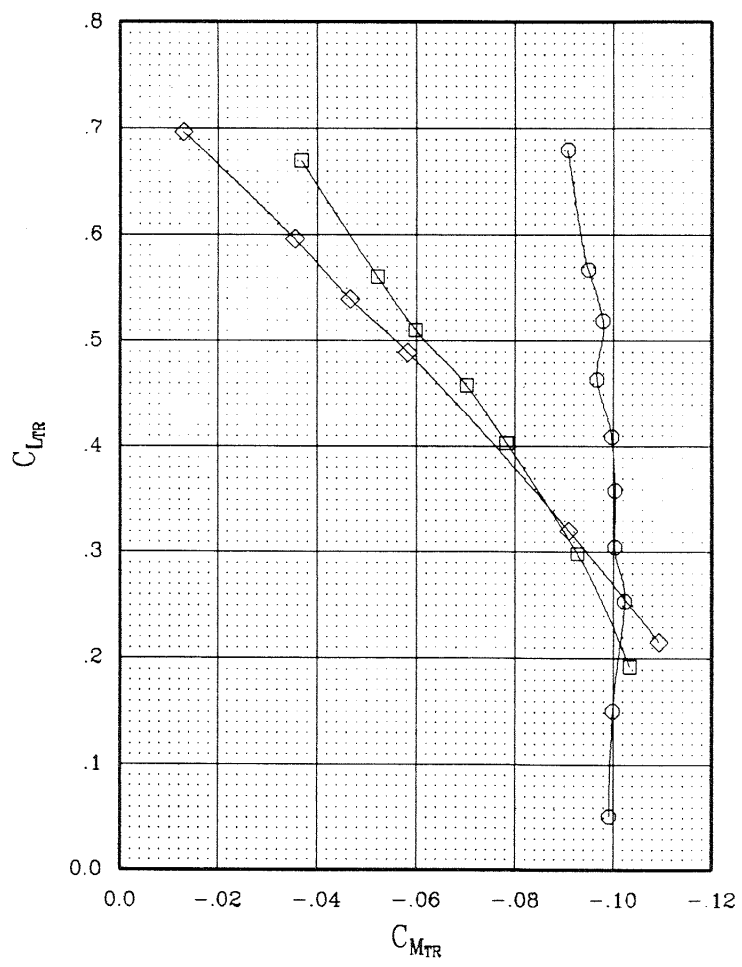
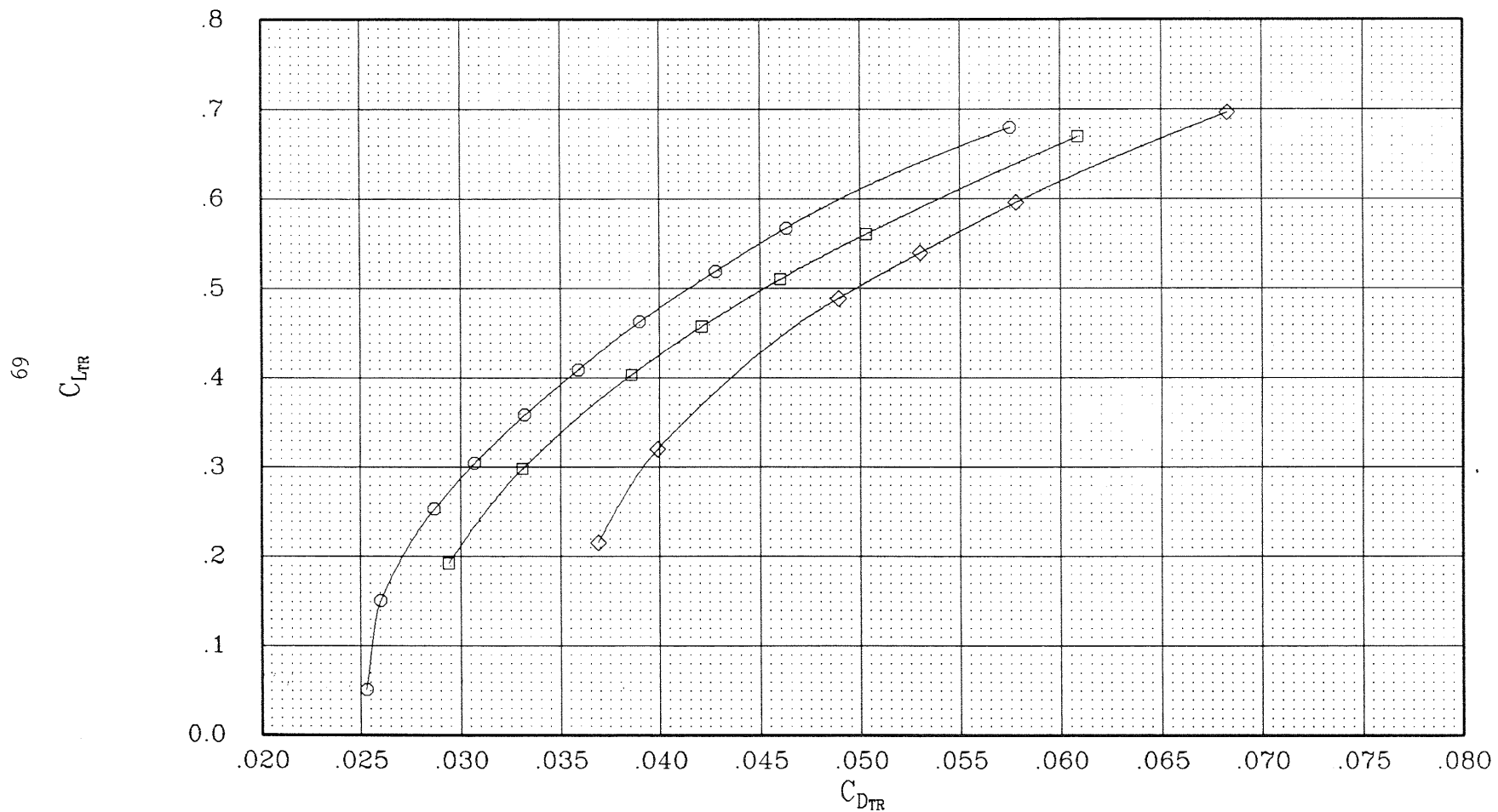
(d)  $M_{\infty} = 0.78$ .

Figure 13.- Continued.

SYMBOL	CONFIGURATION	MACH	BETA	EPR	CTNET
—○—	W B	.784	0.0	1.000	0.0
—□—	W B OTWB L H2	.773	0.0	1.712	0.0
—◇—	W B OTW L H2 P2	.776	56.6	1.712	.028

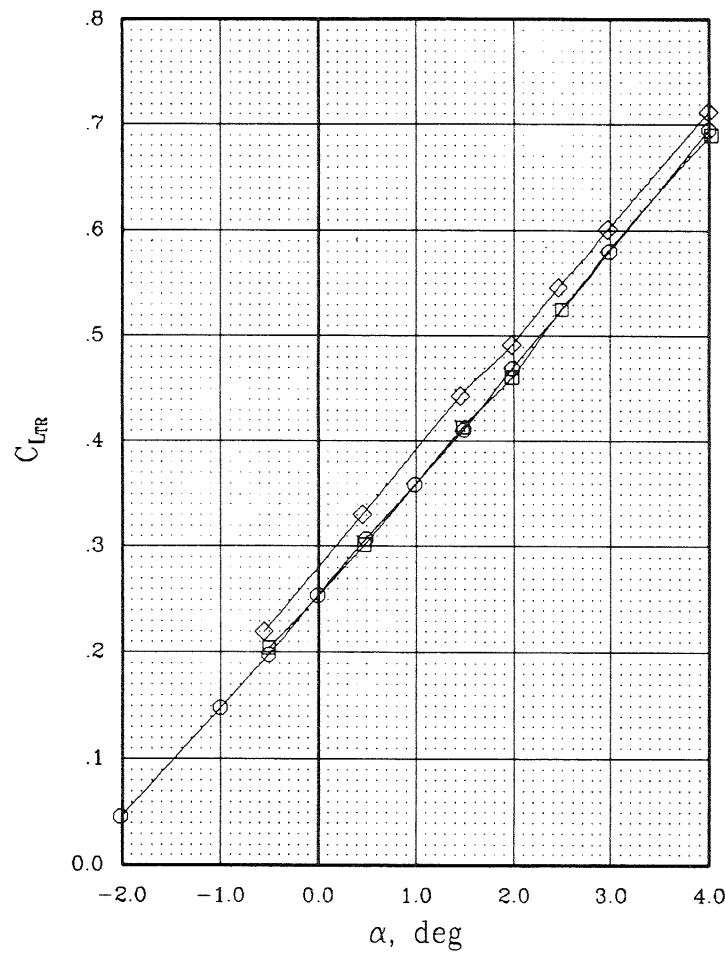


(d)  $M_\infty = 0.78$ .

Figure 13.- Continued.

SYMBOL	CONFIGURATION	MACH	BETA	EPR	CTNET
—○—	W B	.794	0.0	1.000	0.0
—□—	W B OTWB L H2	.794	0.0	1.978	0.0
—◇—	W B OTW L H2 P2	.803	56.6	1.978	.028

70



(e)  $M_{\infty} = 0.80$ .

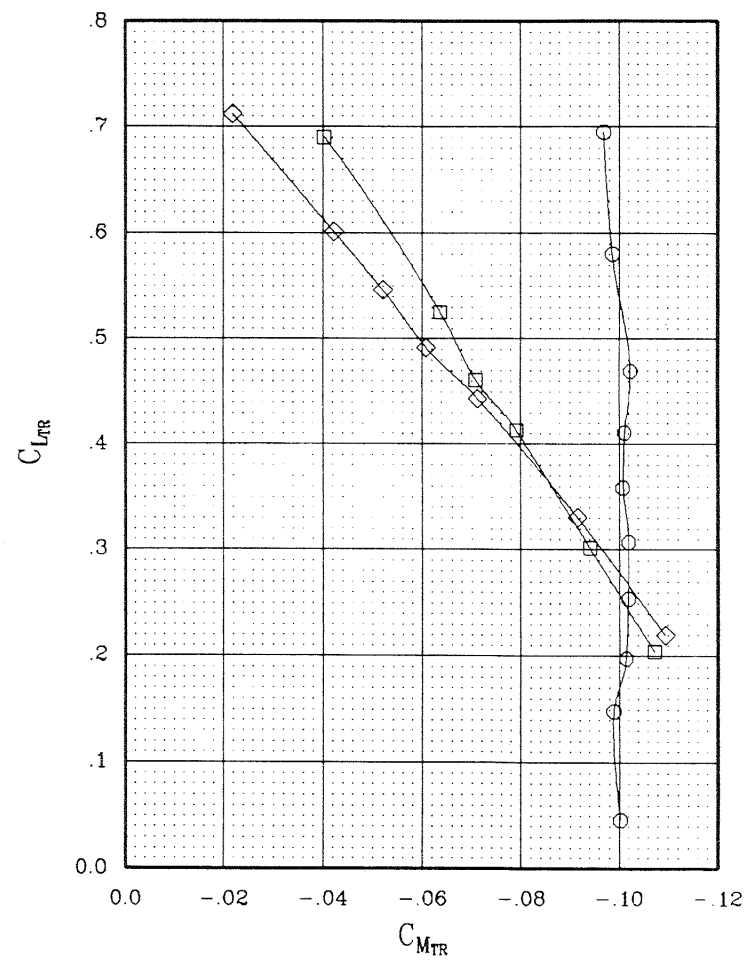
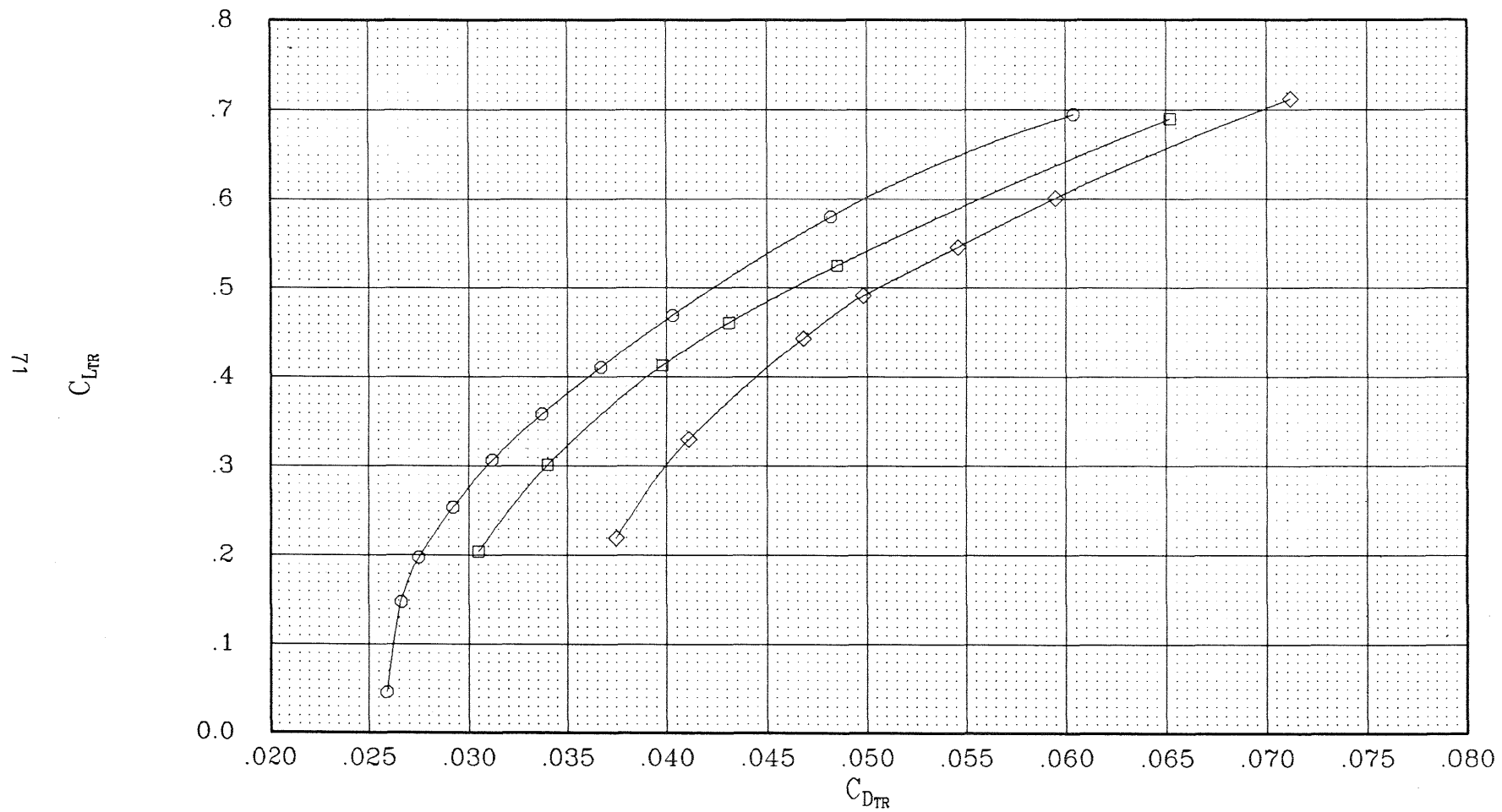


Figure 13.- Continued.

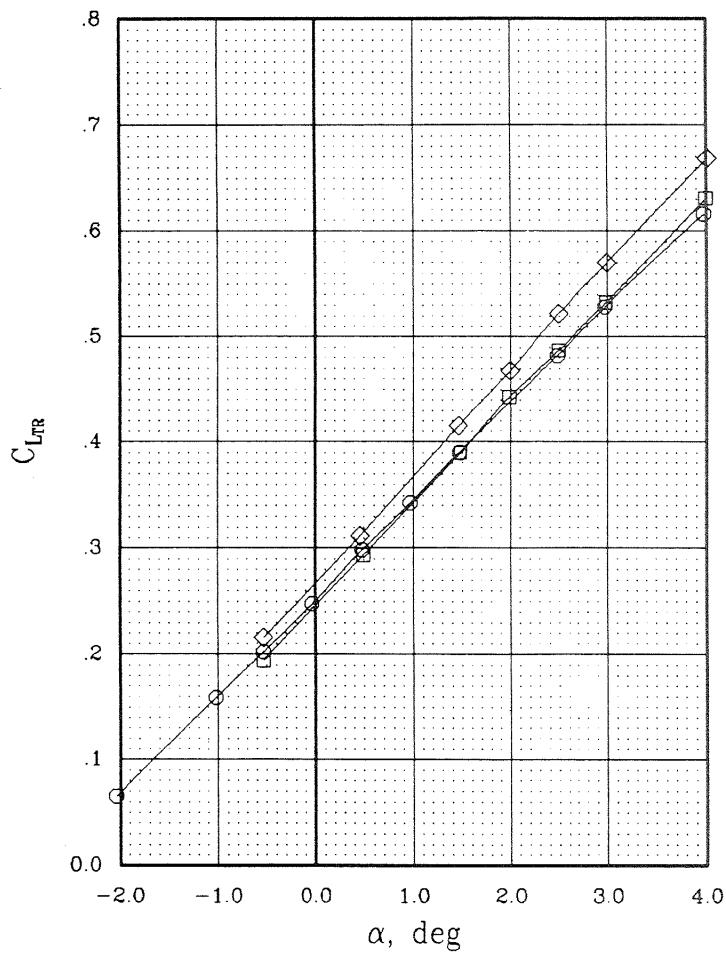
SYMBOL	CONFIGURATION	MACH	BETA	EPR	CTNET
—○—	W B	.794	0.0	1.000	0.0
—□—	W B OTWB L H2	.794	0.0	1.978	0.0
—◇—	W B OTW L H2 P2	.803	56.6	1.978	.028



(e)  $M_{\infty} = 0.80$ .

Figure 13.- Concluded.

SYMBOL	CONFIGURATION	MACH	BETA	EPR	CTNET
—○—	W B	.597	0.0	1.000	0.0
—□—	W B OTWB L H2 E	.586	0.0	1.115	0.0
—◇—	W B OTW L H2 P2 E	.595	54.8	1.115	.025



(a)  $M_a = 0.60$ .

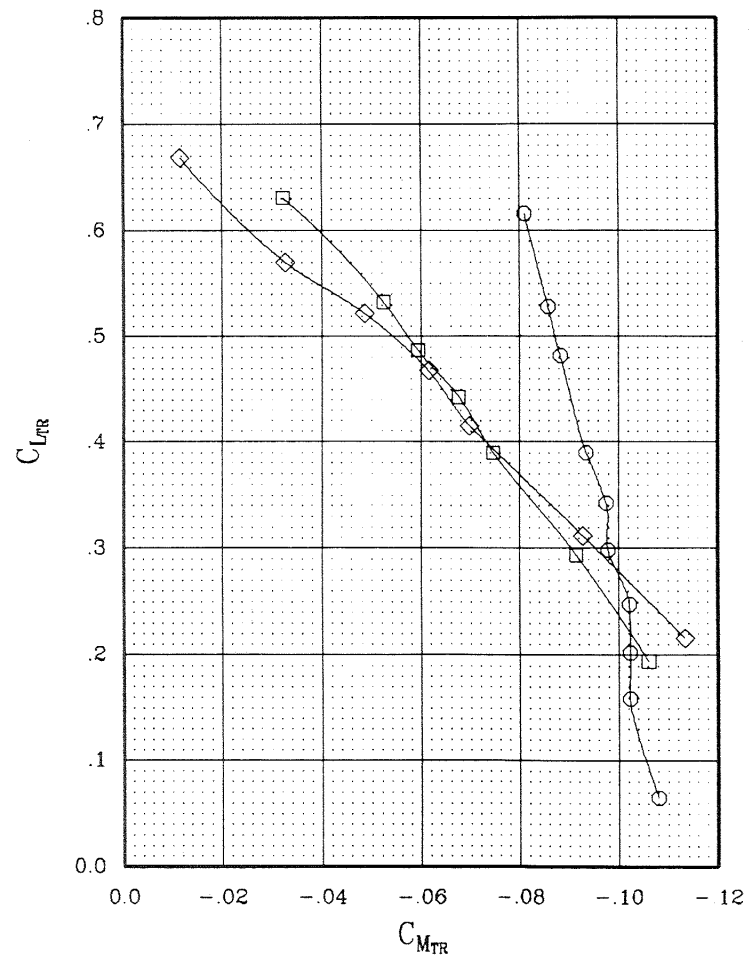
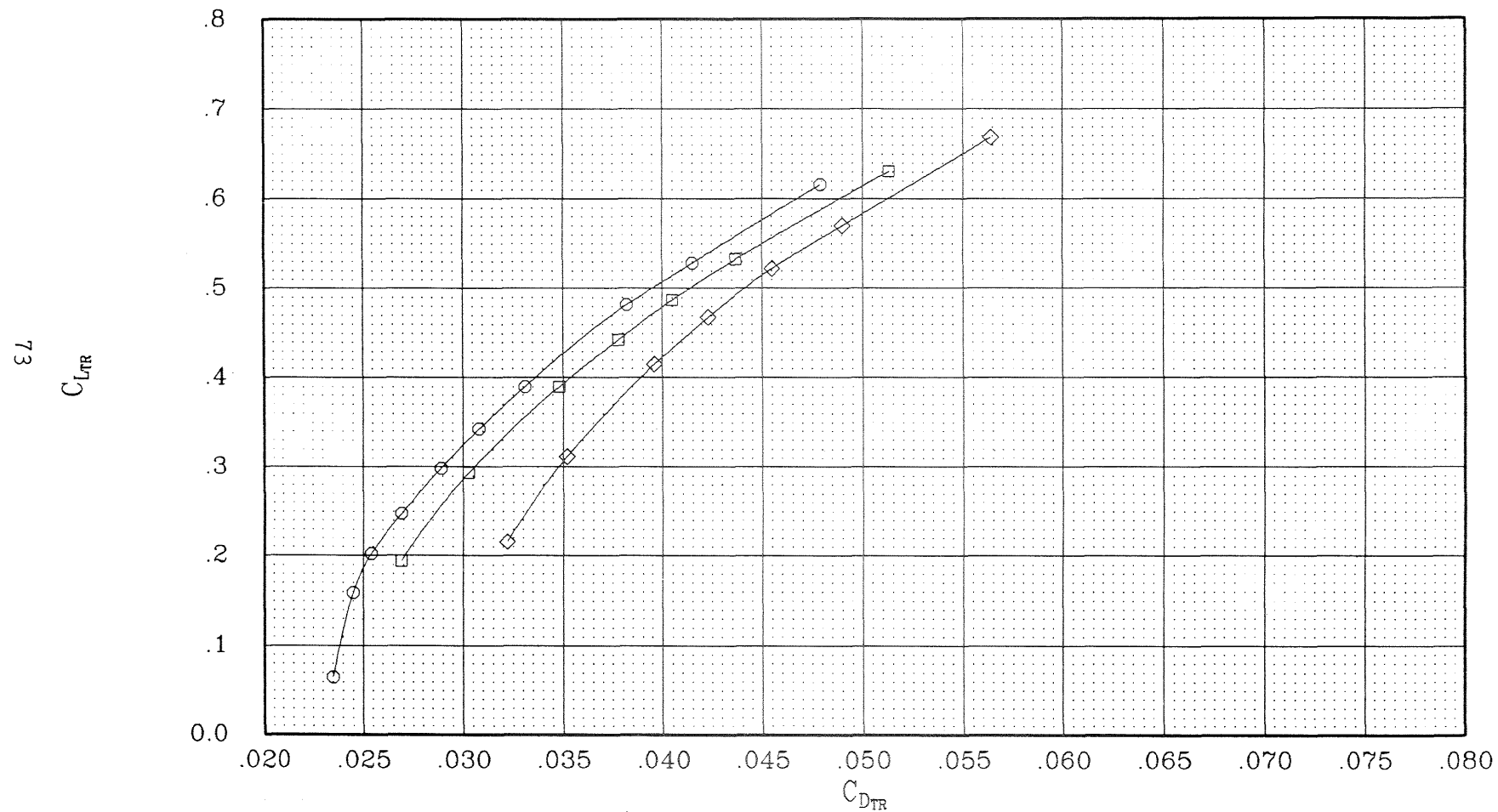


Figure 14.- Extended duct aerodynamic characteristics at cruise power.

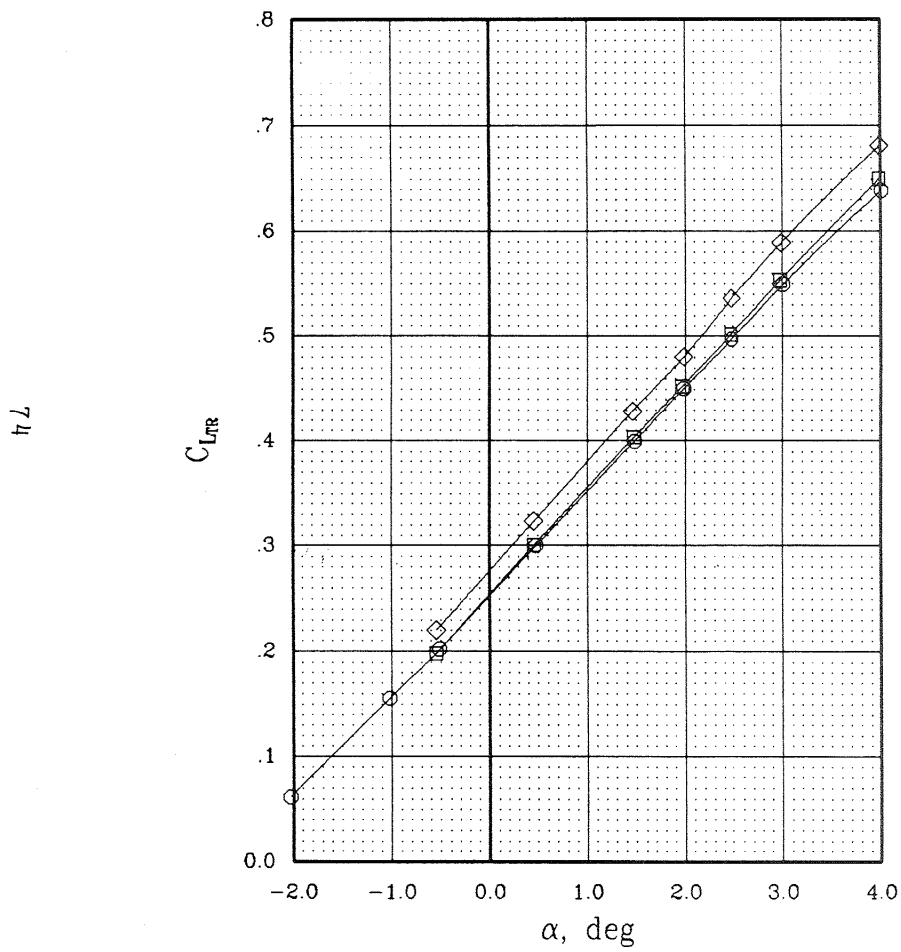
SYMBOL	CONFIGURATION	MACH	BETA	EPR	CTNET
—○—	W B	.597	0.0	1.000	0.0
—□—	W B OTWB L H2 E	.586	0.0	1.115	0.0
—◇—	W B OTW L H2 P2 E	.595	54.8	1.115	.025



(a)  $M_\infty = 0.60$ .

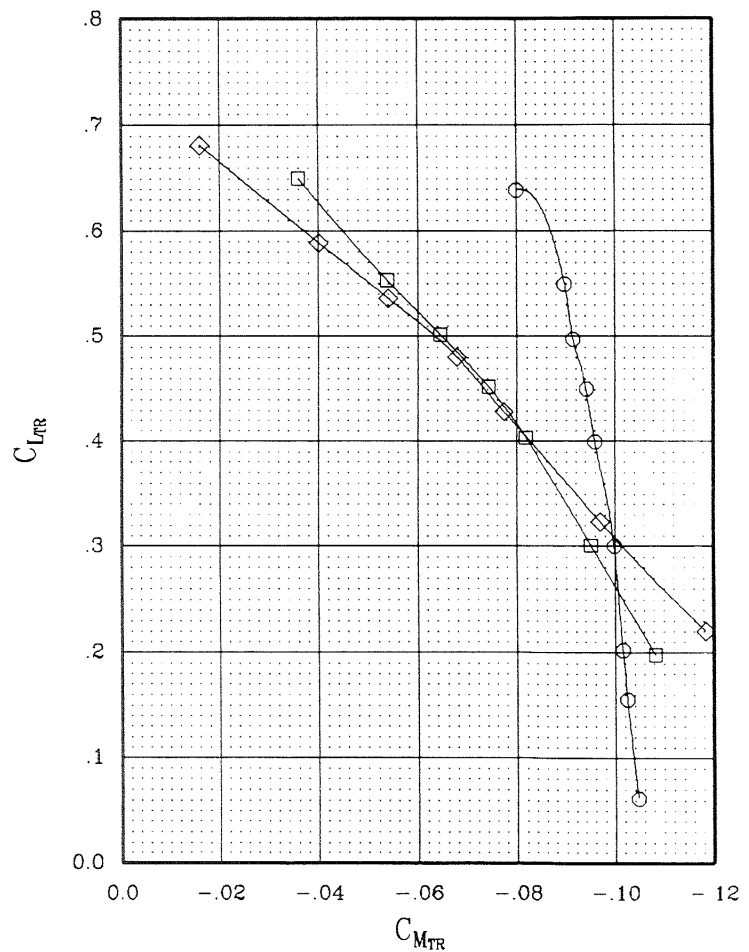
Figure 14.- Continued.

SYMBOL	CONFIGURATION	MACH	BETA	EPR	CTNET
—○—	W B	.699	0.0	1.000	0.0
—□—	W B OTWB L H2 E	.706	0.0	1.235	0.0
—◇—	W B OTW L H2 P2 E	.703	55.6	1.235	.026

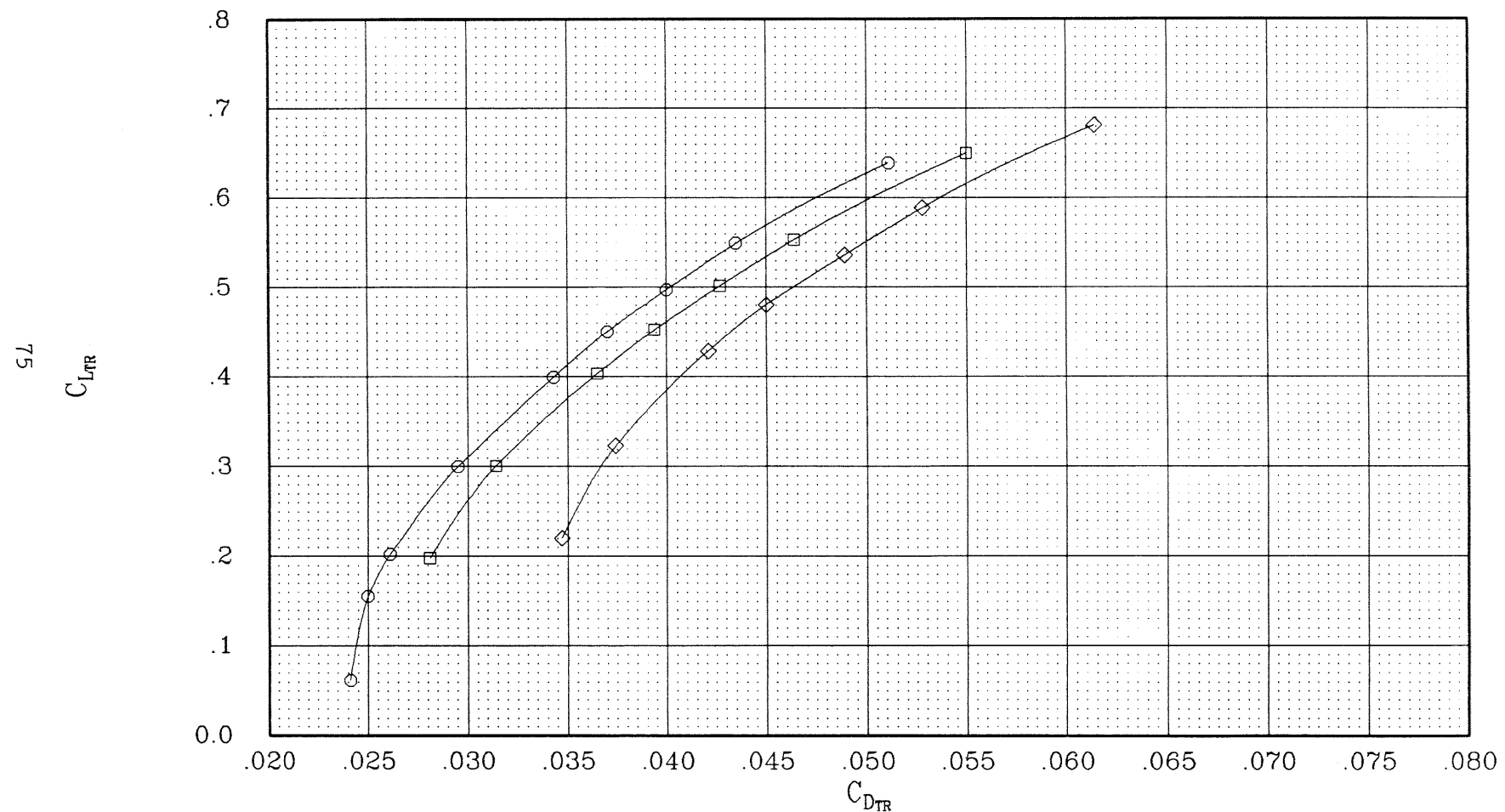


(b)  $M_{\infty} = 0.70$ .

Figure 14.- Continued.



SYMBOL	CONFIGURATION	MACH	BETA	EPR	CTNET
—○—	W B	.699	0.0	1.000	0.0
—□—	W B OTWB L H2 E	.706	0.0	1.235	0.0
—◇—	W B OTW L H2 P2 E	.703	55.6	1.235	.026

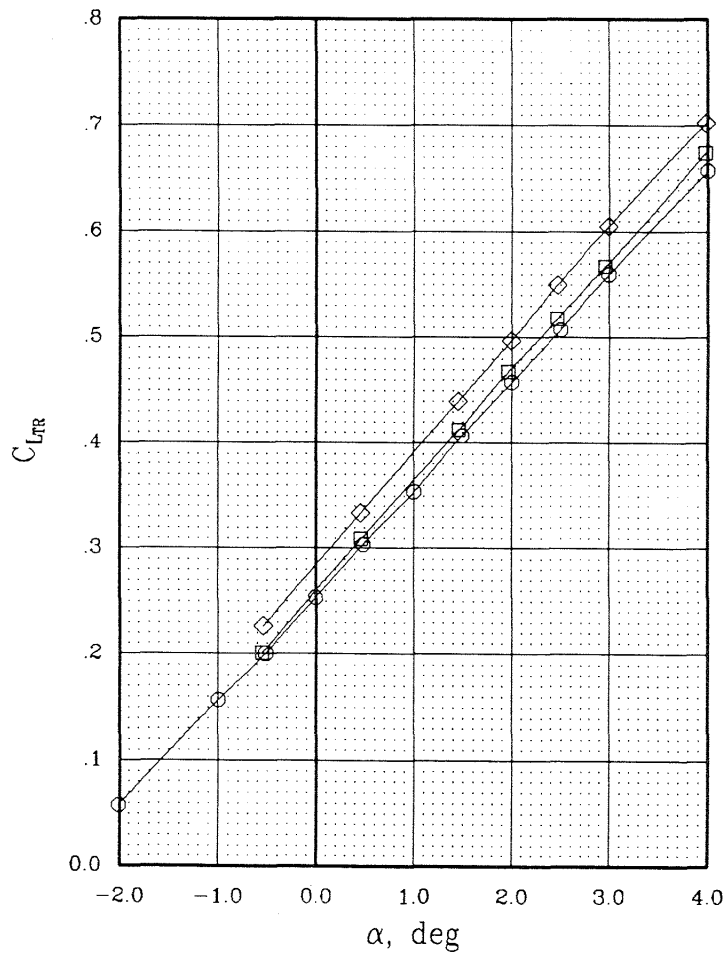


(b)  $M_\infty = 0.70$ .

Figure 14.- Continued.

SYMBOL	CONFIGURATION	MACH	BETA	EPR	CTNET
—○—	W B	.749	0.0	1.000	0.0
—□—	W B OTWB L H2 E	.750	0.0	1.549	0.0
—◇—	W B OTW L H2 P2 E	.748	56.6	1.549	.028

76



(c)  $M_{\infty} = 0.75$ .

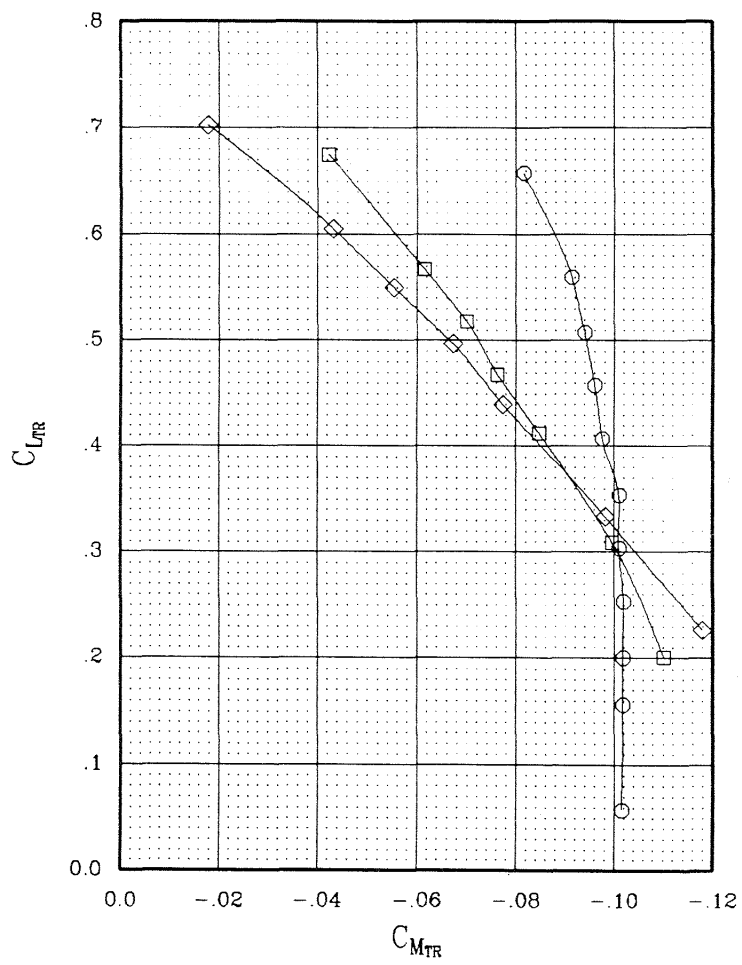
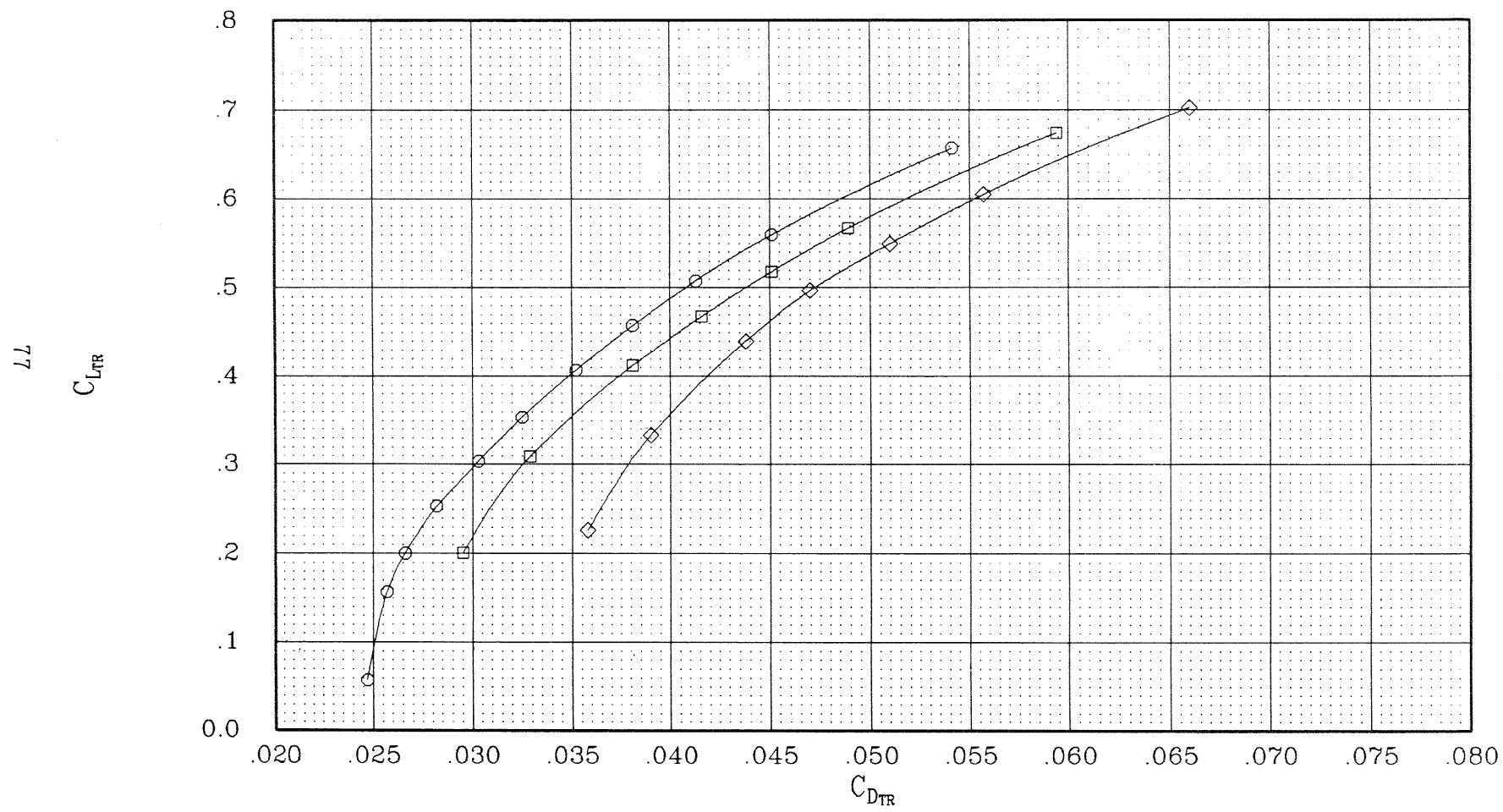


Figure 14.- Continued.

SYMBOL	CONFIGURATION	MACH	BETA	EPR	CTNET
—○—	W B	.749	0.0	1.000	0.0
—□—	W B OTWB L H2 E	.750	0.0	1.549	0.0
—◇—	W B OTW L H2 P2 E	.748	56.6	1.549	.028

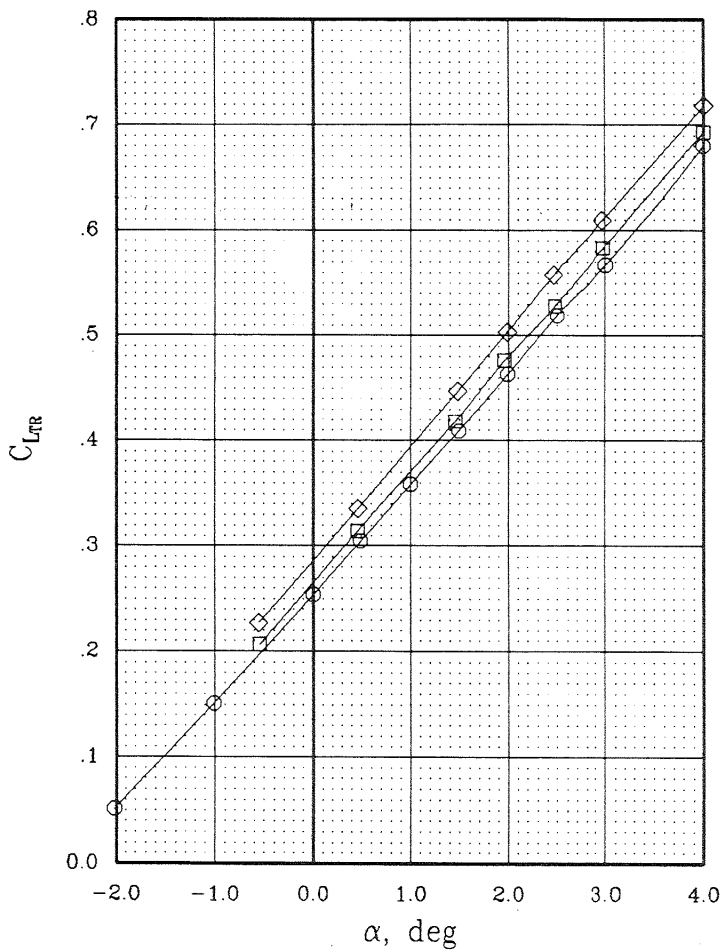


(c)  $M_{\infty} = 0.75$ .

Figure 14.- Continued.

SYMBOL	CONFIGURATION	MACH	BETA	EPR	CTNET
—○—	W B	.784	0.0	1.000	0.0
—□—	W B OTWB L H2 E	.772	0.0	1.739	0.0
—◇—	W B OTW L H2 P2 E	.783	56.6	1.739	.028

78



(d)  $M_{\infty} = 0.78$ .

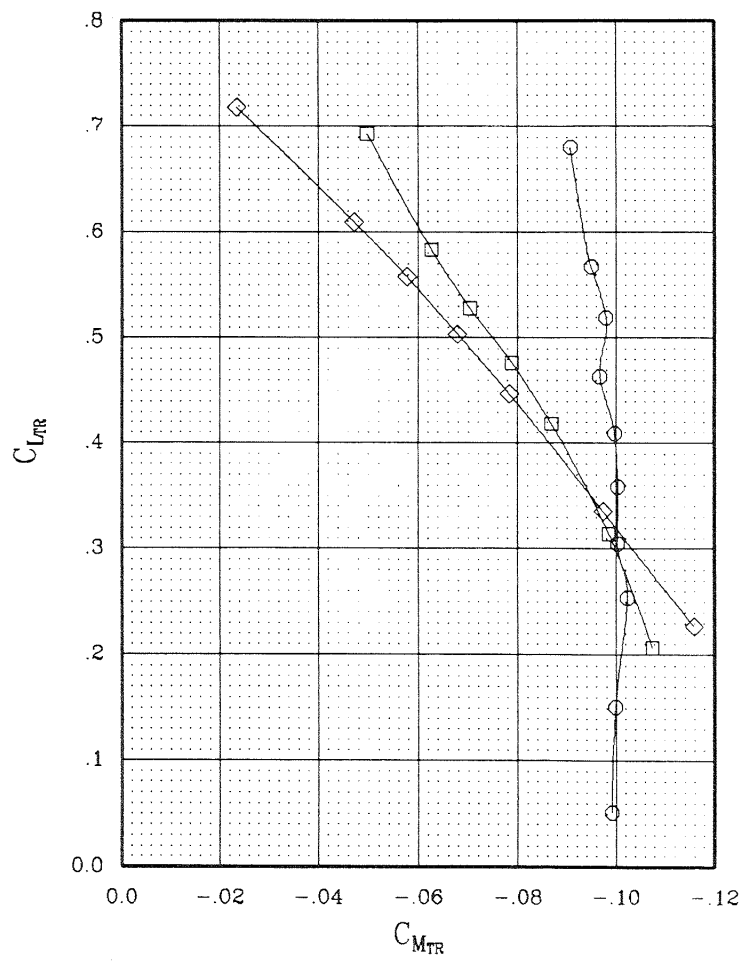
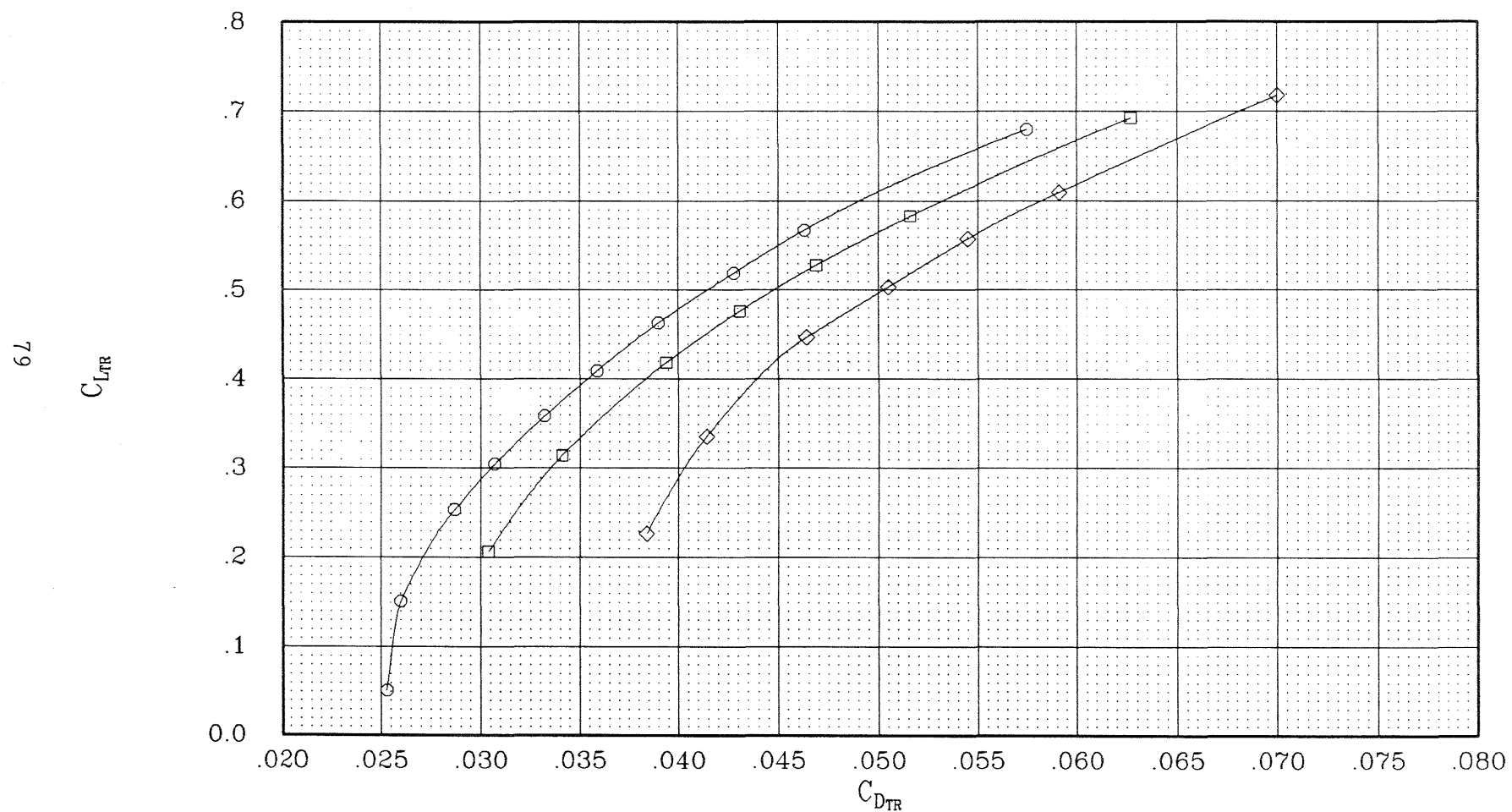


Figure 14.- Continued.

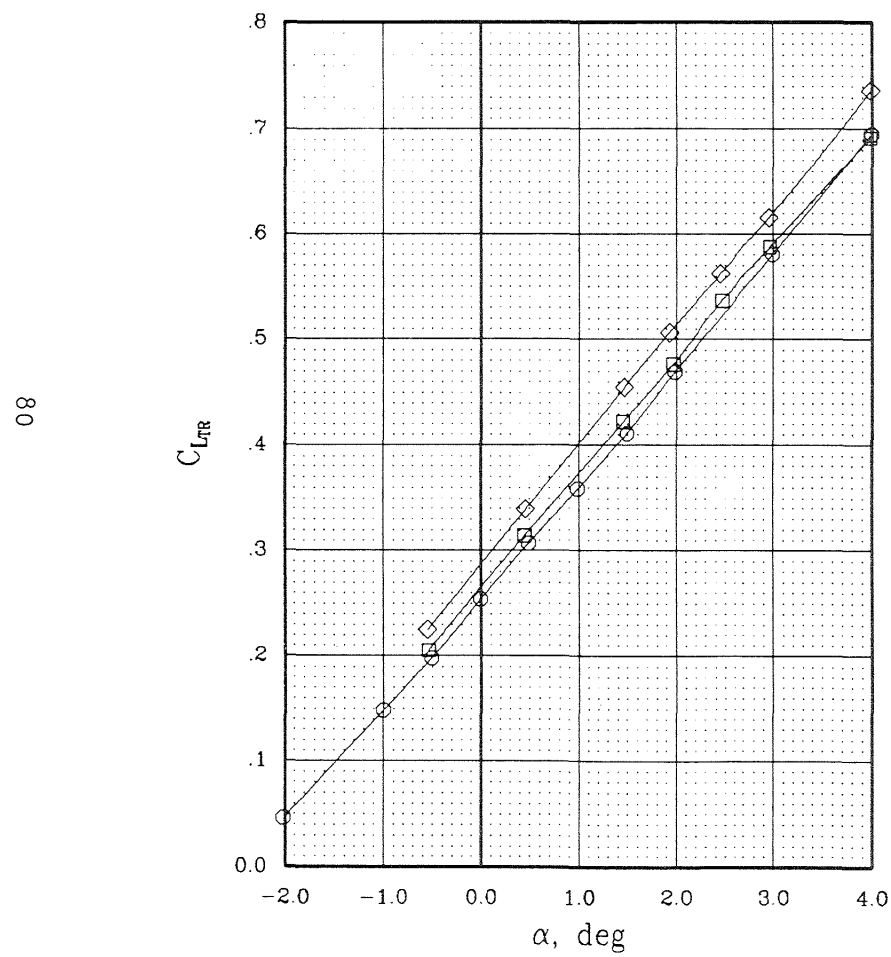
SYMBOL	CONFIGURATION	MACH	BETA	EPR	CTNET
○	W B	.784	0.0	1.000	0.0
□	W B OTWB L H2 E	.772	0.0	1.739	0.0
◇	W B OTW L H2 P2 E	.783	58.6	1.739	.028



(d)  $M_{\infty} = 0.78$ .

Figure 14.- Continued.

SYMBOL	CONFIGURATION	MACH	BETA	EPR	CTNET
—○—	W B	.794	0.0	1.000	0.0
—□—	W B OTWB L H2 E	.797	0.0	1.906	0.0
—◇—	W B OTW L H2 P2 E	.803	56.6	1.906	.028



(e)  $M_\infty = 0.80$ .

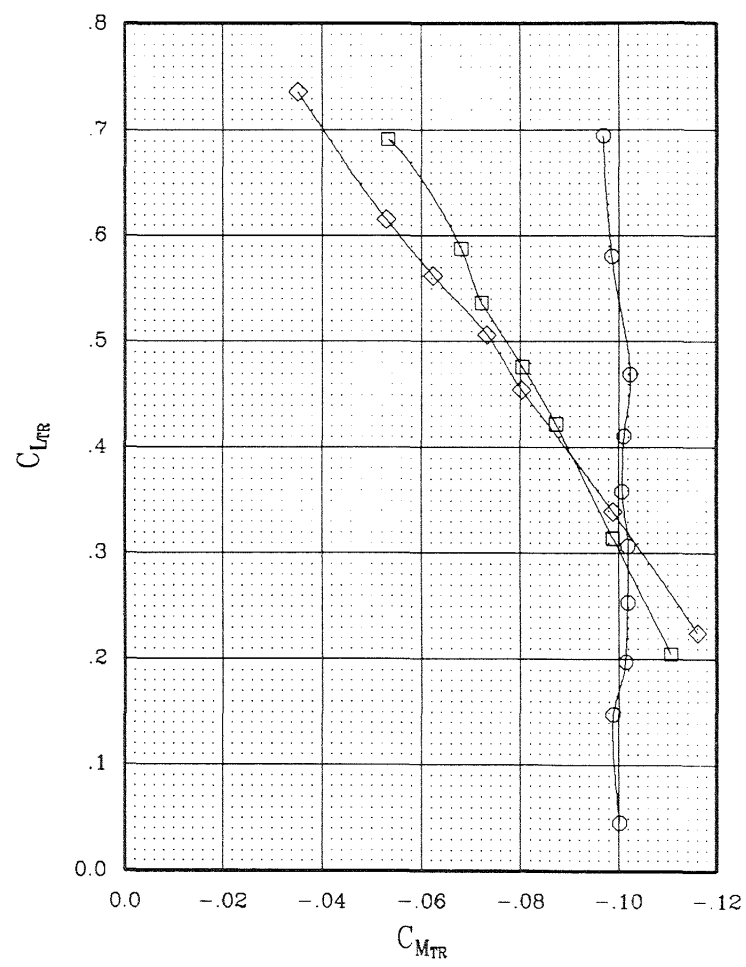
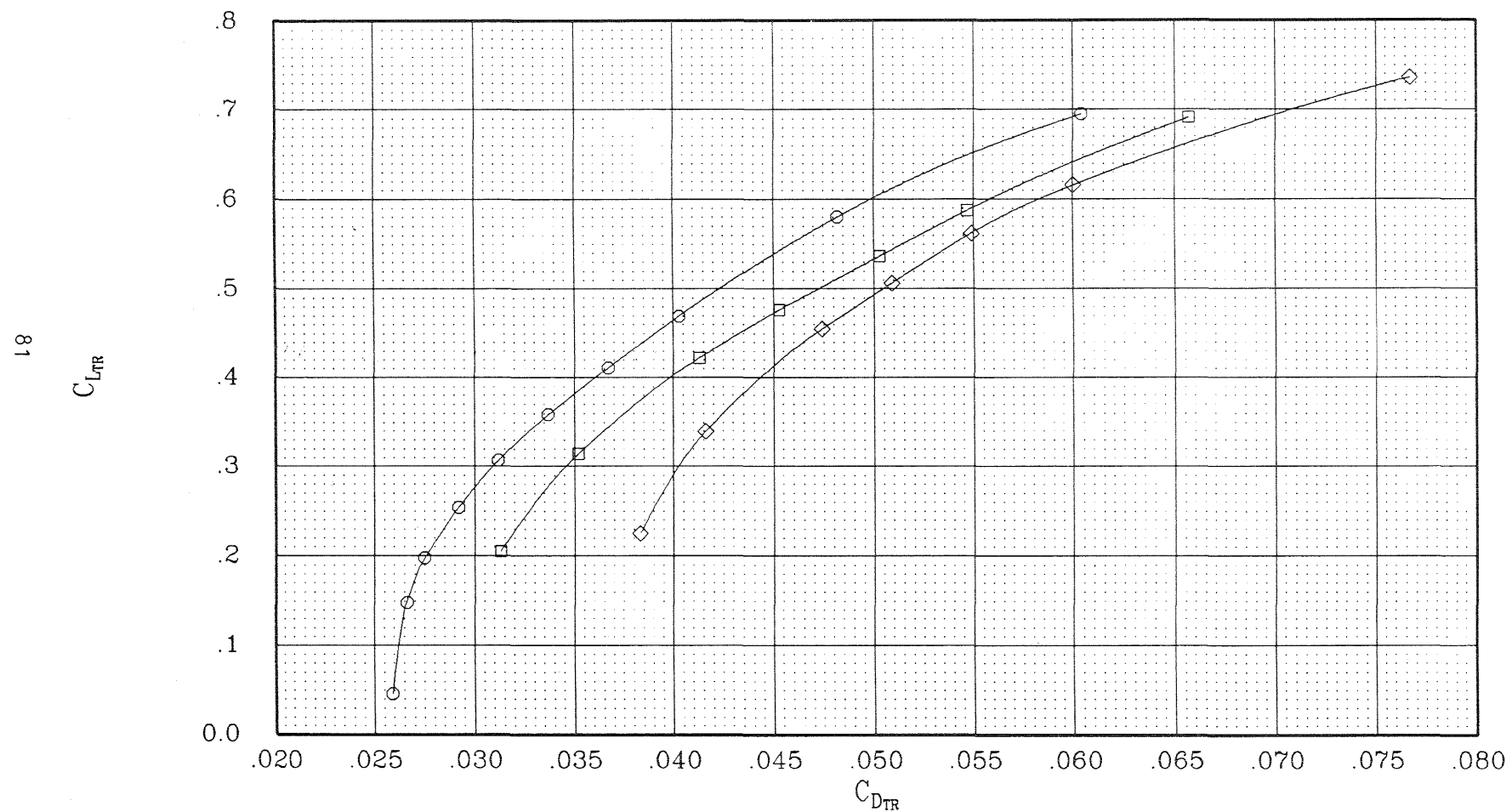


Figure 14.- Continued.

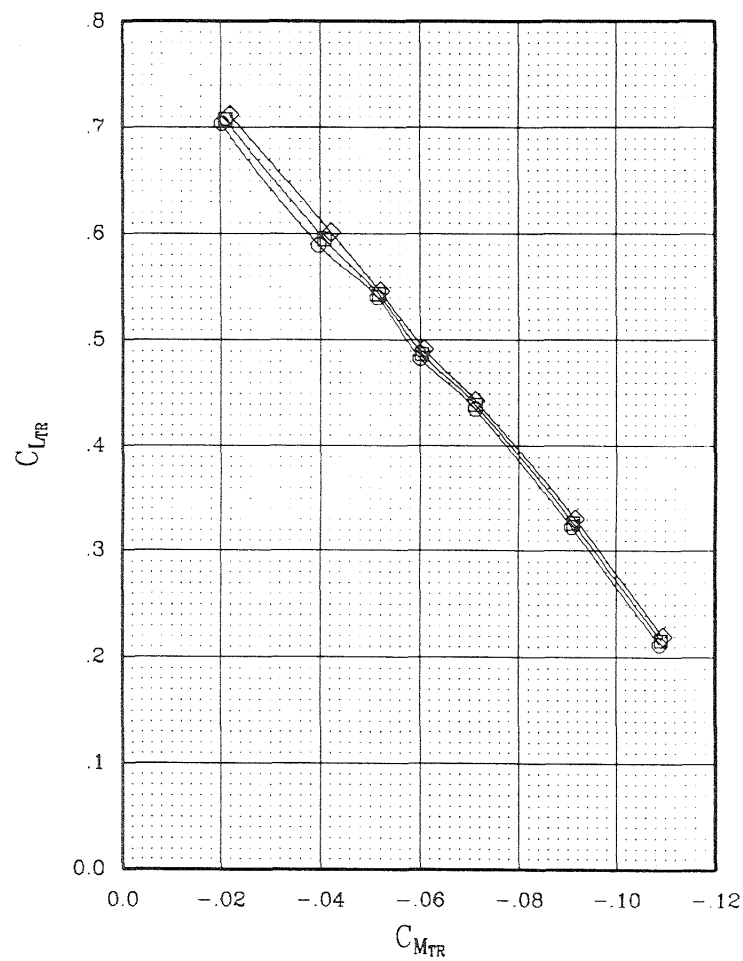
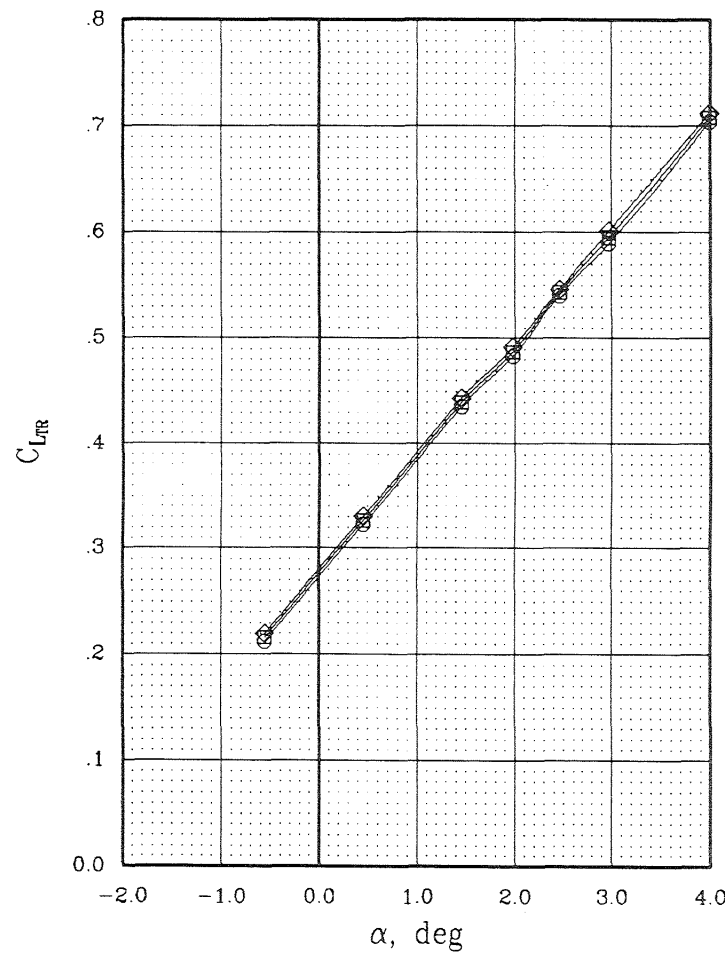
SYMBOL	CONFIGURATION	MACH	BETA	EPR	CTNET
—○—	W B	.794	0.0	1.000	0.0
—□—	W B OTWB L H2 E	.797	0.0	1.906	0.0
—◇—	W B OTW L H2 P2 E	.803	56.6	1.906	.028



(e)  $M_{\infty} = 0.80.$

Figure 14.- Concluded.

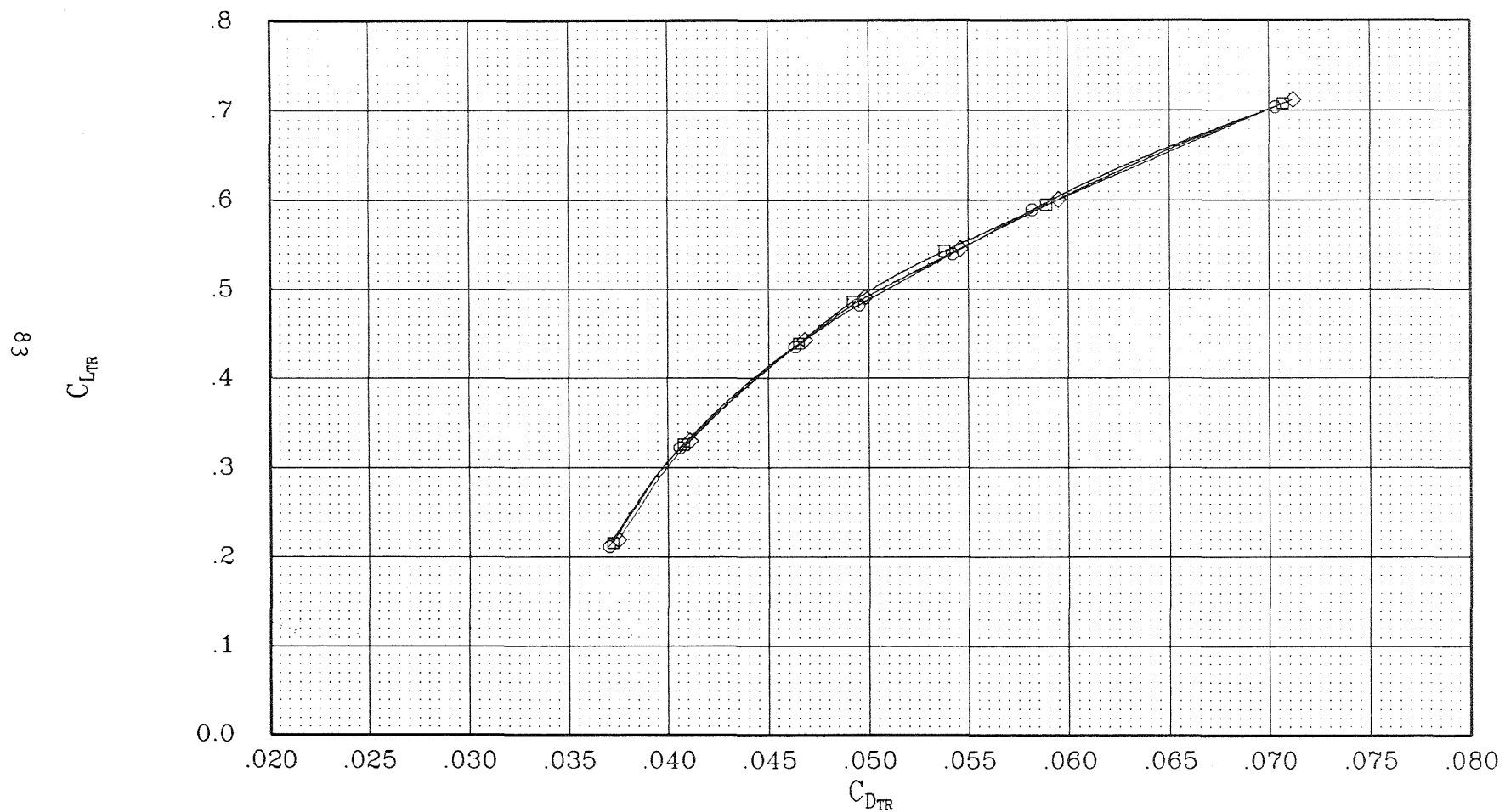
SYMBOL	CONFIGURATION	MACH	BETA	EPR	CTNET
—○—	W B OTW L H2 P2	.803	56.6	1.832	.026
—□—	W B OTW L H2 P2	.803	56.6	1.905	.027
—◇—	W B OTW L H2 P2	.803	56.6	1.978	.028



(a) Baseline configuration.

Figure 15.- Effect of thrust on the aerodynamic characteristics.

SYMBOL	CONFIGURATION	MACH	BETA	EPR	CTNET
—○—	W B OTW L H2 P2	.803	56.6	1.832	.026
—□—	W B OTW L H2 P2	.803	56.6	1.905	.027
—◇—	W B OTW L H2 P2	.803	56.6	1.978	.028

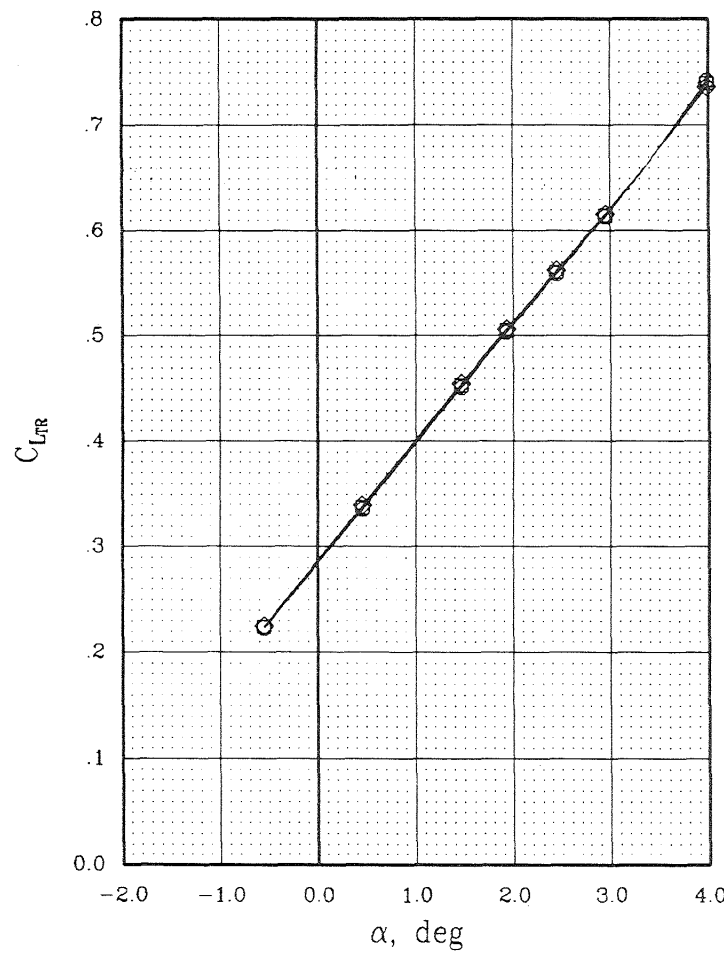


(a) Concluded.

Figure 15.- Continued.

SYMBOL	CONFIGURATION	MACH	BETA	EPR	CTNET
—○—	W B OTW L H2 P2 E	.803	56.6	1.809	.026
—□—	W B OTW L H2 P2 E	.803	56.6	1.857	.027
—◇—	W B OTW L H2 P2 E	.803	56.6	1.906	.028

118



(b) Extended duct configuration.

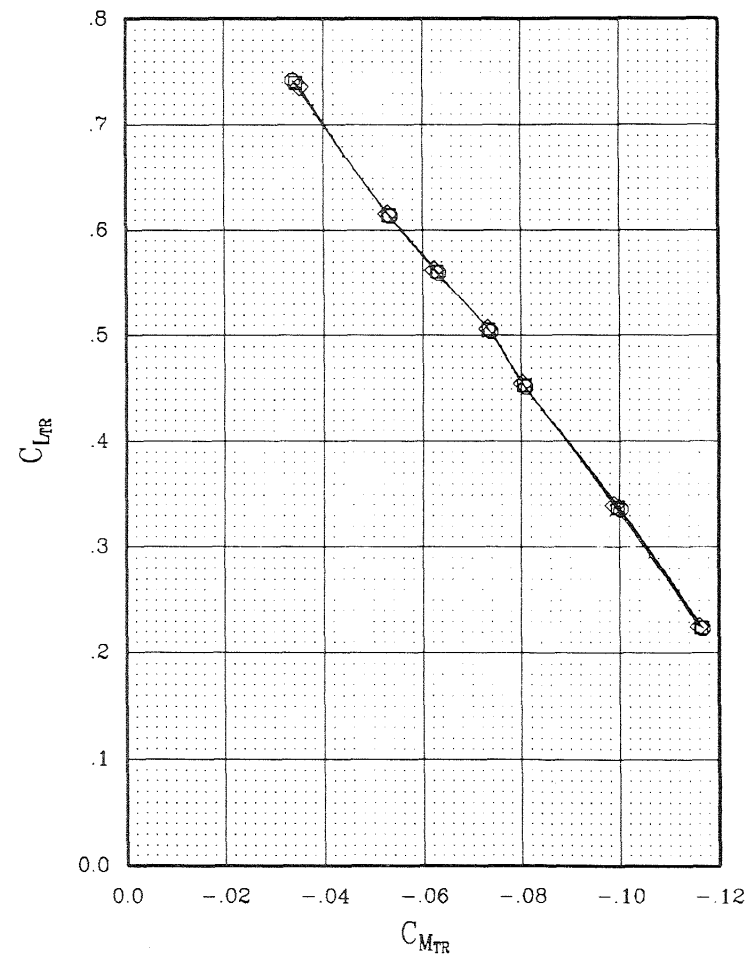
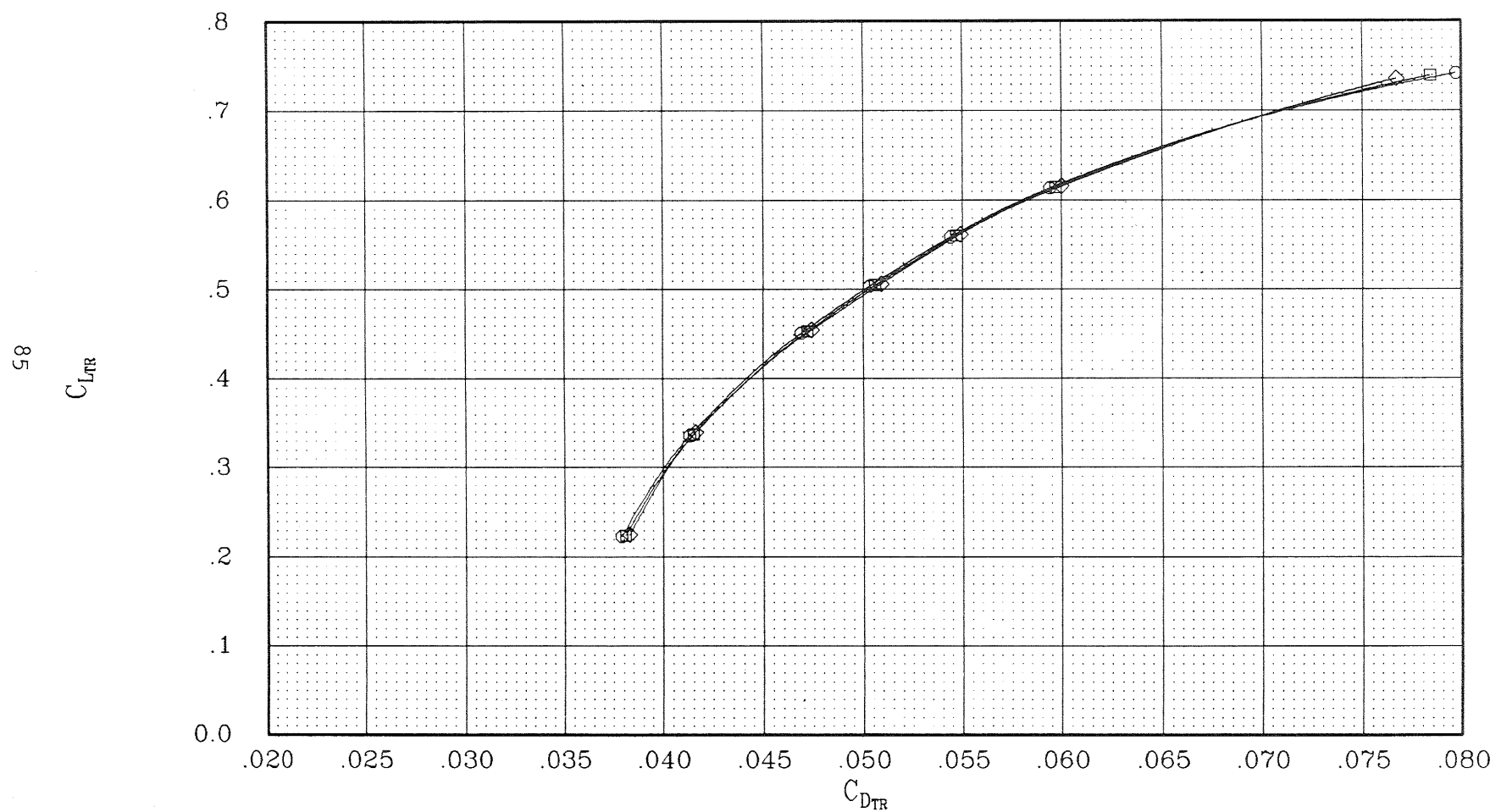


Figure 15.- Continued.

SYMBOL	CONFIGURATION	MACH	BETA	EPR	CTNET
—○—	W B OTW L H2 P2 E	.803	56.6	1.809	.026
—□—	W B OTW L H2 P2 E	.803	56.6	1.857	.027
—◇—	W B OTW L H2 P2 E	.803	56.6	1.906	.028



(b) Concluded.

Figure 15.- Concluded.

SYMBOL	CONFIGURATION	MACH	BETA	EPR	CTNET
—○—	W B	.794	0.0	1.000	0.0
—□—	W B OTW L H2 P2	.803	56.6	1.978	.028
—◇—	W B OTW L H2 P2 E	.803	56.6	1.908	.028

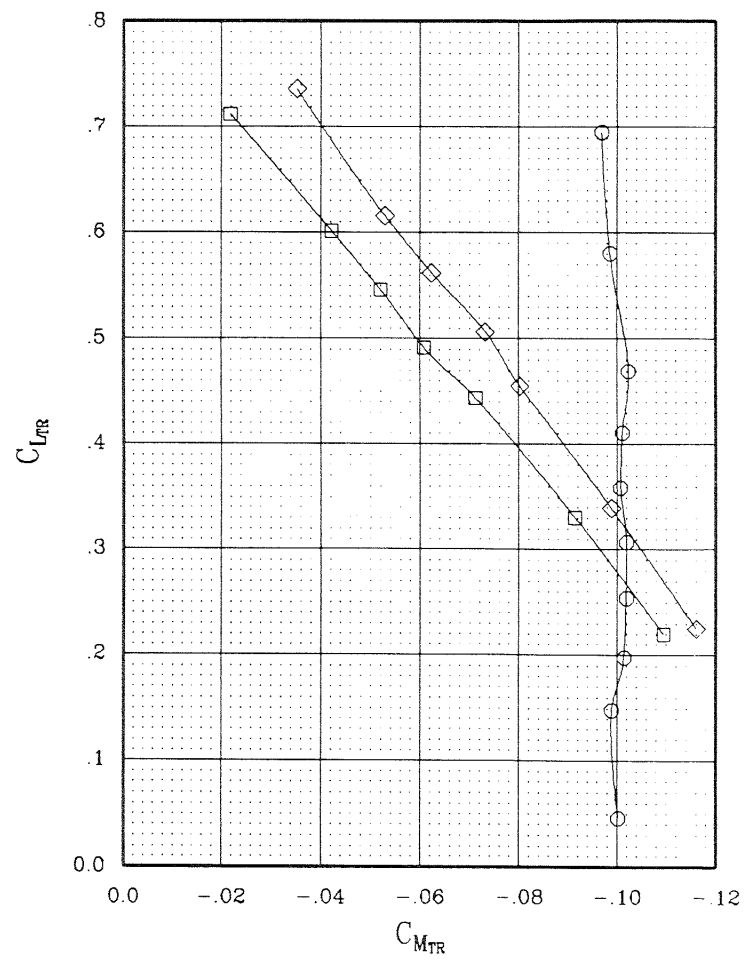
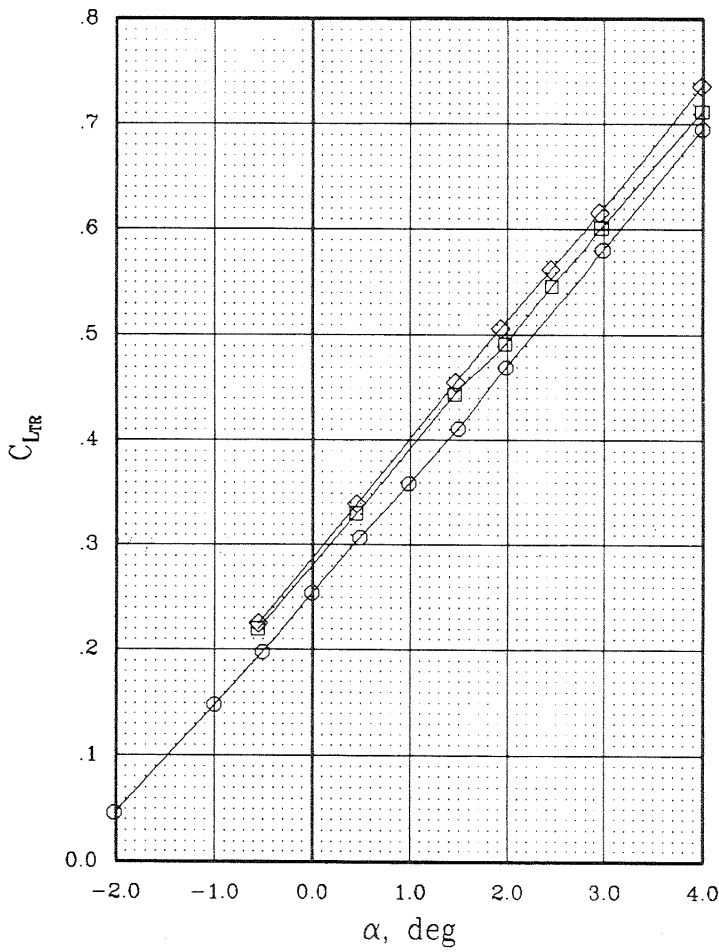


Figure 16.- Configuration comparison at constant thrust.

SYMBOL	CONFIGURATION	MACH	BETA	EPR	CTNET
—○—	W B	.794	0.0	1.000	0.0
—□—	W B OTW L H2 P2	.803	56.6	1.978	.028
—◇—	W B OTW L H2 P2 E	.803	56.6	1.906	.028

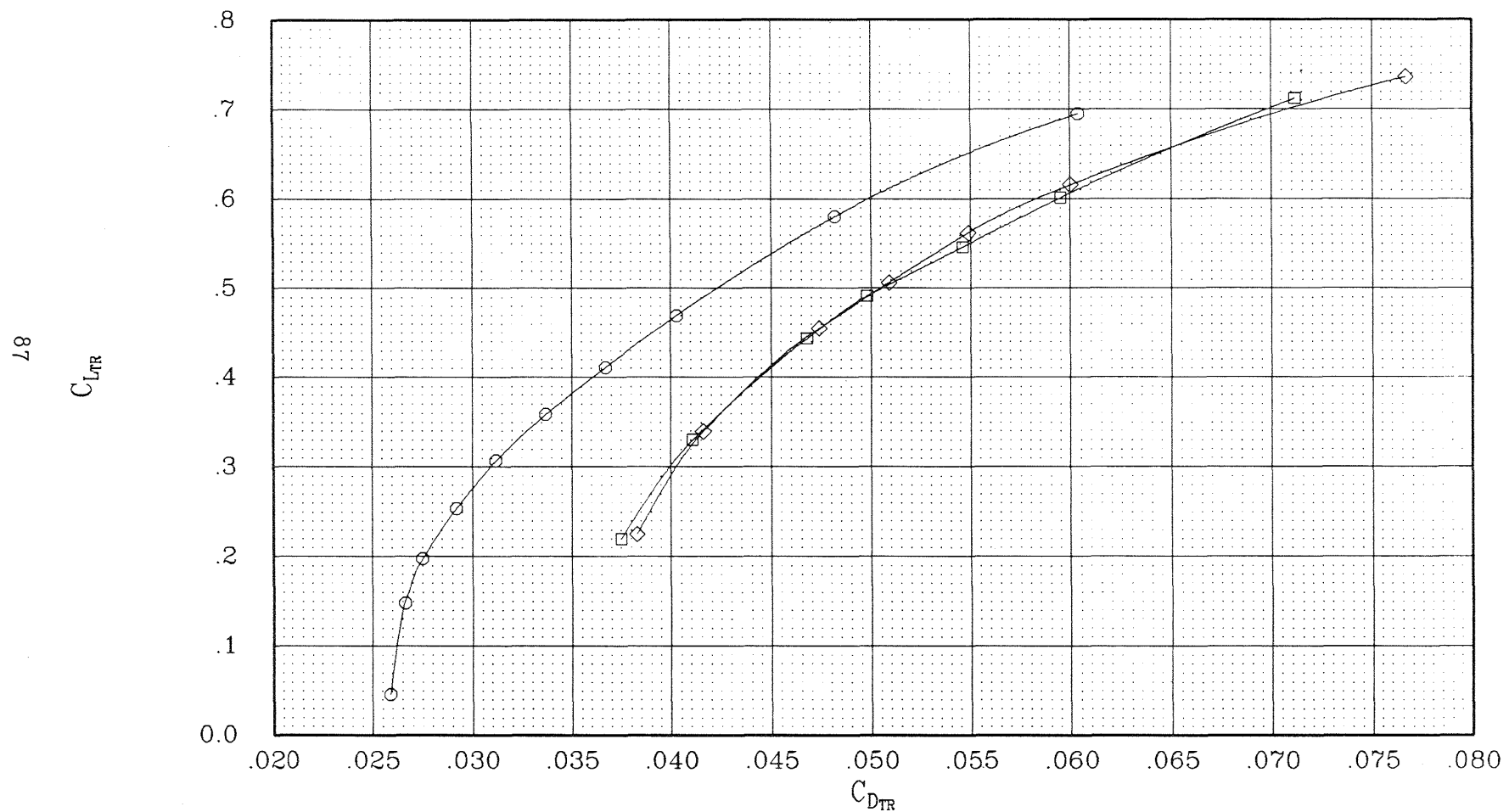
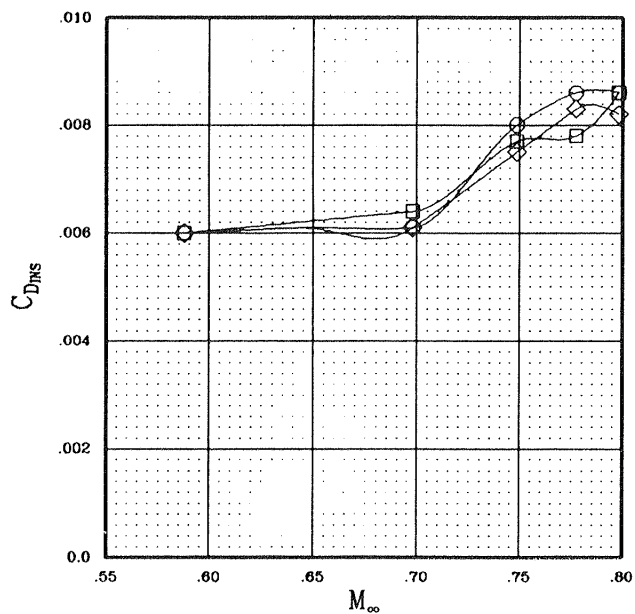
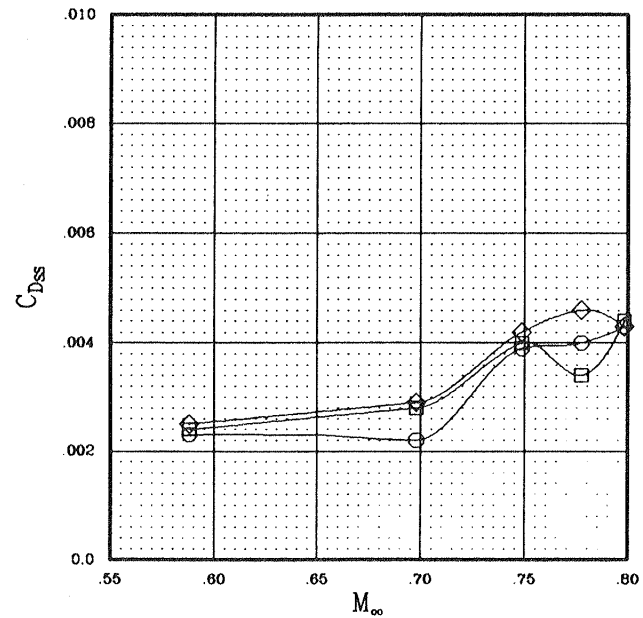
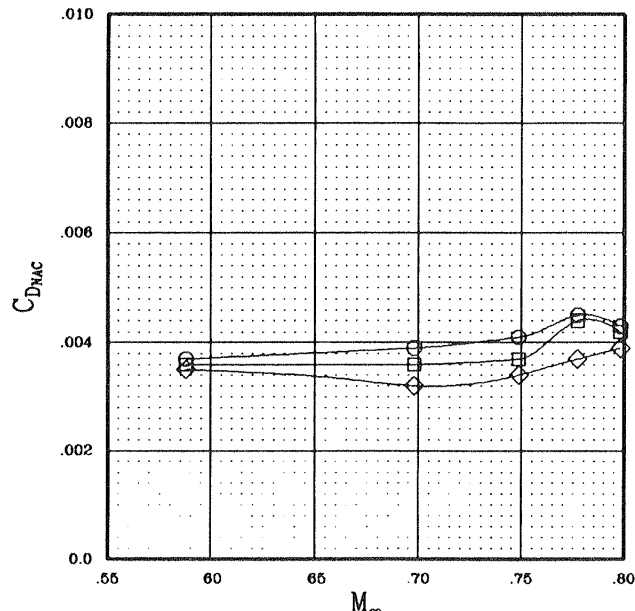


Figure 16.- Concluded.

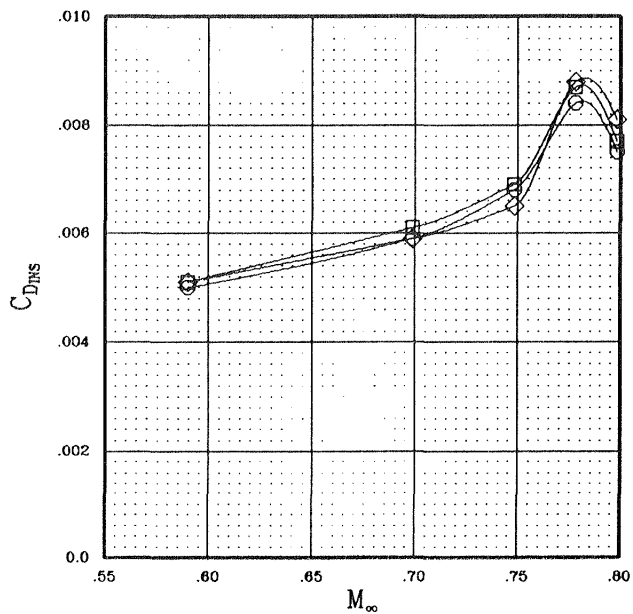
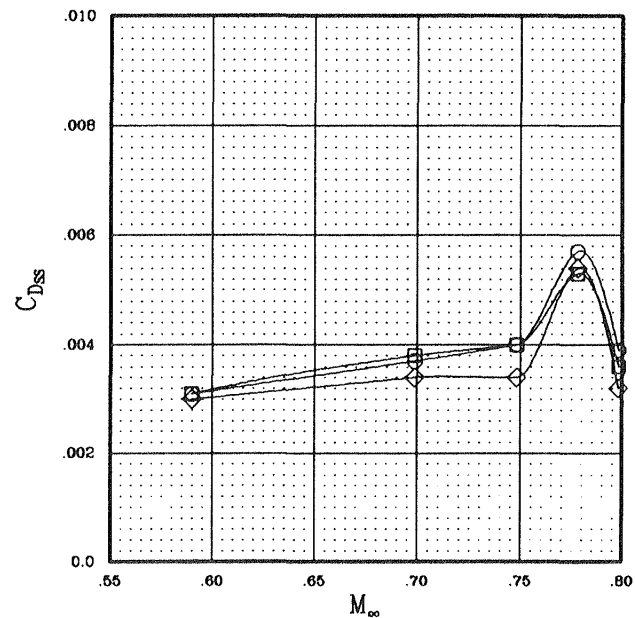
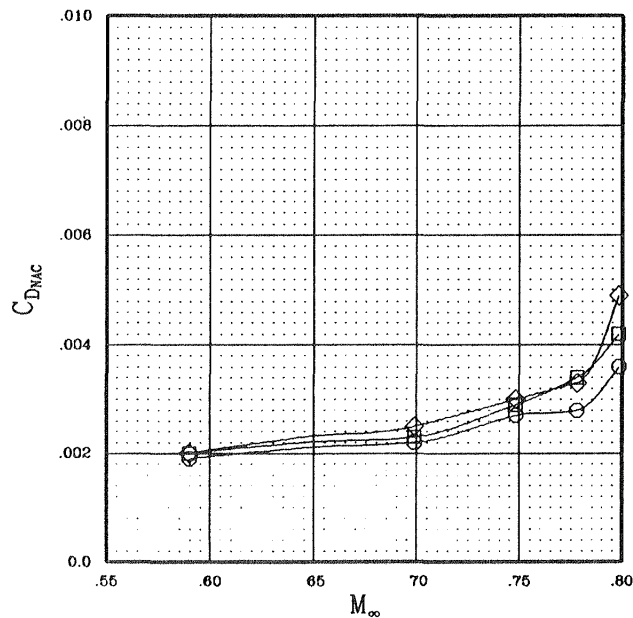
SYMBOL	CONFIGURATION	CTNET	CLEFF
○	W B OTW L H2 P2	.024	.500
□	W B OTW L H2 P2	.026	.500
◇	W B OTW L H2 P2	.028	.500



(a) Baseline configuration.

Figure 17.- Effect of thrust on the installation drags.

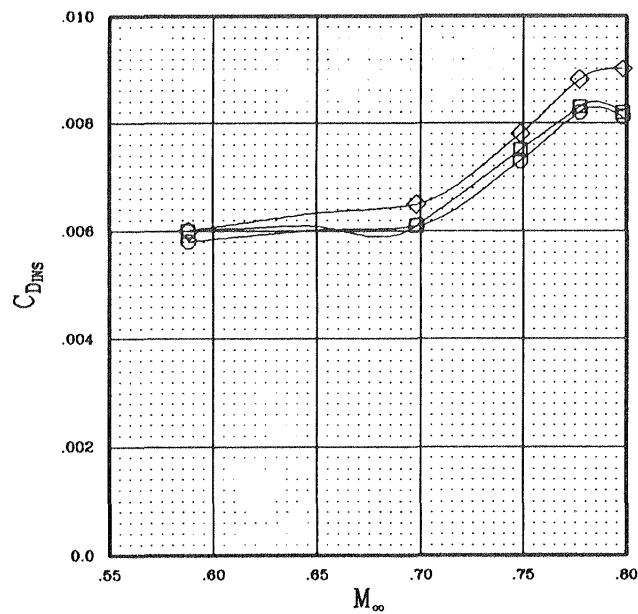
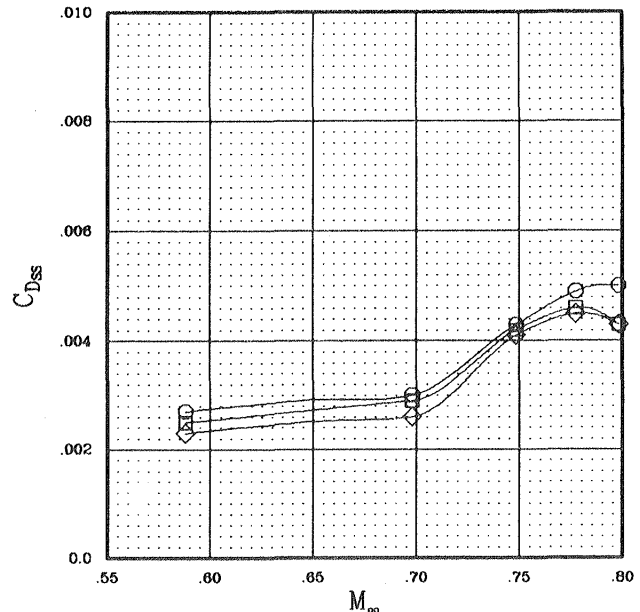
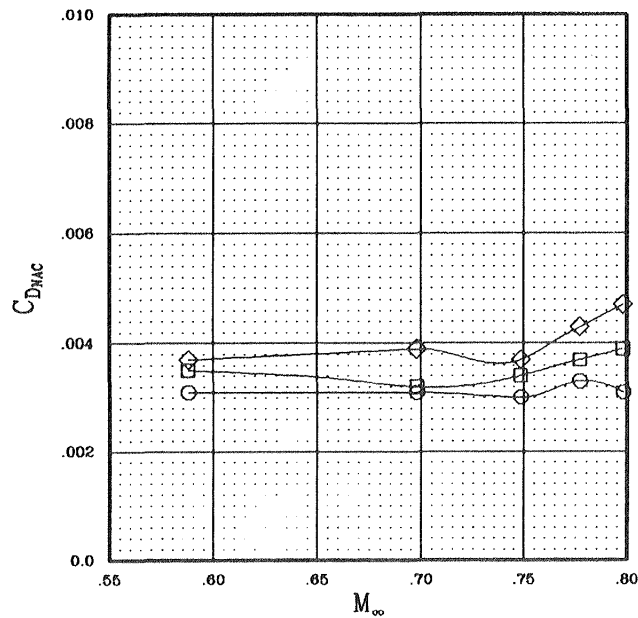
SYMBOL	CONFIGURATION	CTNET	CLEFF
○	W B OTW L H2 P2 E	.024	.500
□	W B OTW L H2 P2 E	.026	.500
◇	W B OTW L H2 P2 E	.028	.500



(b) Extended duct configuration.

Figure 17.- Concluded.

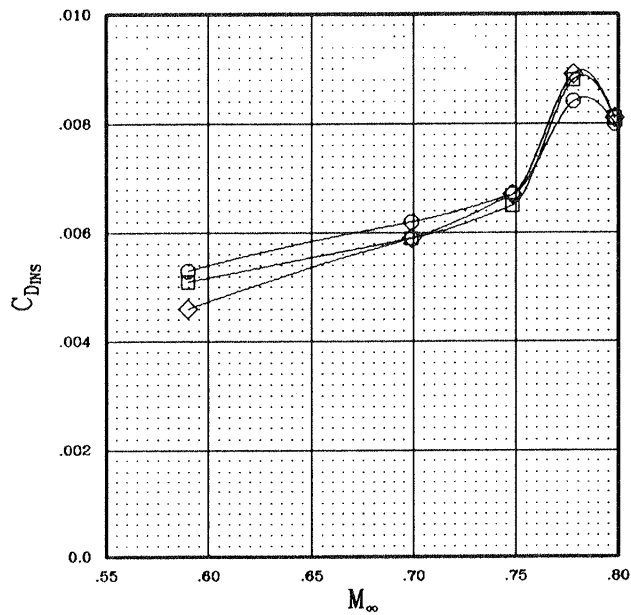
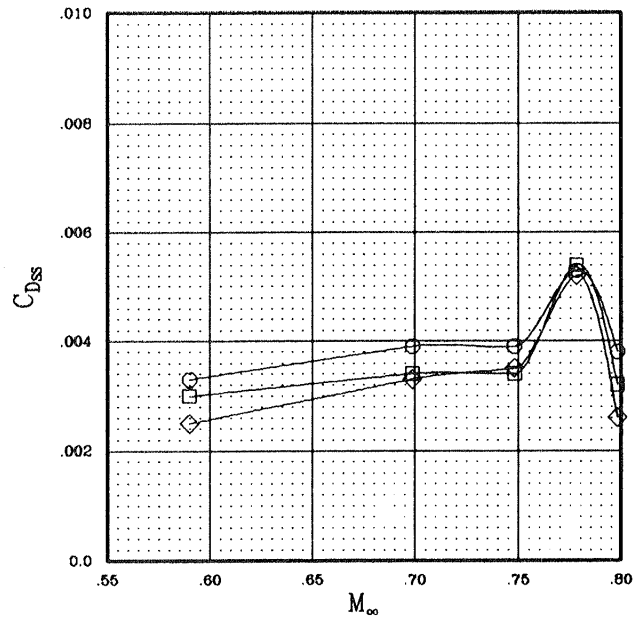
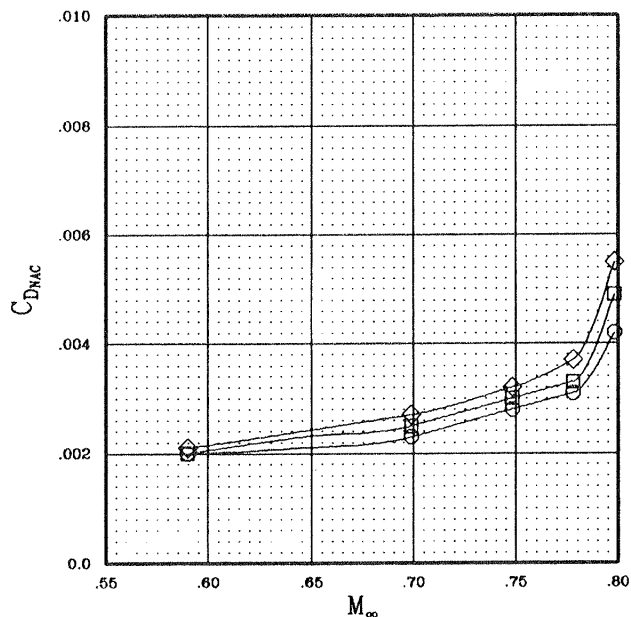
SYMBOL	CONFIGURATION	CTNET	CLEFF
○	W B OTW L H2 P2	.028	.450
□	W B OTW L H2 P2	.028	.500
◇	W B OTW L H2 P2	.028	.550



(a) Baseline configuration.

Figure 18.- Effect of cruise lift on the installation drags.

SYMBOL	CONFIGURATION	CTNET	CLEFF
○	W B OTW L H2 P2 E	.028	.450
□	W B OTW L H2 P2 E	.028	.500
◇	W B OTW L H2 P2 E	.028	.550



(b) Extended duct configuration.

Figure 18.- Concluded.

SYMBOL	CONFIGURATION	CTNET	CLEFF
○	W B OTW L H2 P2	.028	.500
□	W B OTW L H2 P2 E	.028	.500

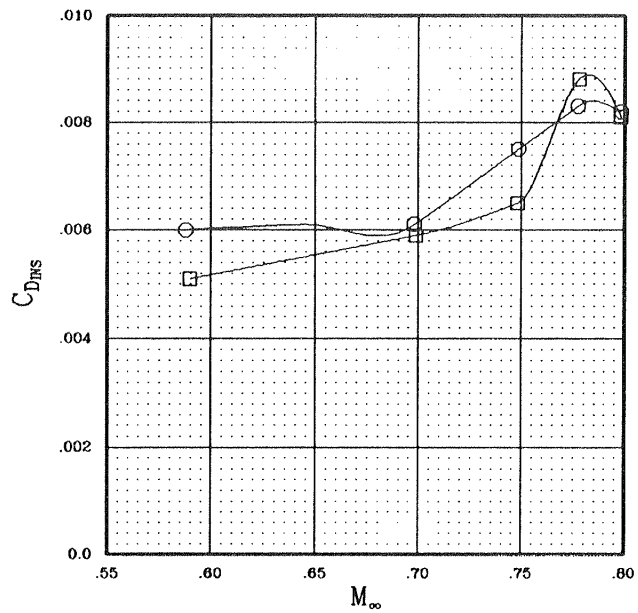
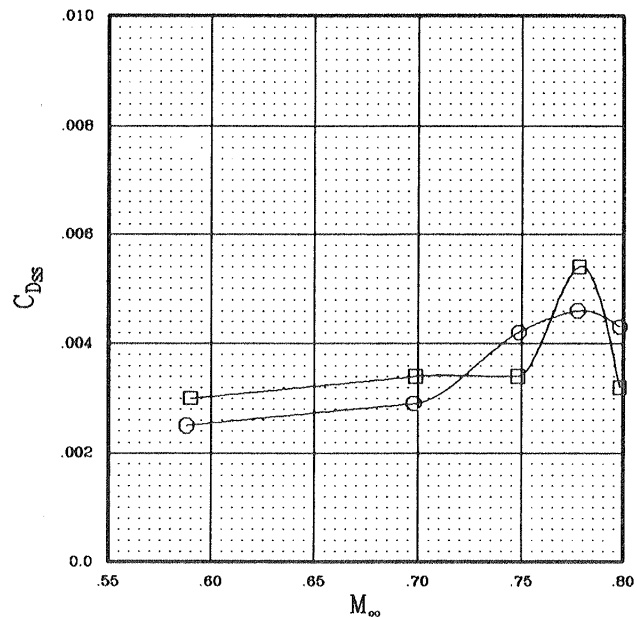
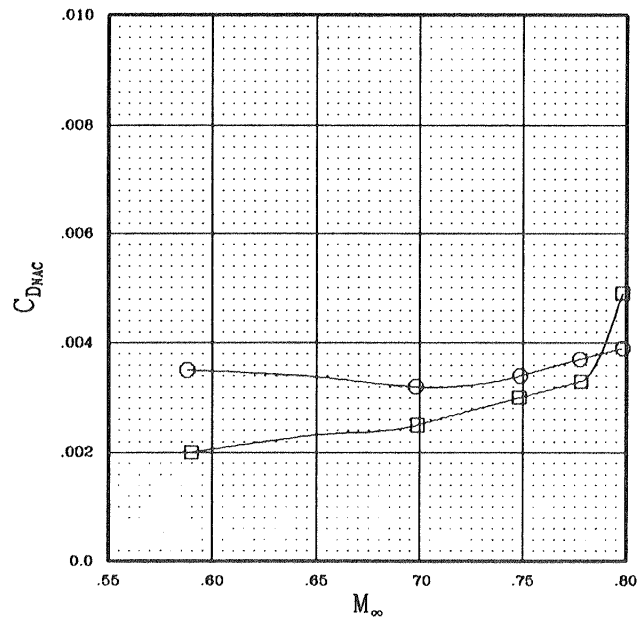


Figure 19.- Configuration effects on the installation drags.

SYMBOL	CONFIGURATION	CTNET	CLEFF
○	W B OTW L H2 P2	.028	.500
□	W B OTW L H2 P2 E	.028	.500
—◇—	W B UTW L H2 P2	.032	.500

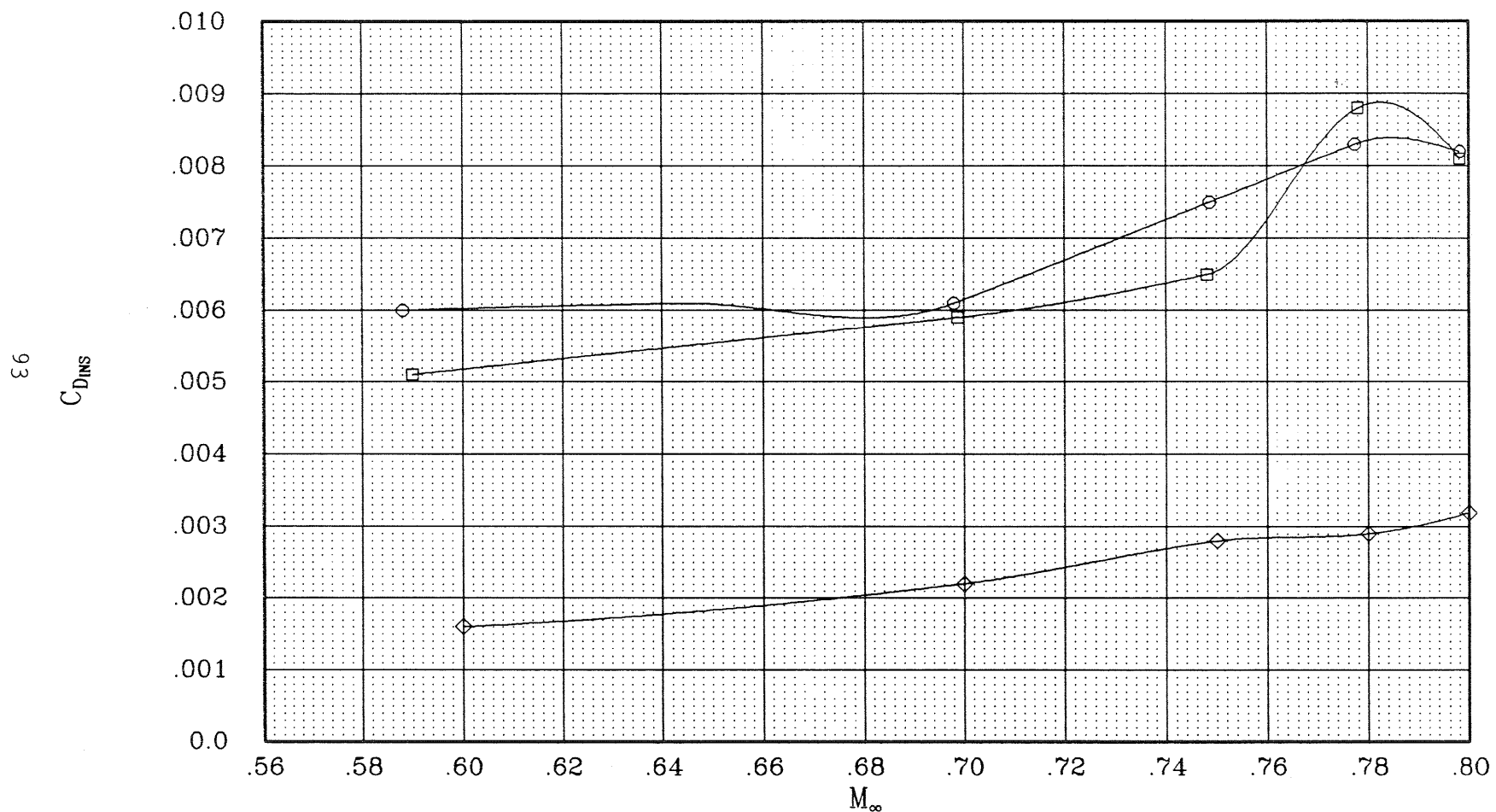


Figure 20.- Installation drag comparison between the UTW and OTW.

1. Report No. NASA TM 88206	2. Government Accession No.	3. Recipient's Catalog No.	
4. Title and Subtitle  TEST RESULTS AT TRANSONIC SPEEDS ON A CONTOURED OVER-THE-WING PROPFAN MODEL		5. Report Date July 1986	
		6. Performing Organization Code	
7. Author(s)  Alan D. Levin, Donald B. Smeltzer, and Ronald C. Smith		8. Performing Organization Report No. A-86082	
9. Performing Organization Name and Address  Ames Research Center Moffett Field, CA 94035		10. Work Unit No.	
		11. Contract or Grant No.	
12. Sponsoring Agency Name and Address  National Aeronautics and Space Administration Washington, DC 10546		13. Type of Report and Period Covered Technical Memorandum	
		14. Sponsoring Agency Code 535-03-11	
15. Supplementary Notes  Point of Contact: Alan D. Levin, Ames Research Center, MS 227-6, Moffett Field, CA 94035 (415) 694-5858 or FTS 464-5858			
16. Abstract  A semispan wing/body model with a powered highly loaded propeller has been tested to provide data on the propulsion installation drag of advanced propfan-powered aircraft. The model had a supercritical wing with a con- toured over-the-wing nacelle. It was tested in the Ames Research Center's (ARC) 14-Foot Transonic Wind Tunnel at a total pressure of 1 atm. The test was conducted at angles of attack from -0.5° to 4° at Mach numbers ranging from 0.6 to 0.8. The test objectives were to determine propeller perfor- mance, exhaust jet-effects, propeller slipstream interference drag, and total powerplant installation drag. Test results indicated a total power- plant installation drag of 82 counts (0.0082) at a Mach number of 0.8 and a lift coefficient of 0.5, which is approximately 29% of a typical airplane cruise drag.			
17. Key Words (Suggested by Author(s))  Turboprop Propulsion integration		18. Distribution Statement <u>Limited (for early</u> <u>domestic dissemination).</u> For use by U.S. Government and their contractors only. Date of general release <u>Jul.</u> <u>1988.</u> No foreign dissemination. Subject category - 05	
19. Security Classif. (of this report) Unclassified	20. Security Classif. (of this page) Unclassified	21. No. of Pages 96	22. Price* A03

**End of Document**